The Self-Assembly of Nanogold for Optical Metamaterials

by

Robert A. Nidetz

A dissertation submitted in partial fulfillment
of the requirements for the degree of
Doctor of Philosophy
(Materials Science and Engineering)
in The University of Michigan
2011

Doctoral Committee:

Associate Professor Jinsang Kim, Chair
Professor Peter Green
Associate Professor Lingjie Guo
Associate Professor Çagliyan Kurdak

© Robert A. Nidetz
2011

For Elizabeth, Elliott, and James

Acknowledgements

I must thank Professor Jinsang Kim before anyone else for being an amazing research advisor. There were moments that I felt like a failure during my time in graduate school, but Professor Kim was always there to reassure me that I could do this and keep me focused. I could never have reached this point without his constant support, encouragement, and wisdom. My heartfelt thanks go out to Professor Kim.

I am also thankful for my committee members. Professors L. Jay Guo, Peter Green, and Çagliyan Kurdak deserve special thanks for their work on my thesis committee. They provided great insight and discussion for my research.

Furthermore, I would like to thank the past and present members of the Kim Group for their comradery and support. In particular, I would like to thank Dr. Jae Cheol Cho for helping me get started with my PhD studies and David Bilby for his assistance on the PS-PVP project as an undergraduate. Onas and Laura, I miss having you guys in the lab to talk to about football and baseball. Jisama and Bonggi-ya, I will miss you both and being able to talk to you about babies and chemistry. Much thanks to Myungsu for being one of the warmest and friendliest people I have ever met.

The clean room staff has also been incredibly helpful to me during my PhD studies. I especially thank Tim Brock for being my go to guy for anything and everything ebeam. I would also like to thank Greg Allion for always going out of his way to help me out whenever I needed it. Also, thank you a million times to Dr. Pilar Herrara-Fierro and Dr. Nadine Wang for all of their help with my research and being awesome.

I do not think I could have made it through my PhD studies without my friends here at Michigan. To Obi, Chris, Adam Wood, and Mike Warren: thanks for always being there to help me waste time with pointless conjecture and to put a smile on my face. To Myungkoo, my MURI pal, I will miss you and your Halloween costume. To Lindsay and Rachel, I miss working out with you guys in the summer. To Gerri Bernard, my fellow Illini and the first friend I made here, I will miss our conjectures, our smoking breaks, our long toss, our wizard people, our beer drinking, and our kvetching. I also must give thanks to Mike Katz for teaching me TEM, spotting me at the gym, and being a great friend.

Lastly and most importantly, I must thank my wife, Elizabeth Covington, for her unwavering support as both a partner and a fellow graduate student. Sometimes I wonder if it was fate that allowed us to share a dry box in the clean room. You are my greatest collaborator. I love you.

Table of Contents

List of Figures

List of Tables

List of Abbreviations

Au NP	Gold Nanoparticle
Au NR	Gold Nanorod
D.I. H_2O	Deionized water
MeOH	Methanol
EtOH	Ethanol
IPA	Isopropanol
THF	Tetrahydrofruan
DMF	Dimethylformamide
MIBK	Methyl isobutyl ketone
CH_2Cl_2	Dichloromethane
$CHCl_3$	Chloroform
TFA	Trifluoroacetic acid
HCl	Hydrochloric acid
HF	Hydrofluoric acid
HNO_3	Nitric acid
NaOH	Sodium hydroxide
CTAB	Cetyltrimethylammonium bromide
$NaBH_4$	Sodium borohydride
$AgNO_3$	Silver nitrate

NaCl ..... Sodium chloride

APTMS 3-aminopropyltrimethoxysilane

APTES 3-aminopropyltriethoxysilane

APDMES 3-aminopropyldimethylethoxysilane

PMMA ..... Poly(methylmethacrylate)

PS ..... Poly(styrene)

PSS ..... Poly(styrene sulfonate)

PVP ..... Poly(vinyl-4-pyridine)

PTFE ..... Poly(tetrafluoroethylene)

EBL ..... Electron-beam lithography

SEM ..... Scanning electron microscopy

TEM ..... Transmission electron microscopy

AFM ..... Atomic force microscopy

Abstract

Optical metamaterials are an emerging field that enables manipulation of light like never before. Producing optical metamaterials requires sub-wavelength building blocks. The focus here was to develop methods to produce building blocks for metamaterials from nanogold.

Electron-beam lithography was used to define an aminosilane patterned chemical template in order to electrostatically self-assemble citrate-capped gold nanoparticles. Equilibrium self-assembly was achieved in 20 minutes by immersing chemical templates into gold nanoparticle solutions. The number of nanoparticles that self-assembled on an aminosilane dot was controlled by manipulating the diameters of the dots and nanoparticles. Adding salt to the nanoparticle solution enabled the nanoparticles to self-assemble in greater numbers on the same sized dot. However, the preparation of the nanoparticle solution containing salt was sensitive to spikes in the salt concentration which led to aggregation of the nanoparticles and non-specific deposition.

Gold nanorods were also electrostatically self-assembled. Polyelectrolyte-coated gold nanorods were patterned with limited success. A polyelectrolyte chemical template also patterned gold nanorods, but the gold nanorods preferred to pattern on the edges of the pattern. Ligand-exchanged gold nanorods displayed the best self-assembly, but suffered from slow kinetics.

Self-assembled gold nanoparticles were cross-linked with poly(diallyldimethylammonium chloride). The poly(diallyldimethylammonium chloride)

allowed additional nanoparticles to pattern on top of the already patterned nanoparticles. Cross-linked nanoparticles were lifted-off of the substrate by sonication in a sodium hydroxide solution. The presence of van der Waals forces and/or amine bonding prevent the nanogold from lifting-off without sonication.

A good-solvent evaporation process was used to self-assemble poly(styrene) coated gold nanoparticles into spherical microbead assemblies. The use of larger nanoparticles and larger poly(styrene) ligands resulted in larger and smaller assemblies, respectively. Stirring the solution resulted in a wider size distribution of microbead assemblies due to the stirring's shear forces.

Two undeveloped methods to self-assemble nanogold were investigated. One method used block-copolymer thin films as chemical templates to direct the electrostatic self-assembly of nanogold. Another method used gold nanorods that are passivated with different ligands on different faces. The stability of an alkanethiol ligand in different acids and bases was investigated to determine which materials could be used to produce Janus nanorods.

Chapter 1

Introduction and Background

1.1 Nanogold

As materials shrink from the bulk to the nanoscale, the materials begin to exhibit special properties not found in the bulk. One such property is metling point depression. For example, bulk gold has a melting point of 1337°K, but spherical gold nanoparticles (Au NPs) melt at much lower temperatures as the size of the nanoparticle decreases.[1] Also, Au NP solutions generally display a brilliant red color, unlike the bulk material which is a shiny yellow. The red color is a result of the Au NP's surface plasmon.

The following sub-chapters describe the surface plamons of gold colloids and how the sizes, shapes, and assemblies of gold colloids effect the surface plasmon resonance. The synthesis of Au NPs and gold nanorods (Au NRs) will also be discussed, as well as techniques to assemble Au NPs and Au NRs. Lastly, negative index materials, optical metamaterials, and perfect absorbers will be discussed, since assemblies of nanogold could be used as the building blocks for these materials.

1.1.1 Surface Plamons of Nanogold

The surface plasmon is a coherent electron oscillation that is excited by an electric field (light) at an incident wavelength where resonance occurs. This results in strong light

scattering, the appearance of intense surface plasmon bands, and an enhancement of the local electromagnetic fields.[2]

For Au NPs less than a critical size (~30 nm) the surface plasmon absorbance is between 520 and 530 nm, depending on the refractive index of the suspending medium.[3] However, once particles grow larger than 30 nm, the surface plasmon absorbance red-shifts as a simple dipole approximation is no longer appropriate to model the resonance and Mie theory becomes applicable.[4] The surface plasmon absorbance of various sized Au NPs is shown in Figure 1.1a, which shows the red-shifting effect for larger sized Au NPs.

Furthermore, two-dimensional nanometals can display more than one surface plasmon. In the case of gold nanorods (Au NRs), the two resonances are from the longitudinal and transverse axis of the rods. The longitudinal resonance is dependent on the aspect ratio of the Au NR and is generally red-shifted from the transverse resonance.[5] As the aspect ratio of the Au NR increases, the longitudinal resonance can red-shift out of the visible regime and into the Near-IR regime. Figure 1.1b demonstrates this effect for Au NRs with increasing aspect ratios.

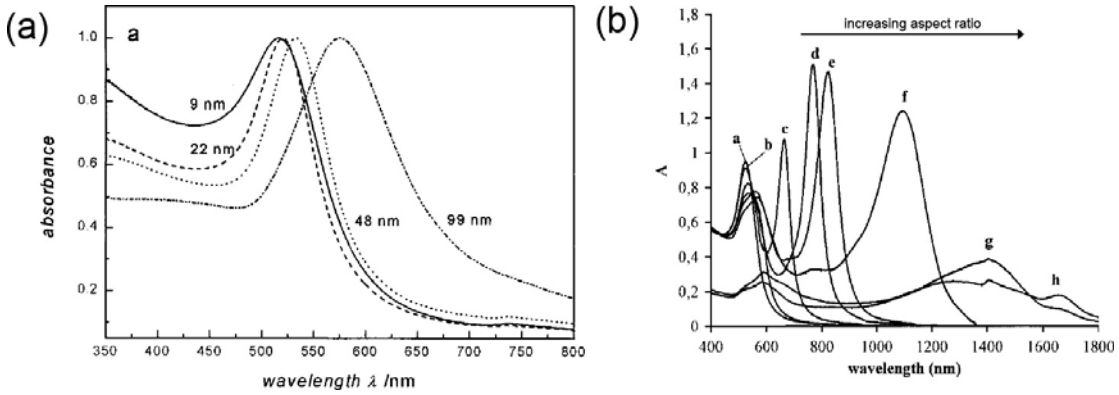

Figure 1.1 Effects of the geometry of nanogold on the surface plasmon resonance. (a) The surface plasmon wavelength of Au NPs red-shifts as the size of the Au NPs increases. (b) The longitudinal surface plasmon wavelength red-shifts as the aspect ratio of the Au NR increases. Images reproduced from (a) Link and (b) Jana.[4, 5]

1.1.2 Synthesis of Gold Nanoparticles

Au NPs are generally synthesized in solution by the reduction of a gold salt ($HAuCl_4$) in the presence of a ligand. The ligand usually serves to rapidly reduce the gold from Au^{3+} to Au^{1+}. The reduction of Au^{1+} to Au^0 is accomplished by a reducing agent. Once Au^0 is formed, the atoms begin to agglomerate and Au NPs are formed.

All glassware used in the synthesis of Au NPs must be free from metal contamination. Thus, glassware is commonly washed with Aqua Regia (3:1 v/v of $HCl:HNO_3$) and rinsed with copious amounts of D.I. water prior to being used for Au NP synthesis.

One of the earliest methods to synthesize Au NPs in solution is the citrate-reduction method.[6-8] In this synthesis, a solution of gold salt is boiled in water and a small amount of aqueous sodium citrate is added to the boiling solution. The yellowish gold salt solution first turns blue, then purplish, and eventually red as the citrate reduces the gold salt to form Au NPs. In addition to acting as the reducing agent, the citrate also coats the Au NPs and serves as a passivating layer. The size of the Au NPs is controlled by the amount of sodium citrate that is added to the gold salt solution. Larger particles are generated by adding less sodium citrate. Spherical, relatively monodisperse particles can be generated with diameters between 10 and 20 nm. As larger particles are produced, they become more polydisperse and their shape becomes more ellipsoidal than spherical.

Recently it was reported that citrate-capped Au NPs could serve as seeds to grow larger, spherical, citrate-capped Au NPs.[9] Citrate-capped Au NPs were prepared as previously mentioned, and then added to a solution containing $HAuCl_4$ under stirring. Sodium citrate and hydroquinone were then added to the solution, which generated

larger, spherical, citrate-capped Au NPs. In this technique, the hydroquinone reduces Au^{1+} to Au^0, but only in the presence of the Au NP because hydroquinone does not have a large enough reduction potential to spontaneously reduce the Au^{1+}.

Another recipe for generating Au NPs is commonly referred to the Brust method.[10] In this synthesis, $HAuCl_4$ is dissolved in water and tetraoctylammonium bromide (TOAB) is dissolved in toluene. The two solutions are mixed together under stirring until the $HAuCl_4$ is transferred to the toluene phase. After discarding the aqueous phase, an aqueous solution of sodium borohydride ($NaBH_4$) is added to the toluene solution, under stirring. The $NaBH_4$ reduces the $HAuCl_4$ to form TOAB coated Au NPs in toluene. Thus, the TOAB serves as both the phase-transfer agent for the gold salt and the ligand for the Au NP in this recipe. Au NPs produced via this method are generally 5.5 nm in diameter. The Au NPs are not very soluble in the toluene, and generally precipitate within a week. It is possible to exchange the TOAB for a thiol-functional ligand that will more permanently stabilize the Au NPs.

The addition of $NaBH_4$ to an aqueous solution of $HAuCl_4$ and cetyltrimethylammonium bromide (CTAB) can also generate CTAB capped Au NPs. These particles are more stable than the TOAB capped Au NPs, but the CTAB is not very soluble below 27°C, and may precipitate as crystals from the solution. These Au NPs are generally 4 nm in diameter.[11] Similarly, 3.5 nm diameter citrate-capped Au NPs can be generated by adding $NaBH_4$ to an aqueous solution of $HAuCl_4$ and trisodium citrate.[5, 12]

Small citrate-capped Au NPs generated from the addition of $NaBH_4$ to a solution of $HAuCl_4$ and citrate can also serve as seeds for the formation of larger Au NPs.[13] The small, citrate-capped Au NPs are added to a vial of growth solution containing $HAuCl_4$,

CTAB, and ascorbic acid. The ascorbic acid reduces the Au^{3+} to Au^{1+}, which facilitates the growth of the Au NPs. The CTAB replaces the citrate as the ligand for the Au NPs during this growth procedure. By adding the newly grown, larger, CTAB capped Au NPs to another vial of growth solution, it is possible to generate even larger Au NPs. Au NPs ranging from 5.5 to 37 nm were generated via this technique. However, as even larger Au NPs are generated, Au NRs are generated as unwanted by-product.

Superhydride ($LiEt_3BH$) can also be used as a reducing agent for the synthesis of Au NPs from $HAuCl_4$ in THF with a thiol-functional ligand.[14] This recipe produces relatively monodisperse Au NPs. However, as the length of the ligand increases, both the size and size dispersity of the Au NPs increase as well.[15] This is due to the steric hindrance of the larger ligands that causes less-effective capping of the Au NP core and may influence the growth rate of the Au NP core.

Au NPs can also be synthesized by adding a solution of $HAuCl_4$ and oleylamine to boiling a solution of oleylamine in toluene.[16] The oleylamine is necessary to solubilize the $HAuCl_4$, since the salt is not soluble in toluene. In this recipe, the oleylamine acts as both the ligand and the reducing agent. Spherical Au NPs with diameters between 6 and 21 nm can be produced via this recipe. The oleylamine can also be replaced via a thiol-functional ligand.

1.1.3 Synthesis of Gold Nanorods

Au NRs were first synthesized in water using an electrolysis technique.[17] In this synthesis, a gold anode and a platinum cathode were immersed into an aqueous solution containing acetone, CTAB, and TOAB. A current of 3 mA was applied for 30 min. under

ultrasonication at 38°C to produce Au NRs. However, drawbacks to this technique are that only Au NRs with longitudinal plasmon bands less than 850 nm could be generated and a large fraction of Au NPs are generated as a by-product.[11]

Au NRs were later synthesized by Jana, et al. using wet chemistry.[5] This procedure is commonly referred to as the seed-growth technique. First, small Au NPs were synthesized via the reduction of $HAuCl_4$ in water with sodium citrate by $NaBH_4$. This produces 4 nm diameter, citrate-capped Au NPs that serve as the seeds for the Au NRs. Next, a volume of this solution was added to a growth solution containing $HAuCl_4$, CTAB, cylclohexane, acetone, $AgNO_3$, and ascorbic acid. CTAB capped Au NRs would then form in this solution. This synthesis was capable of producing Au NRs with aspect ratios from 1 to 7, depending on the gold seed to gold salt ratio. However, there were still a significant amount of Au NPs that were formed as a by-product.

Jana et al. also developed a wet-chemistry technique to prepare high aspect ratio Au NRs using an expanded seed-growth technique.[12] 3.5 nm diameter citrate-capped Au NPs were used as a seed. The seeds were then added to a growth solution containing $HAuCl_4$, CTAB, and ascorbic acid. To produce larger aspect ratio Au NRs, three test tubes (labeled A, B, and C) containing growth solution were prepared. Sometime after the seed solution was added to test tube A, a small volume from test tube A was added to test tube B. Similarly, a small volume was added to test tube C. Large aspect ratio Au NRs would be formed in test tube C. The aspect ratio of the final Au NRs in test tube C was controlled by the altering the time in which volumes from test tubes A and B were added to test tubes B and C, respectively. While a large amount of Au NPs were generated as a

by-product, they were easily separated from the long Au NRs via centrifugation and discarding the supernatant.

However, the most commonly used Au NR recipe was developed by Nikoobakht et al.[11] In this recipe, an aqueous seed solution of CTAB-capped Au NPs is formed by the reduction of $HAuCl_4$ in solution with CTAB by $NaBH_4$. A small volume of seed solution is then added to an aqueous growth solution which contains CTAB, $HAuCl_4$, $AgNO_3$, and ascorbic acid. The solution is left overnight to allow the Au NRs to form. By varying the amount of $AgNO_3$ present in the growth solution, it was possible to control the aspect ratio of the Au NRs. In order to grow Au NRs with aspect ratios greater than 4.5, benzyldimethylhexadecylammoniumchloride was also used in the growth solution. The advantage of this synthetic route is that pure Au NR solutions are synthesized.

The recipes developed by Jana et al. and Nikoobakht et al. are very similar, but are also very different. All of the recipes use Au NPs as seeds, have growth solutions containing $HAuCl_4$, CTAB, and ascorbic acid, and produce CTAB coated Au NRs. These ingredients are critical to the synthesis of Au NRs.

Ascorbic acid is used in the synthesis of Au NRs because of its ability as a weak reducing agent. The ascorbic acid reduces the gold ions in the growth solution from Au^{3+} to Au^{1+}, which facilitates the growth of the Au NP seed into Au NRs. It should be noted that the ascorbic acid is not capable of reducing Ag^+ to Ag^0 when $AgNO_3$ is used in the growth solution.

Initial investigation into the role of CTAB and $AgNO_3$ in the synthesis of Au NRs theorized that the CTAB bound to the {110} faces of the gold and thus directed growth in

the {100} direction, while the Ag somehow formed a Ag-Br complex that facilitated the binding of the CTAB.[11, 18] However, the roles of CTAB and $AgNO_3$ are not that simple.

It was found that the silver deposits on the surface of the Au NPs via an underpotential deposition (UPD).[19] Silver UPD is the reduction of Ag^+ to Ag^0 at a metal substrate with a surface potential less than the standard reduction potential of Ag^+. Furthermore, it was suggested that the Ag^+ deposits on the {110} surfaces faster than either the {100} or {111} faces. This rapid silver deposition followed by strong CTAB binding, via AgBr, inhibits gold growth on the sides of the Au NRs and leads to preferential growth of gold at the ends. Ultimately, as the number of Au^+ ion collisions decreases, the rate at which the Ag+ deposits on the {100} end of the Au NR dominates, and the rod growth ceases. The mechanism for Au NR growth in the presence of $AgNO_3$ is illustrated in Figure 1.2. The UDP explains why Au NRs grown in the presence of $AgNO_3$ are shorter than those grown without $AgNO_3$.[5, 18]

It was recently shown that Au NRs could be formed in the presence of $AgNO_3$ with concentrations of CTAB that were below the critical micelle concentration via the addition of NaBr.[20] Also, it has been shown that the concentration of iodide impurities in CTAB can effect if Au NRs, Au NPs, or gold triangular prisms result from the seed growth synthesis.[21-23] Thus, the presence of bromide and iodide ions appears to be critical to forming Au NRs.

One of the major differences between the Jana and Nikoobakht recipes is that the Jana recipes use aged, citrate-capped Au NP seeds (> 2 hrs. old) and the Nikoobkaht recipe uses recently prepared CTAB capped, Au NP seeds (5 min. old). The seeds and growth mechanism of the Jana and Nikoobakht Au NRs was previously investigated

using high-resolution transmission electron microscopy (HRTEM).[19] It was found that the Jana seeds were about 3 nm in diameter, while the Nikoobakht seeds were about 1.5 nm in diameter. Furthermore, the Jana seeds are twinned crystals that are decahedron in shape with five twin boundaries that are all {111} planes. In contrast, the Nikoobakht seeds appear to be single crystalline. HRTEM of the two seeds are shown in Figure 1.3.

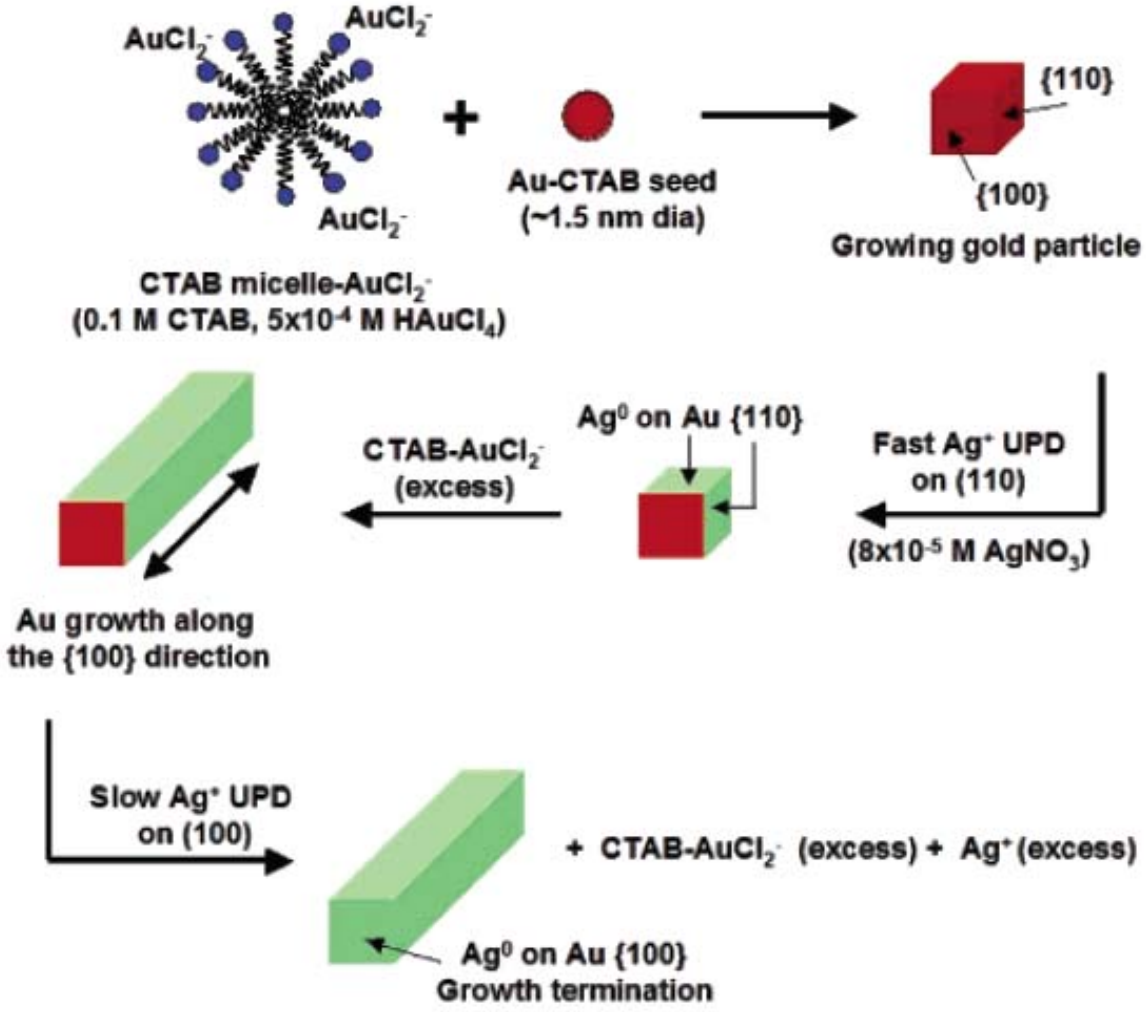

Figure 1.2 Cartoon of the mechanism of nanorod growth from CTAB-protected gold seed particles in the presence of Ag^+. Image reproduced from Orendorff.[24]

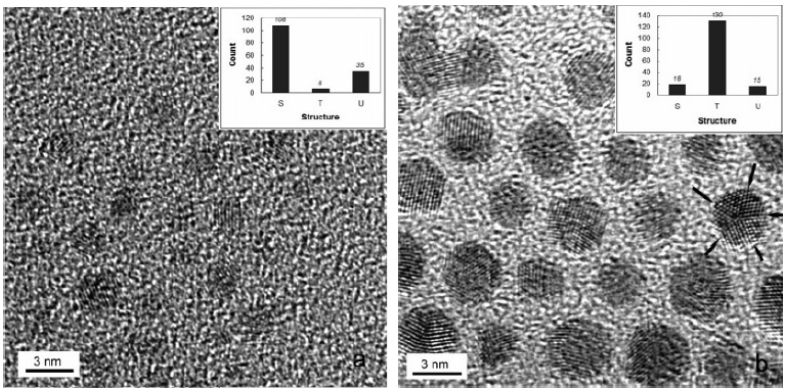

Figure 1.3 HRTEM image of (a) Nikoobakht seeds and (b) Jana seeds. One of the seeds shows a very clear penta-fold twinning. The twinning planes are indicated by the arrows in (b). The histograms are counts of the single crystalline, S, twinned, T, and unidentified, U, nanoparticles observed in each sample. There are more unidentified particle for the Nikoobakht seeds because of their smaller size and therefore worse contrast. Image recreated from Liu.[19]

Until recently, it was believed that Au NRs were octagonal prisms with four {100} and four {110} side facets, and capping facets that were either {100}, {110}, or {111}, as illustrated in Figure 1.4a.[19, 25-27] However, this model was flawed for two major reasons. The first reason was that the Au NRs only grow rapidly along one of the <100> directions without any dendritic growth along the side facets that belong to the <100> family. The second reason was that despite the different surface energies of the {100} and {110} facets, the Au NR was still symmetric. From the UDP theory, it is believed that the Ag ions preferentially bind to the {110} facets because of more abundant vacancies and higher surface energy on this facet. Thus, the Au NR should be asymmetric along its longitudinal axis due to the different facets. However, the Au NR displays a regular, octagonal cross-section.

Recent work has shown that the side facets of the Au NRs are all symmetry equivalent and are of higher index than the {100}, {110}, or {111} varieties.[28, 29] The result of these findings helps account for the observed symmetric growth of the Au NRs.

The crystallography was determined using a series of high-angle annular dark-field TEM images that were compiled to determine the three-dimensional structure of the Au NRs.[29] The three-dimension structure is illustrated in Figure 1.4b. Due to the higher index of the side facets, which were found to be {0 5 12}, there are more vacancies and greater surface energy on these facets.[29] These two factors would promote the adhesion of both Ag ions for the UDP mechanism and surfactant to reduce the free energy of the facet. Thus, the presence of Ag ions and surfactant on the side factets facilitate the anisotropic growth mechanism.

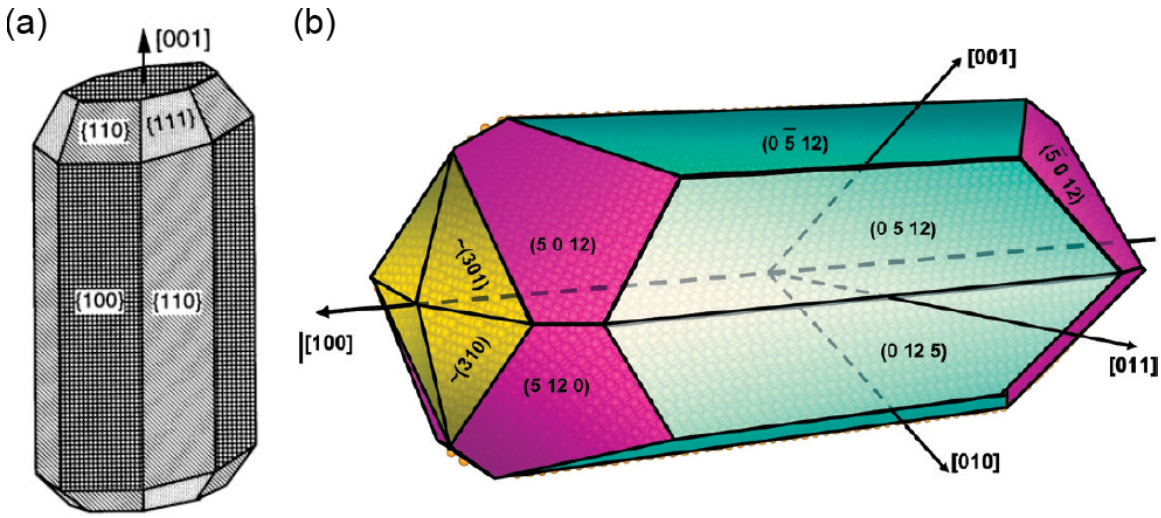

Figure 1.4 Illustrations of the crystallography of Au NRs as (a) previously proposed with asymmetric side facets and (b) currently proposed with symmetrical side facets. Images recreated from (a) Wang[26] and (b) Katz-Boon[29].

The pyramidal caps of the Au NRs were found to have different symmetry than the side facets, but the facets that connected the pyramidal caps to the sides were found to be symmetrically equivalent to the sides.[29] The different symmetry of the end caps may explain the promotion of growth along the rod axis and the greater chemical reactivity of the nanorod tips.

Furthermore, the Au NRs were found not to have sharp facets, but rounded facets.[28, 29] The normal to the {0 5 12} facet bisects the normals to the {001} and {011} directions. Thus, the octagonal, high-index, symmetrically equaivalent side facets may be a result of terraced stacking of {001} atomic planes on a cube having {001} faces.[29]

1.1.4 Synthesis of Gold Nanoclusters

It is briefly worth mentioning that ultra-small (diameter < 2 nm) Au NPs are often referred to as gold nanoclusters. A recent review elucidated the differences between Au NPs and gold nanoclusters[30] Due to these striking differences, when referring to Au NPs, only Au NPs with diameters greater than 2 nm are of consideration.

Gold nanoclusters demonstrate quantum confinement effects. This quantum confinement results in a discrete electronic band structure, HOMO-LUMO electronic transition, enhanced photoluminescence, and the inability to support surface plasmons. Figure 1.5 compares the UV-Vis absorption spectra of Au NPs and gold nanoclusters.

Also, there exist synthetic routes that are capable of producing monodisperse gold nanoclusters. The general synthesis involves the reduction of $HAuCl_4$ at low temperature with a thiol-functional molecule to generate an $[Au^{1+}]$-SR intermediate that is reduced at low temperature with $NaBH_4$ to form a monodisperse gold nanocluster.[31] The synthesis is very similar to one used to generate Au NPs.[32]

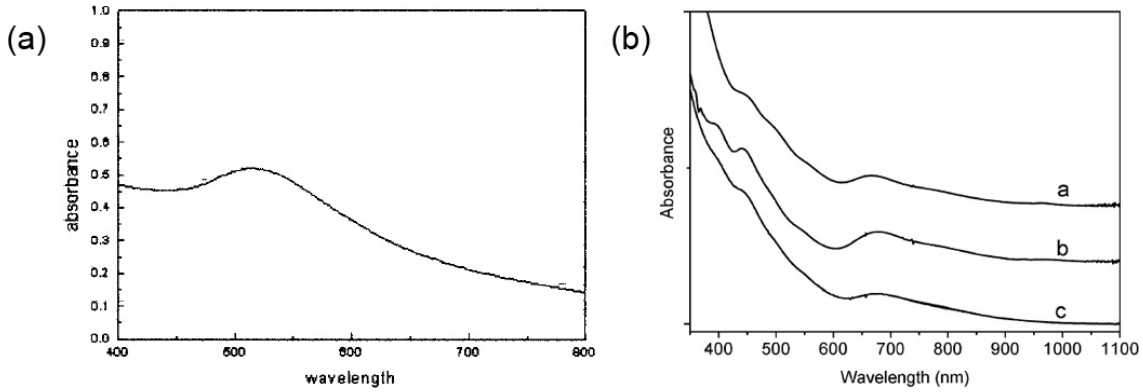

Figure 1.5 UV-Vis absorbance spectra for (a) thiol-capped Au NPs and (b) various thiol-capped, 25 atom gold nanoclusters. The Au NPs show one peak at 525 nm which corresponds to the surface plasmon absorption. The gold nanoclusters show peaks at 400 nm, 440 nm, and 690 nm which arise from an interband transition (sp ← d), a mixed intraband (sp ← sp) and interband (sp ← d) transition, and a LUMO ← HOMO transition, which is essentially an intraband transition (sp ← sp), respectively. Images recreated from Yee[14] and Wu[33].

1.2 Assemblies of Nanoparticles

By assembling nanogold, it is also possible to shift the plasmonic resonance and create new resonances. Aggregations of Au NPs have been shown to exhibit two plasmonic resonances, one due to the aggregate and the other due to the individual particles.[34-36] In the case of Au NRs, assemblies of the NRs shift the longitudinal plasmon absorbance. End-to-end assemblies of Au NRs cause the longitudinal plasmon absorbance to red-shift, while side-by-side assemblies cause the longitudinal plasmon absorbance to blue-shift.[37] Thus, by altering the geometry of the nanometals and their assemblies, it is possible to tune the resonant frequencies.

1.2.1 Self-Assembly of Nanogold in Solution

Nanogold can be assembled in solution using a molecule to cross-link the nanogold. This cross-linking can be accomplished via covalent bonding, electrostatics, or

biological systems. It is also possible to assemble nanogold by using solvent selectivity to induce aggregation of the nanogold.

Covalent cross-linking of Au NPs. has previously been demonstrated to form a spherical assembly of Au NPs.[34-36] This was accomplished by introducing a tridentate thioether ligand or a dithiol ligand. In both cases, the size of the spherical assembly of Au NPs was inversely proportional to the amount of ligand that was added to the Au NP solution. Figure 1.6 shows the evolution of separate surface plasmon absorptions as the size of the spherical assemblies of Au NPs increases. One absorption is from the individual Au NPs, and one absorption is from the whole spherical assembly. As the spherical assembly grows larger, its absorption red-shifts similar to how the absorption of individual Au NPs red-shifts as the Au NPs get larger. For smaller assemblies of the Au NPs, the surface plasmon absorption is similar to that of the individual Au NPs, so the two peaks convalesce to form one, wide surface plasmon absorption.

Nanogold may also be self-assembled in solution by using electrostatic forces. For example, positively charged, cetyl trimethylammonium bromide (CTAB) capped Au NRs can be aggregated into clusters by adding adipic acid to the Au NR solution.[38] The adipic acid acts as a connecting bridge between the Au NRs and causes them to form side-by-side assemblies. It was possible to reversibly assemble or disassemble the Au NRs by varying the pH of the solution to deprotonate or protonate the adipic acid.

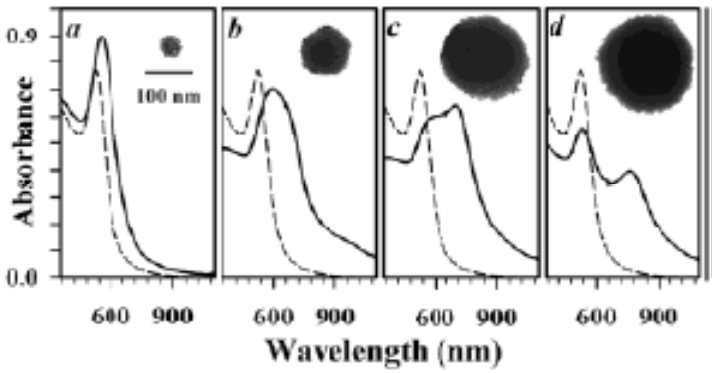

Figure 1.6 Extinction absorption for individual Au NPs (dashed lines) and assemblies of Au NPs (solid lines) after the addition of (a) 200, (b) 20, (c) 0.8, and (d) 0.08 μM of tidentate thioether. Transmission electron microscopy images of representative assemblies are included as inserts. Image reproduced from Maye.[36]

Biological ligands have also been used to assemble nanogold in solution. The biotin-streptavidin system was used to assemble Au NRs in both and end-to-end fashion[39] and a side-by-side fashion[40]. DNA has also been used to assemble Au NPs in solution. By using DNA ligands, Au NPs have been assembled into quadruple-helicies[41] and pseudocrystals[42, 43]. In the case of the pseudocrysals, the interparticle spacing and crystal structure could be controlled by altering the length of the DNA stands as well as by using either direct hybridization or a complementary DNA strand.

Solvent selectivity is another technique used to assemble nanogold. Based on the solvent, the nanoparticles will organize to minimize the free-entropy of the system. If there is a favorable interaction between the nanoparticle's ligand and the solvent, then the particles will be stable in solution. However, if the interaction is unfavorable, the particles will aggregate to minimize their interaction with the solvent and to maximize their interaction with each other. Au NRs capped with poly(styrene) on their ends and CTAB along their facets were assembled into various structures by varying the solvent

selectivity for the poly(styrene) and CTAB, as seen in Figure 1.7.[44-46] By assembling the Au NRs, the longitudinal plasmon resonance shifted, based on the type of assembly.

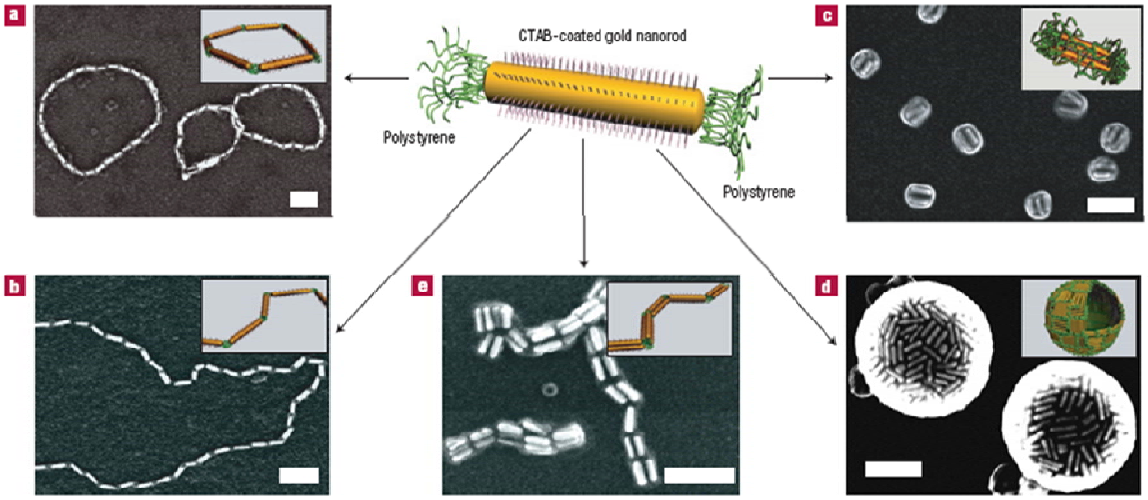

Figure 1.7 Self-assembly of an amphiphilic gold nanorod carrying a double layer of CTAB along the longitudinal side and poly(styrene) molecules grafted to both ends. Scanning electron microscopy images of the self assembled nanorod structures: (a) rings, (b) chains self-assembled in the dimethyl formamide/water mixture at water contents of 6 and 20 wt%, respectively, (c) side-to-side aggregated bundles of nanorods and (d) nanospheres self-organized in the tetrahydrofuran/water mixture at water contents of 6 and 20 wt%, respectively, and (e) bundled nanorod chains obtained in the ternary dimethyl formamide/tetrahydrofuran/water mixture at a weight ratio of liquids 42.5:42.5:15. The scale bars are 100 nm. The inserts show corresponding schematic diagrams of the nanorod assemblies. Image recreated from Nie.[45]

1.2.2 Self-assembly of Nanogold on Surfaces

There exist many methods to assemble nanogold on surfaces.[47-52] Most of these methods involve functionalized surfaces. In a typical assembly, the functional surface is immersed in a solution of nanogold, and the nanogold is allowed to self-assemble onto the functional surface before the surface is removed from the solution. These functional surfaces can covalently bind nanogold to the surface.[53-55] Au NPs have been previously been self-assembled onto a surface by using free thiols to covalently bind the Au NPs to the surface.[53, 54]

Electrostatic forces are commonly used to self-assemble Au NPs on surfaces.[53, 56-63] Generally, Au NPs are functionalized with a charged ligand and self-assembled on an oppositely charged, patterned surface. Functional, charged surfaces can be fabricated using self-assembled monolayers[53, 62], electron-beam lithography[56, 58, 60, 63], nanoimprint lithography[59], microcontact printing[64], or AFM-tip lithography[65-68]. For the electrostatic assembly of Au NPs, an aminosilane such as 3-aminopropyltrimethoxysilane (APTMS) is used to functionalize a silicon wafer surface with a positive charge. Figure 1.8 shows examples of Au NPs that were electrostatically self-assemble using aminosilanes. Polyelectrolytes, which are charged polymers, are also commonly used to functionalize a surface with a charge. An intermediate molecule can also be used to enable the self-assembly of multi-layers of Au NPs.[55]

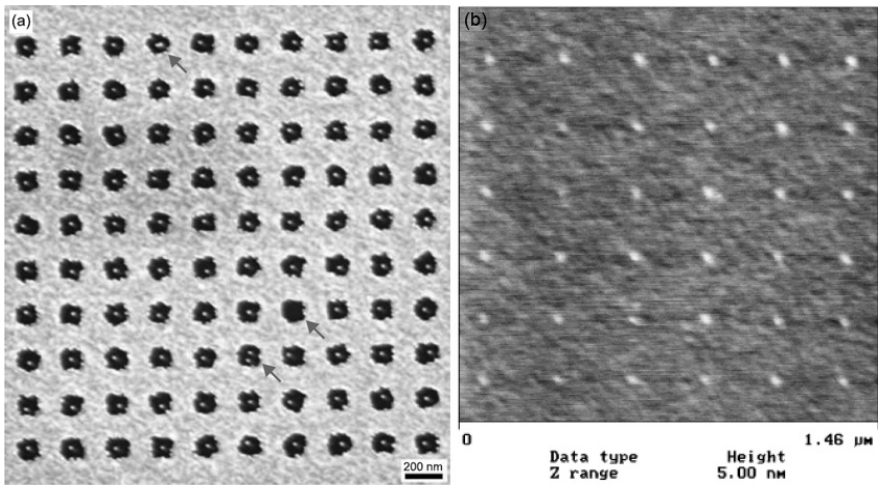

Figure 1.8 Examples of electrostatic assembly of Au NPs using an aminosilane patterned surface. (a) SEM image of Au NPs self-assembled into wells patterned with aminosilane and a hydrophobic Au film surface. (b) AFM image of Au NPs self-assembled onto aminosilane dots patterned using AFM-tip oxidation. Images recreated from Huang[56] and Li[65].

The meniscus method can also be used to assemble nanoparticles on surfaces.[69-76] This technique uses a moving meniscus to direct nanoparticles into a two-dimensional

array of cylindrical holes or trenches that have been lithographically patterned. As the meniscus moves along the surface, the capillary force drives the nanoparticle into the recessed regions that were lithographically generated. A schematic illustrating the forces involved in the meniscus method is shown in Figure 1.9a. Depending on the geometry of the recessed regions, it is possible to pattern nanoparticles in different geometries, as observed in Figures 1.9b-f.

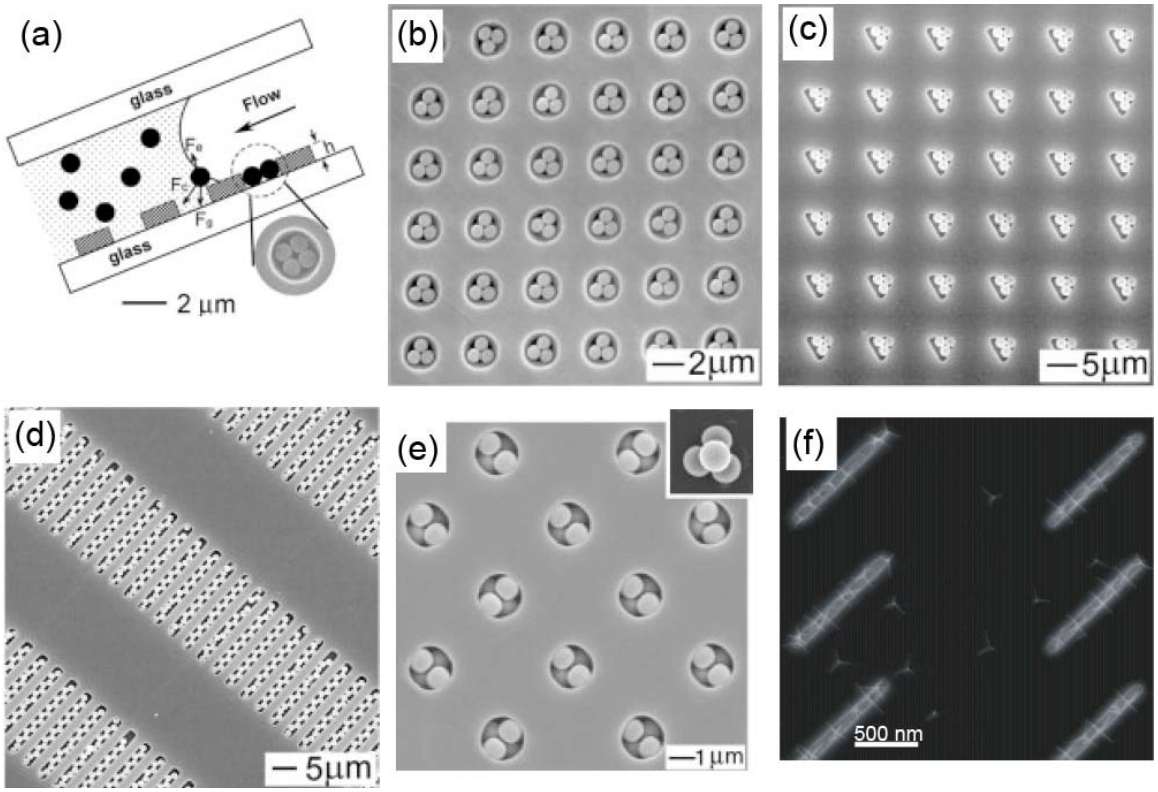

Figure 1.9 (a) Illustration of the gravitational (F_g), electrostatic (F_e), and capillary (F_c) forces involved in the patterning of nanoparticles using the meniscus method. Examples of latex spheres patterned in (b) cylindrical holes, (c) triangular holes, and (d) rectangular trenches via the meniscus method. (e) Tetramers of latex spheres are patterned in a deep cylindrical hole. The inset shows the tetramer after removing the resist. (f) Nanotetrapods are patterned in rectangular trenches. Images recreated from (a) – (e) Xia[76] and (f) Cui[69].

1.2.3 Self-Assembly of Nanogold in Polymers

Block copolymers have also been used to pattern nanoparticles. There are several examples of sequestering nanoparticles within one block of the copolymer.[77-79] To sequester the nanoparticles within one block, it is necessary to use a ligand that preferentially mixes with one block. It has also been shown possible to synthesize nanoparticles within one block of the copolymer after it has self-assembled.[80, 81]

1.3 Negative Index Materials

The refractive index or index of refraction of a material is the measure of the speed of light in that substance. It is expressed as a ratio of the speed of light in a vacuum relative to that in the considered medium. Thus, light travels faster through a material with a lower index of refraction. The refractive index of a material, n, is determined by its relative electric permittivity, ε_r, and its magnetic permeability, μ_r, at a frequency, ω, by the following equation:

$$n(\omega) = \pm\sqrt{\varepsilon_r(\omega)\mu_r(\omega)}. \quad (1)$$

Most materials do not have a strong magnetic response, so in most cases $\mu_r(\omega) = 1$. Thus, the refractive index is often directly related to the permittivity, which can vary depending on the frequency of the incident radiation. For example, in the case of a glass prism, incident white light is transmitted as a rainbow because the refractive index/permittivity is greater for higher frequencies of light. This results in different frequencies of light refracting at different angles. Thus, the rainbow appears.

Negative index materials (NIMs) are materials that exhibit a negative index of refraction for certain frequencies of light. In conventional materials, both the permittivity

and permeability are positive values, and thus, the refractive index is a positive value. However, there exists the academic question which supposes that there was such a material that had negative values of both the permittivity and the permeability, and thus a negative index of refraction.

One of the first papers addressing the issue of NIMs was published by Veselago over 40 years ago.[82] In this paper, Veselago investigated what would happen to Maxwell's equations in the case of NIM. The result was that for negative values of ε and μ, the electric field, the magnetic field, and the wave vector form a left-handed set instead of a right-handed set. Thus, NIMs are often referred to as left-handed materials. One consequence of this left-handed set was that the phase velocity and the group velocity are anti-parallel. Figure 1.10 compares the propagation in both a right-handed and a left-handed material. While the Poynting vector, S, continues to travel away from the source in the NIM, the phase, k, appears to travel towards the source instead of away from the source in a NIM. Relating back to the definition of the refractive index, it would only make sense that a NIM would cause the radiation to have a "negative" speed through the material.

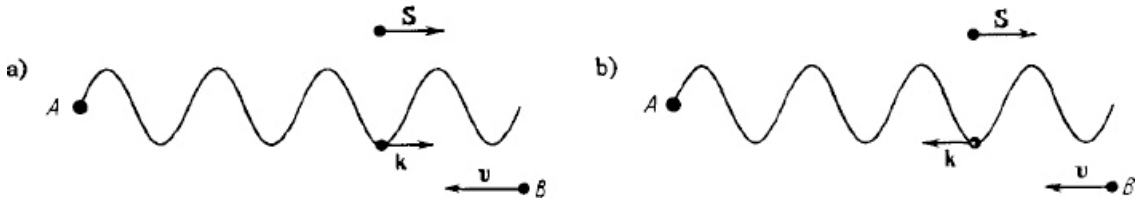

Figure 1.10 Propagation of an electromagnetic wave through a right-handed material (a) and a left-handed material (b). The letter A represents the source and the letter B represents the observer. Recreated from Veselago.[82]

Another consequence of a NIM is that light refracts to the left when it passes through the boundary from a positive index material into a NIM. This is easily explained by Snell's law,

$$\frac{\sin\theta_1}{\sin\theta_2} = \frac{n_2}{n_1}, \tag{2}$$

which states that the ratio of the sines of the angles of incidence and refraction is equivalent to the opposite ratio of the indicies of refraction. Thus, for a NIM, the angle of refraction must be negative. One outcome of this negative refraction is that a NIM plate with a thickness, *d*, will focus the radiation from a point source located a distance *l* < *d* from the plate, as seen in Figure 1.11. In essence, the NIM plate will act as a non-traditional lens. One exciting application of this negative refraction is superlensing, which would enable focusing superior to the diffraction limit. However, as no natural NIMs exist, it was only relatively recently that the first NIM was realized.

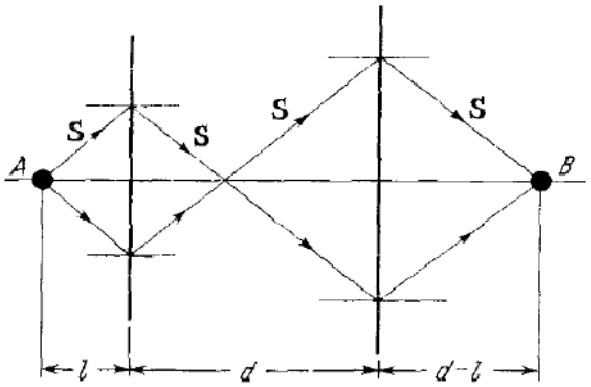

Figure 1.11 Passage of rays of light through a NIM plate of thickness d. The source of radiation is point A and the detector of radiation is point B. Recreated from Veselago.[82]

1.4 Optical Metamaterials

Traditional materials derive their properties from their constituent elements or atoms. These atoms form a structure that is referred to as the unit cell, which dictates the

properties of the material. This unit cell may vary for the same atoms. For example, carbon atoms can form hexagonal sheets as brittle graphite, or they can form a 3-d structure as strong diamond. Both are made of carbon, but have very different properties.

Metamaterials, on the other hand, are not dependent simply upon the atoms that comprise the material, but on the structures created by the atoms that comprise the material. The unit cell of metamaterials is often a well-defined structure that enables the material to display an effective macroscopic behavior. In the case of optical metamaterials, the unit cell is significantly smaller than the wavelength of the incident light, thus the light interacts with the unit cell and not the individual atoms that comprise the unit cell.

1.4.1 Negative Index Metamaterials

In the late 1990's John Pendry described the blueprints for manufacturing a metamaterial with a negative permittivity and a negative permeability. To generate the negative effective permittivity, ε_{eff}, Pendry proposed a structure of free standing wires that would result in a negative ε_{eff} at frequencies smaller than the plasmon frequency, ω_p, of the metal.[83, 84] The negative effective permeability, μ_{eff}, would be generated by concentric metal rings that were called split-ring resonators (SRRs).[85] The first NIM was a metamaterial which combined Pendry's array of millimeter-sized parallel wires and millimeter-sized SRRs.[86] The NIM operated at a frequency of 5 GHz. By incorporating the copper wire into the back of the SRR's circuit board, the construction of the NIM was simplified, while preserving the negative index property.[87]

The SRR behaves similar to a circuit with a capacitor and an inductor. The rings act as the inductors, while the splits act as capacitors. This is illustrated in Figure 1.12. Like an LC-circuit, the SRR has a resonant frequency, which is dependent upon the effective capacitance and the effective inductance of the SRR. By modifying the materials and the geometry of the SRR, it is possible to tune the SRR to different frequencies.[88-90] Figure 1.13 highlights some of the NIMs that have been fabricated using different sized SRRs that operate at different frequencies.

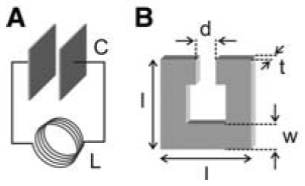

Figure 1.12 Illustration of the analogy between (A) an LC-circuit with inductance L and capacitance C, and (B) a horseshoe SRR. Image reproduced from Linden.[89]

The simplest form of a SRR is a cut-wire pair. An early attempt at fabricating NIMs using cut-wire pairs showed that the device produced negative values of ε and μ, but at separate, non-overlapping frequencies.[91] Another attempt demonstrated a NIM with cut-wire pairs, but this NIM only displayed a negative refractive index of n ~ -0.3.[92]

Recently, advances in NIMs have not actually dealt with true NIMs, but waveguides that exhibit NIM behaviors. [93-95] These NIMs use a fishnet type structure with alternating layers of metal and dielectric. The negative index of this structure arises from the combination of the permeability resonance resulting from the excitation of a gap surface plasmon polaration in the metal-dielectric-metal multilayer and the effective negative permeability that is governed by the cutoff frequency of the waveguide mode

supported by the holes.[93] The production of these fishnet structures often involves focused ion beam milling, which is very time consuming.

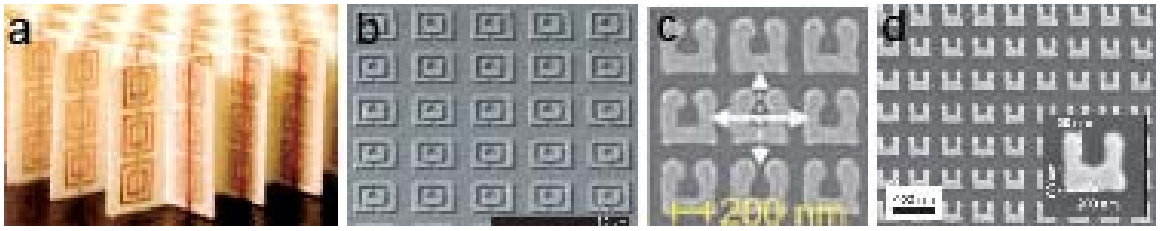

Figure 1.13 By shrinking the SRRs, the operating frequency increases from (a) the microwave range[87] to the (b) THz range[88], (c) Mid-IR range[89], and (d) Near-IR range[90]

1.4.2 Perfect Absorber Metamaterials

Metamaterials can also be fabricated to be perfect absorbers.[96-98] In this case, the metamaterial is designed such that the $\varepsilon_{eff}(\omega) = \mu_{eff}(\omega)$. The result of this design is that the impedance is matched to free space, which minimizes the reflectivity. Also, by maximizing the imaginary components of $\varepsilon_{eff}(\omega)$ and $\mu_{eff}(\omega)$, which correspond to the loss components of the optical constants, it is possible to achieve large absorbance. In the case of metals this is very easy, because the loss of $\varepsilon(\omega)$ increases exponentially around the plasma frequency. A perfect absorber metamaterial could be useful as a cloaking device for radar or as the active element in a bolometer.

1.5 Conclusions

There exist several methods to synthesize Au NPs and Au NRs. The surface plasmon resonances of Au NPs and Au NRs are dependent on the sizes of the Au NPs and Au NRs, which can be controlled via careful synthetic design. Furthermore, the surface plasmons may be tuned by assembling the Au NPs and Au NRs.

Despite the success of SRRs and waveguide-style NIMs, they are both limited in that they have only been produced via lithographic techniques. Lithography is ideal for one or two-dimensional structures, but not three-dimensional structures. Therefore, there exists a need for a technique which produces large quantities of SRRs. By synthesizing and assembling nanogold, it should be possible to generate building blocks for NIMs that can be randomly dispersed in a matrix at high enough concentrations to provide an isotropic negative index response.

1.6 References

1. Buffat, P.; Borel, J. P., Size effect on the melting temperature of gold particles. *Phys. Rev. A* **1976,** *13* (6), 2287.
2. Hutter, E.; Fendler, J. H., Exploitation of Localized Surface Plasmon Resonance. *Adv. Mater.* **2004,** *16* (19), 1685-1706.
3. Templeton, A. C.; Pietron, J. J.; Murray, R. W.; Mulvaney, P., Solvent Refractive Index and Core Charge Influences on the Surface Plasmon Absorbance of Alkanethiolate Monolayer-Protected Gold Clusters. *The Journal of Physical Chemistry B* **1999,** *104* (3), 564-570.
4. Link, S.; El-Sayed, M. A., Size and Temperature Dependence of the Plasmon Absorption of Colloidal Gold Nanoparticles. *The Journal of Physical Chemistry B* **1999,** *103* (21), 4212-4217.
5. Jana, N. R.; Gearheart, L.; Murphy, C. J., Seed-Mediated Growth Approach for Shape-Controlled Synthesis of Spheroidal and Rod-like Gold Nanoparticles Using a Surfactant Template. *Adv. Mater.* **2001,** *13* (18), 1389-1393.
6. Turkevich, J.; Stevenson, P. C.; Hillier, J., A study of the nucleation and growth processes in the synthesis of colloidal gold. *Discussions of the Faraday Society* **1951,** *11*, 55-75.
7. Kimling, J.; Maier, M.; Okenve, B.; Kotaidis, V.; Ballot, H.; Plech, A., Turkevich Method for Gold Nanoparticle Synthesis Revisited. *The Journal of Physical Chemistry B* **2006,** *110* (32), 15700-15707.
8. Frens, G., CONTROLLED NUCLEATION FOR REGULATION OF PARTICLE-SIZE IN MONODISPERSE GOLD SUSPENSIONS. *Nature-Physical Science* **1973,** *241* (105), 20-22.
9. Perrault, S. D.; Chan, W. C. W., Synthesis and Surface Modification of Highly Monodispersed, Spherical Gold Nanoparticles of 50−200 nm. *J. Am. Chem. Soc.* **2009,** *131* (47), 17042-17043.
10. Brust, M.; Walker, M.; Bethell, D.; Schiffrin, D. J.; Whyman, R., SYNTHESIS OF THIOL-DERIVATIZED GOLD NANOPARTICLES IN A 2-PHASE LIQUID-LIQUID SYSTEM. *J. Chem. Soc.-Chem. Commun.* **1994,** (7), 801-802.
11. Nikoobakht, B.; El-Sayed, M. A., Preparation and Growth Mechanism of Gold Nanorods (NRs) Using Seed-Mediated Growth Method. *Chem. Mat.* **2003,** *15* (10), 1957-1962.
12. Jana, N. R.; Gearheart, L.; Murphy, C. J., Wet Chemical Synthesis of High Aspect Ratio Cylindrical Gold Nanorods. *The Journal of Physical Chemistry B* **2001,** *105* (19), 4065-4067.
13. Jana, N. R.; Gearheart, L.; Murphy, C. J., Seeding Growth for Size Control of 5−40 nm Diameter Gold Nanoparticles. *Langmuir* **2001,** *17* (22), 6782-6786.
14. Yee, C. K.; Jordan, R.; Ulman, A.; White, H.; King, A.; Rafailovich, M.; Sokolov, J., Novel One-Phase Synthesis of Thiol-Functionalized Gold, Palladium, and Iridium Nanoparticles Using Superhydride. *Langmuir* **1999,** *15* (10), 3486-3491.
15. Corbierre, M. K.; Cameron, N. S.; Lennox, R. B., Polymer-stabilized gold nanoparticles with high grafting densities. *Langmuir* **2004,** *20* (7), 2867-2873.

16. Hiramatsu, H.; Osterloh, F. E., A simple large-scale synthesis of nearly monodisperse gold and silver nanoparticles with adjustable sizes and with exchangeable surfactants. *Chem. Mat.* **2004,** *16* (13), 2509-2511.
17. Yu; Chang, S.-S.; Lee, C.-L.; Wang, C. R. C., Gold Nanorods: Electrochemical Synthesis and Optical Properties. *The Journal of Physical Chemistry B* **1997,** *101* (34), 6661-6664.
18. Sau, T. K.; Murphy, C. J., Seeded High Yield Synthesis of Short Au Nanorods in Aqueous Solution. *Langmuir* **2004,** *20* (15), 6414-6420.
19. Liu; Guyot-Sionnest, P., Mechanism of Silver(I)-Assisted Growth of Gold Nanorods and Bipyramids. *The Journal of Physical Chemistry B* **2005,** *109* (47), 22192-22200.
20. Garg, N.; Scholl, C.; Mohanty, A.; Jin, R., The Role of Bromide Ions in Seeding Growth of Au Nanorods. *Langmuir* **2010,** *26* (12), 10271-10276.
21. Millstone, J. E.; Wei, W.; Jones, M. R.; Yoo, H.; Mirkin, C. A., Iodide Ions Control Seed-Mediated Growth of Anisotropic Gold Nanoparticles. *Nano Letters* **2008,** *8* (8), 2526-2529.
22. Smith, D. K.; Korgel, B. A., The Importance of the CTAB Surfactant on the Colloidal Seed-Mediated Synthesis of Gold Nanorods. *Langmuir* **2008,** *24* (3), 644-649.
23. Smith, D. K.; Miller, N. R.; Korgel, B. A., Iodide in CTAB Prevents Gold Nanorod Formation. *Langmuir* **2009,** *25* (16), 9518-9524.
24. Orendorff, C. J.; Murphy, C. J., Quantitation of Metal Content in the Silver-Assisted Growth of Gold Nanorods. *The Journal of Physical Chemistry B* **2006,** *110* (9), 3990-3994.
25. Carbó-Argibay, E.; Rodríguez-González, B.; Pacifico, J.; Pastoriza-Santos, I.; Pérez-Juste, J.; Liz-Marzán, L. M., Chemical Sharpening of Gold Nanorods: The Rod-to-Octahedron Transition. *Angewandte Chemie International Edition* **2007,** *46* (47), 8983-8987.
26. Wang, Z. L.; Mohamed, M. B.; Link, S.; El-Sayed, M. A., Crystallographic facets and shapes of gold nanorods of different aspect ratios. *Surface Science* **1999,** *440* (1-2), L809-L814.
27. Keul, H. A.; Möller, M.; Bockstaller, M. R., Structural Evolution of Gold Nanorods during Controlled Secondary Growth. *Langmuir* **2007,** *23* (20), 10307-10315.
28. Carbó-Argibay, E.; Rodríguez-González, B.; Gómez-Graña, S.; Guerrero-Martínez, A.; Pastoriza-Santos, I.; Pérez-Juste, J.; Liz-Marzán, L. M., The Crystalline Structure of Gold Nanorods Revisited: Evidence for Higher-Index Lateral Facets. *Angewandte Chemie International Edition* **2010,** *49* (49), 9397-9400.
29. Katz-Boon, H.; Rossouw, C. J.; Weyland, M.; Funston, A. M.; Mulvaney, P.; Etheridge, J., Three-Dimensional Morphology and Crystallography of Gold Nanorods. *Nano Letters* **2010,** *11* (1), 273-278.
30. Jin, R., Quantum sized, thiolate-protected gold nanoclusters. *Nanoscale* **2010,** *2* (3), 343-362.
31. Zhu, M.; Lanni, E.; Garg, N.; Bier, M. E.; Jin, R., Kinetically controlled, high-yield synthesis of Au-25 clusters. *J. Am. Chem. Soc.* **2008,** *130* (4), 1138-+.

32. Brust, M.; Schiffrin, D. J.; Bethell, D.; Kiely, C. J., Novel gold-dithiol nano-networks with non-metallic electronic properties. *Adv. Mater.* **1995,** *7* (9), 795-797.
33. Wu, Z.; Suhan, J.; Jin, R., One-pot synthesis of atomically monodisperse, thiol-functionalized Au25 nanoclusters. *J. Mater. Chem.* **2009,** *19* (5), 622-626.
34. Maye, M. M.; Chun, S. C.; Han, L.; Rabinovich, D.; Zhong, C. J., Novel spherical assembly of gold nanoparticles mediated by a tetradentate thioether. *J. Am. Chem. Soc.* **2002,** *124* (18), 4958-4959.
35. Maye, M. M.; Lim, I. I. S.; Luo, J.; Rab, Z.; Rabinovich, D.; Liu, T. B.; Zhong, C. J., Mediator-template assembly of nanoparticles. *J. Am. Chem. Soc.* **2005,** *127* (5), 1519-1529.
36. Maye, M. M.; Luo, J.; Lim, I. I. S.; Han, L.; Kariuki, N. N.; Rabinovich, D.; Liu, T. B.; Zhong, C. J., Size-controlled assembly of gold nanoparticles induced by a tridentate thioether ligand. *J. Am. Chem. Soc.* **2003,** *125* (33), 9906-9907.
37. Jain, P. K.; Eustis, S.; El-Sayed, M. A., Plasmon coupling in nanorod assemblies: Optical absorption, discrete dipole approximation simulation, and exciton-coupling model. *J. Phys. Chem. B* **2006,** *110* (37), 18243-18253.
38. Orendorff, C. J.; Hankins, P. L.; Murphy, C. J., pH-Triggered Assembly of Gold Nanorods. *Langmuir* **2005,** *21* (5), 2022-2026.
39. Caswell, K. K.; Wilson, J. N.; Bunz, U. H. F.; Murphy, C. J., Preferential End-to-End Assembly of Gold Nanorods by Biotin−Streptavidin Connectors. *J. Am. Chem. Soc.* **2003,** *125* (46), 13914-13915.
40. Gole, A.; Murphy, C. J., Biotin−Streptavidin-Induced Aggregation of Gold Nanorods: Tuning Rod−Rod Orientation. *Langmuir* **2005,** *21* (23), 10756-10762.
41. Sharma, J.; Chhabra, R.; Cheng, A.; Brownell, J.; Liu, Y.; Yan, H., Control of Self-Assembly of DNA Tubules Through Integration of Gold Nanoparticles. *Science* **2009,** *323* (5910), 112-116.
42. Park, S. Y.; Lytton-Jean, A. K. R.; Lee, B.; Weigand, S.; Schatz, G. C.; Mirkin, C. A., DNA-programmable nanoparticle crystallization. *Nature* **2008,** *451* (7178), 553-556.
43. Nykypanchuk, D.; Maye, M. M.; van der Lelie, D.; Gang, O., DNA-guided crystallization of colloidal nanoparticles. *Nature* **2008,** *451* (7178), 549-552.
44. Fava, D.; Nie, Z.; Winnik, M. A.; Kumacheva, E., Evolution of Self-Assembled Structures of Polymer-Terminated Gold Nanorods in Selective Solvents. *Adv. Mater.* **2008,** *20* (22), 4318-4322.
45. Nie, Z. H.; Fava, D.; Kumacheva, E.; Zou, S.; Walker, G. C.; Rubinstein, M., Self-assembly of metal-polymer analogues of amphiphilic triblock copolymers. *Nat. Mater.* **2007,** *6* (8), 609-614.
46. Nie, Z. H.; Fava, D.; Rubinstein, M.; Kumacheva, E., "Supramolecular" assembly of gold nanorods end-terminated with polymer "Pom-Poms": Effect of pom-pom structure on the association modes. *J. Am. Chem. Soc.* **2008,** *130* (11), 3683-3689.
47. Maury, P. A.; Reinhoudt, D. N.; Huskens, J., Assembly of nanoparticles on patterned surfaces by noncovalent interactions. *Current Opinion in Colloid & Interface Science* **2008,** *13* (1-2), 74-80.

48. Zhang, J.; Li, Y.; Zhang, X.; Yang, B., Colloidal Self-Assembly Meets Nanofabrication: From Two-Dimensional Colloidal Crystals to Nanostructure Arrays. *Adv. Mater.* **2010,** *22* (38), 4249-4269.
49. Crespo-Biel, O.; Ravoo, B. J.; Reinhoudt, D. N.; Huskens, J., Noncovalent nanoarchitectures on surfaces: from 2D to 3D nanostructures. *J. Mater. Chem.* **2006,** *16* (41), 3997-4021.
50. Kinge, S.; Crego-Calama, M.; Reinhoudt, D. N., Self-assembling nanoparticles at surfaces and interfaces. *ChemPhysChem* **2008,** *9* (1), 20-42.
51. Min, Y. J.; Akbulut, M.; Kristiansen, K.; Golan, Y.; Israelachvili, J., The role of interparticle and external forces in nanoparticle assembly. *Nat. Mater.* **2008,** *7* (7), 527-538.
52. Shenhar, R.; Norsten, T. B.; Rotello, V. M., Polymer-Mediated Nanoparticle Assembly: Structural Control and Applications. *Adv. Mater.* **2005,** *17* (6), 657-669.
53. Liu, G.; Luais, E.; Gooding, J. J., The Fabrication of Stable Gold Nanoparticle-Modified Interfaces for Electrochemistry. *Langmuir* **2011,** *27* (7), 4176-4183.
54. Liu, S.; Maoz, R.; Schmid, G.; Sagiv, J., Template Guided Self-Assembly of [Au55] Clusters on Nanolithographically Defined Monolayer Patterns. *Nano Letters* **2002,** *2* (10), 1055-1060.
55. Crespo-Biel, O.; Dordi, B.; Reinhoudt, D. N.; Huskens, J., Supramolecular layer-by-layer assembly: Alternating adsorptions of guest- and host-functionalized molecules and particles using multivalent supramolecular interactions. *J. Am. Chem. Soc.* **2005,** *127* (20), 7594-7600.
56. Huang, H. W.; Bhadrachalam, P.; Ray, V.; Koh, S. J., Single-particle placement via self-limiting electrostatic gating. *Appl. Phys. Lett.* **2008,** *93* (7).
57. Ma, L.-C.; Subramanian, R.; Huang, H.-W.; Ray, V.; Kim, C.-U.; Koh, S. J., Electrostatic Funneling for Precise Nanoparticle Placement: A Route to Wafer-Scale Integration. *Nano Letters* **2007,** *7* (2), 439-445.
58. Manandhar, P.; Akhadov, E. A.; Tracy, C.; Picraux, S. T., Integration of Nanowire Devices in Out-of-Plane Geometry. *Nano Letters* **2010,** *10* (6), 2126-2132.
59. Maury, P.; Escalante, M.; Reinhoudt, D. N.; Huskens, J., Directed assembly of nanoparticles onto polymer-imprinted or chemically patterned templates fabricated by nanoimprint lithography. *Adv. Mater.* **2005,** *17* (22), 2718-+.
60. Ofir, Y.; Samanta, B.; Xiao, Q.; Jordan, B. J.; Xu, H.; Arumugam, P.; Arvizo, R.; Tuominen, M. T.; Rotello, V. M., Polyelectrolyte negative resist patterns as templates for the electrostatic assembly of nanoparticles and electroless deposition of metallic films. *Adv. Mater.* **2008,** *20* (13), 2561-2566.
61. Xu, H.; Hong, R.; Wang, X. Y.; Arvizo, R.; You, C. C.; Samanta, B.; Patra, D.; Tuominen, M. T.; Rotello, V. M., Controlled formation of patterned gold films via site-selective deposition of nanoparticles onto polymer-templated surfaces. *Adv. Mater.* **2007,** *19* (10), 1383-+.
62. Zhu, T.; Zhang, X.; Wang, J.; Fu, X. Y.; Liu, Z. F., Assembling colloidal Au nanoparticles with functionalized self-assembled monolayers. *Thin Solid Films* **1998,** *327*, 595-598.

63. Lee, H.; You, S.; Pikhitsa, P. V.; Kim, J.; Kwon, S.; Woo, C. G.; Choi, M., Three-Dimensional Assembly of Nanoparticles from Charged Aerosols. *Nano Letters* **2010,** *11* (1), 119-124.
64. Zheng, H. P.; Lee, I.; Rubner, M. F.; Hammond, P. T., Two component particle arrays on patterned polyelectrolyte multilayer templates. *Adv. Mater.* **2002,** *14* (8), 569-572.
65. Li, Q.; Zheng, J.; Liu, Z., Site-Selective Assemblies of Gold Nanoparticles on an AFM Tip-Defined Silicon Template. *Langmuir* **2002,** *19* (1), 166-171.
66. Ling, X.; Zhu, X.; Zhang, J.; Zhu, T.; Liu, M.; Tong, L.; Liu, Z., Reproducible Patterning of Single Au Nanoparticles on Silicon Substrates by Scanning Probe Oxidation and Self-Assembly. *The Journal of Physical Chemistry B* **2005,** *109* (7), 2657-2665.
67. Liu, S. T.; Maoz, R.; Sagiv, J., Planned nanostructures of colloidal gold via self-assembly on hierarchically assembled organic bilayer template patterns with in-situ generated terminal amino functionality. *Nano Letters* **2004,** *4* (5), 845-851.
68. Zheng, J. W.; Zhu, Z. H.; Chen, H. F.; Liu, Z. F., Nanopatterned assembling of colloidal gold nanoparticles on silicon. *Langmuir* **2000,** *16* (10), 4409-4412.
69. Cui, Y.; Björk, M. T.; Liddle, J. A.; Sönnichsen, C.; Boussert, B.; Alivisatos, A. P., Integration of Colloidal Nanocrystals into Lithographically Patterned Devices. *Nano Letters* **2004,** *4* (6), 1093-1098.
70. Fustin, C. A.; Glasser, G.; Spiess, H. W.; Jonas, U., Parameters influencing the templated growth of colloidal crystals on chemically patterned surfaces. *Langmuir* **2004,** *20* (21), 9114-9123.
71. Ling, X. Y.; Malaquin, L.; Reinhoudt, D. N.; Wolf, H.; Huskens, J., An in situ study of the adsorption behavior of functionalized particles on self-assembled monolayers via different chemical interactions. *Langmuir* **2007,** *23* (20), 9990-9999.
72. Malaquin, L.; Kraus, T.; Schmid, H.; Delamarche, E.; Wolf, H., Controlled particle placement through convective and capillary assembly. *Langmuir* **2007,** *23* (23), 11513-11521.
73. Varghese, B.; Cheong, F. C.; Sindhu, S.; Yu, T.; Lim, C. T.; Valiyaveettil, S.; Sow, C. H., Size selective assembly of colloidal particles on a template by directed self-assembly technique. *Langmuir* **2006,** *22* (19), 8248-8252.
74. Yin, Y. D.; Xia, Y. N., Self-assembly of monodispersed spherical colloids into complex aggregates with well-defined sizes, shapes, and structures. *Adv. Mater.* **2001,** *13* (4), 267-+.
75. Lee, J. H.; Wu, Q.; Park, W., Metal nanocluster metamaterial fabricated by the colloidal self-assembly. *Opt. Lett.* **2009,** *34* (4), 443-445.
76. Xia, Y.; Yin, Y.; Lu, Y.; McLellan, J., Template-Assisted Self-Assembly of Spherical Colloids into Complex and Controllable Structures. *Adv. Funct. Mater.* **2003,** *13* (12), 907-918.
77. Sohn, B. H.; Seo, B. H., Fabrication of the Multilayered Nanostructure of Alternating Polymers and Gold Nanoparticles with Thin Films of Self-Assembling Diblock Copolymers. *Chem. Mat.* **2001,** *13* (5), 1752-1757.
78. Mendoza, C.; Pietsch, T.; Gutmann, J. S.; Jehnichen, D.; Gindy, N.; Fahmi, A., Block Copolymers with Gold Nanoparticles: Correlation between Structural

Characteristics and Mechanical Properties. *Macromolecules* **2009,** *42* (4), 1203-1211.
79. Sohn, B.-H.; Choi, J.-M.; Yoo, S. I.; Yun, S.-H.; Zin, W.-C.; Jung, J. C.; Kanehara, M.; Hirata, T.; Teranishi, T., Directed Self-Assembly of Two Kinds of Nanoparticles Utilizing Monolayer Films of Diblock Copolymer Micelles. *J. Am. Chem. Soc.* **2003,** *125* (21), 6368-6369.
80. Mendoza, C.; Gindy, N.; Gutmann, J. S.; Frömsdorf, A.; Förster, S.; Fahmi, A., In Situ Synthesis and Alignment of Au Nanoparticles within Hexagonally Packed Cylindrical Domains of Diblock Copolymers in Bulk. *Langmuir* **2009,** *25* (16), 9571-9578.
81. Chan, Y. N. C.; Schrock, R. R.; Cohen, R. E., Synthesis of silver and gold nanoclusters within microphase-separated diblock copolymers. *Chem. Mat.* **1992,** *4* (1), 24-27.
82. Veselago, V. G., ELECTRODYNAMICS OF SUBSTANCES WITH SIMULTANEOUSLY NEGATIVE VALUES OF SIGMA AND MU. *Soviet Physics Uspekhi-Ussr* **1968,** *10* (4), 509-&.
83. Pendry, J. B.; Holden, A. J.; Robbins, D. J.; Stewart, W. J., Low frequency plasmons in thin-wire structures. *J. Phys.-Condes. Matter* **1998,** *10* (22), 4785-4809.
84. Pendry, J. B.; Holden, A. J.; Stewart, W. J.; Youngs, I., Extremely Low Frequency Plasmons in Metallic Mesostructures. *Phys. Rev. Lett.* **1996,** *76* (25), 4773.
85. Pendry, J. B.; Holden, A. J.; Robbins, D. J.; Stewart, W. J., Magnetism from conductors and enhanced nonlinear phenomena. *Microwave Theory and Techniques, IEEE Transactions on* **1999,** *47* (11), 2075-2084.
86. Smith, D. R.; Padilla, W. J.; Vier, D. C.; Nemat-Nasser, S. C.; Schultz, S., Composite Medium with Simultaneously Negative Permeability and Permittivity. *Phys. Rev. Lett.* **2000,** *84* (18), 4184.
87. Shelby, R. A.; Smith, D. R.; Schultz, S., Experimental verification of a negative index of refraction. *Science* **2001,** *292* (5514), 77-79.
88. Yen, T. J.; Padilla, W. J.; Fang, N.; Vier, D. C.; Smith, D. R.; Pendry, J. B.; Basov, D. N.; Zhang, X., Terahertz magnetic response from artificial materials. *Science* **2004,** *303* (5663), 1494-1496.
89. Linden, S.; Enkrich, C.; Wegener, M.; Zhou, J. F.; Koschny, T.; Soukoulis, C. M., Magnetic response of metamaterials at 100 terahertz. *Science* **2004,** *306* (5700), 1351-1353.
90. Enkrich, C.; Wegener, M.; Linden, S.; Burger, S.; Zschiedrich, L.; Schmidt, F.; Zhou, J. F.; Koschny, T.; Soukoulis, C. M., Magnetic Metamaterials at Telecommunication and Visible Frequencies. *Phys. Rev. Lett.* **2005,** *95* (20), 203901.
91. Dolling, G.; Enkrich, C.; Wegener, M.; Zhou, J. F.; Soukoulis, C. M.; Linden, S., Cut-wire pairs and plate pairs as magnetic atoms for optical metamaterials. *Opt. Lett.* **2005,** *30* (23), 3198-3200.
92. Shalaev, V. M.; Cai, W. S.; Chettiar, U. K.; Yuan, H. K.; Sarychev, A. K.; Drachev, V. P.; Kildishev, A. V., Negative index of refraction in optical metamaterials. *Opt. Lett.* **2005,** *30* (24), 3356-3358.

93. Garcia-Meca, C.; Hurtado, J.; Marti, J.; Martinez, A.; Dickson, W.; Zayats, A. V., Low-Loss Multilayered Metamaterial Exhibiting a Negative Index of Refraction at Visible Wavelengths. *Phys. Rev. Lett.* **2011,** *106* (6).
94. Xiao, S.; Drachev, V. P.; Kildishev, A. V.; Ni, X.; Chettiar, U. K.; Yuan, H.-K.; Shalaev, V. M., Loss-free and active optical negative-index metamaterials. *Nature* **2010,** *466* (7307), 735-738.
95. Burgos, S. P.; de Waele, R.; Polman, A.; Atwater, H. A., A single-layer wide-angle negative-index metamaterial at visible frequencies. *Nat Mater* **2010,** *9* (5), 407-412.
96. Landy, N. I.; Sajuyigbe, S.; Mock, J. J.; Smith, D. R.; Padilla, W. J., Perfect metamaterial absorber. *Phys. Rev. Lett.* **2008,** *100* (20).
97. Tao, H.; Landy, N. I.; Bingham, C. M.; Zhang, X.; Averitt, R. D.; Padilla, W. J., A metamaterial absorber for the terahertz regime: design, fabrication and characterization. *Opt. Express* **2008,** *16* (10), 7181-7188.
98. Cheng, Y.; Yang, H., Design, simulation, and measurement of metamaterial absorber. *Journal of Applied Physics* **2010,** *108* (3), 034906-4.

Chapter 2

Directed Self-Assembly of Gold Nanoparticles Using a Chemically Patterned Template

2.1 Introduction

To create building blocks from nanogold for metamaterials, it is necessary to assemble the nanogold. Inspired from the works of Lee[1] and Maury[2], a bottom-up approach was conceived where electrostatics would be used to self-assemble nanogold on a chemically patterned template. The relative sizes of the nanogold and the chemical pattern would dictate the number of nanogold elements that self-assembled on the chemical pattern. To test the control of this technique, gold nanoparticles (Au NPs) were patterned first. The following sections describe the fabrication of aminosilane chemical templates and the variables that affect how citrate-capped Au NPs electrostatically self-assemble on the aminosilane chemical template. A scheme for the aminosilane chemical template fabrication and Au NP self-assembly is illustrated in Figure 2.1

2.2 Experimental Methods

N-type/phosphorus Si <100> wafers were purchased from Silicon Valley Microelectronics. Poly(methyl methacrylate) (PMMA, PMMA 950k A2) was purchased from MicroChem. All other chemicals were purchased from Sigma Aldrich and used as received.

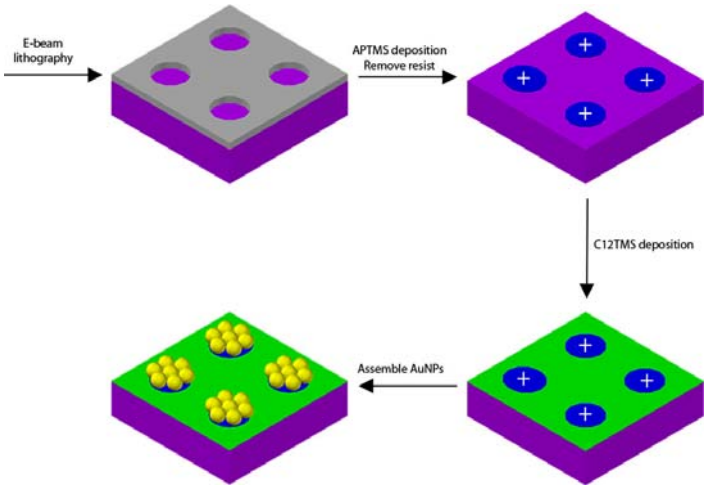

Figure 2.1 Schematic for the self-assembly of Au NPs on an aminsilane chemical template. PMMA is spin-ccast on a Si wafer. After e-beam lithography and development of the dot patterns, aminosilane is deposited in the patterned areas via gas-phase silanization. After removing the remaining PMMA resist, the freshly exposed Si surface is coated with an alkylsilane. Finally, the sample is dipped into a solution of citrate-capped Au NPs to induce self-assembly.

2.2.1 Nanopattern Generation

A 45 nm layer of thermal oxide was grown on the Si wafers. Oxide thickness was checked using ellipsometry. After a dehydration bake at 150°C for 5 min. on a hot plate, PMMA resist (PMMA 950k A2, MicroChem) was spin-coat onto the wafer at 4000 rpm for 60 sec. to obtain a resist thickness of ~ 65 nm. A pre-bake was then performed by heating the wafer at 170°C in an oven for 30 min.

Electron-beam lithography (EBL) was performed at 20 keV with at 10 μm aperture using a Raith 150 (Raith). 10 by 10 μm arrays of dots were fabricated with a 500 nm pitch for multiple exposure doses (10, 20, 30, … 100 fC) per sample with a large crosshair for easy visibility. After exposure, samples were developed by immersing samples in a 1:3 (v/v) mixture of MIBK and IPA for 20 sec., immersing samples in IPA for 30 sec., and drying the samples under a stream of N_2. O_2 plasma reactive ion etching

(250 mT, 17% O2, 80 W, 15 s) was used to remove any trace organics from the wafer surface after development.

To image the patterns, 10 Å of Ti and 200 Å of Au were deposited using an SJ-20 electron-beam evaporator. Lift-off was done by immersing the sample in chloroform overnight. The sizes of the gold dots were measured by using the Analyze Particles function in the ImageJ software on SEM images of the gold dots.

2.2.2 Silanization

3-aminopropyltrimethoxy silane (APTMS, 97%), 3-aminopropyldimethylethoxy silane (APDMES, 97%), and dodecyltrimethoxysilane (C12TMS, 95%) were used without any purification. Silanization of the nanopatterned sample was performed by placing the samples into a desiccator with 100 μL of silane in a watch glass, pulling a vacuum, and leaving the desiccator overnight. Samples were then rinsed with MeOH and D.I. H_2O, and blown dry with Ar gas. Samples being functionalized with APDMES were placed on a hot plate at 50°C for 3 hrs. Samples being functionalized with the other silanes were placed on a 140°C hotplate for 30 min.

Contact angles were measured using a horizontally oriented stereo-microscope with a digital camera and in-house software.

2.2.3 Gold nanoparticle synthesis

Gold nanoparticles (Au NPs) were synthesized as reported elsewhere.[3] A 100 mL solution of 1 wt% $HAuCl_4$:$3H_2O$ (Sigma) in D.I. H_2O was brought to a boil under stirring and 1.00, 0.930, or 0.860 mL of 10 wt% trisodium citrate (Sigma) in water was added to

the solution to obtain 30, 37, and 50 nm diameter Au NPs, respectively. The solution turned bluish, then purplish, and eventually a bright red, indicating Au NP formation. The reaction was allowed to run for 10 min. before removing the solution from heat and transferring the solution to 20 mL vials. These vials were stored in the refrigerator until used. UV-Vis (Cary UV-Vis Bio 50, Varian) was used to observe the surface plasmon absorbance of the Au NPs.

TEM samples were prepared by drop casting 5 μL of the Au NP solution onto a carbon-coated copper TEM grid (Ted Pella) and allowing the solvent to evaporate. TEM was used to characterize the size of the Au NPs using a JEOL 3011 HRTEM at 300 keV.

2.2.4 Self-Assembly of Gold Nanoparticles

Silanized nanopatterns were rinsed for 5 sec. with chloroform and dried under an Ar stream to remove the unexposed PMMA and to expose the SiO_2 surface. Samples were then placed into a "flat-mouth" alligator clip and fixed to the arm of a vertical dipper (Microslide stage with NSC-1S controller, Newmark Systems) using double-stick tape. The sample was then lowered into 5 mL of the Au NP solution. The solution was contained in a sawed-off bottom of a 20 mL vial. In a typical experiment, the sample remained immersed in the Au NP solution for 20 min. before being withdrawn from the solution at 10 μm/s. The withdrawal rate was controlled by the dipper control software. Assemblies of Au NPs were imaged using SEM on an FEI Nova Nanolab FIB/SEM at 10 keV.

2.3 Salt concentration

Sodium chloride (Sigma) was used to create a 0.1 M solution in D.I. water. To obtain the desired concentrations of NaCl in the Au NP solution, x mL of 0.1 M NaCl solution was mixed with 5.0 – x mL of Au NP solution. For 1, 2, 5, and 10 mM NaCl concentrations, x = 0.05, 0.10, 0.25, and 0.50 mL, respectively. Unless noted otherwise, solutions were prepared by first adding 4 mL of Au NP solution, then x mL of NaCl solution, and finally 1 – x mL of Au NP solution.

To test the effects of when the NaCl is added to the Au NP solution, a 1.0 M solution of NaCl in D.I. water was created. First a small volume (100, 150, 200, 300, 500, 900 μL) of the Au NP solution was added to a UV-Vis cuvette. Then, 5 μL of the 1 M NaCl solution was added to the cuvette. After shaking the cuvette to ensure good mixing, another small volume of Au NP solution was added to bring the total volume of the solution to 1 mL. The final NaCl concentration of all solutions was 5 mM. UV-Vis was used to characterize the solutions after adding the NaCl and after adding the final volume of Au NP solution.

2.4 Results and Discussion

EBL was performed on pieces of Si wafer that had been spin-cast with a 65 nm thick PMMA resist to create arrays of dots. After developing the nanopatterns and a quick O_2 plasma cleaning, the nanopatterns were given a positive charge by functionalizing the exposed Si with an aminosilane via gas-phase silanization in a desiccator under vacuum. Once functionalized, the sample was rinsed with chloroform to remove the unexposed PMMA resist, dried under Ar gas, and then dipped into an

aqueous solution of citrate-capped Au NPs. The negatively charged, citrate-capped Au NPs self-assemble on the positively charged nanopatterns via an electrostatic interaction. The self-assembled Au NPs were then observed via scanning electron microscopy (SEM).

2.4.1 Wafer Preparation

EBL is essentially a SEM that is used to pattern a polymer resist. The electrons from the SEM will cut the bonds of the resist or cross-link the resist in a positive or negative resist, respectively.[4] However, the electrons also interact with the sample substrate. Figure 2.2 shows Monte Carlo simulations of the interaction between the electron beam and a typical EBL sample. While a large amount of electrons are forward scattered, there also are a significant number of electrons that are backscattered. The forward scattered electrons tend to broaden the initial beam diameter and can significantly contribute to the resist exposure. The increase in effective beam diameter, d_f, in nanometers due to forward scattered is given by the formula

$$d_f = 0.9(R_t/V_b)^{1.5}, \quad (1)$$

where R_t is the resist thickness in nanometers and V_b is the beam voltage in kilovolts. The backscattered electrons can contribute to the proximity effect, which is indirect exposure of areas adjacent to the incident electron beam. The amount of backscattered electrons depends on the incident beam energy, the substrate material, and the resist thickness. Thus, it becomes a game of compromises to limit the effects of both the back and forward scattered electrons.

One way to reduce the electron scattering is by growing a layer of SiO_2 on the Si wafer. The SiO_2 acts as an electron trap, which helps to reduce the number of scattered electrons.[5, 6] This, in turn, helps promote high-resolution EBL with limited undercutting from the proximity effect.

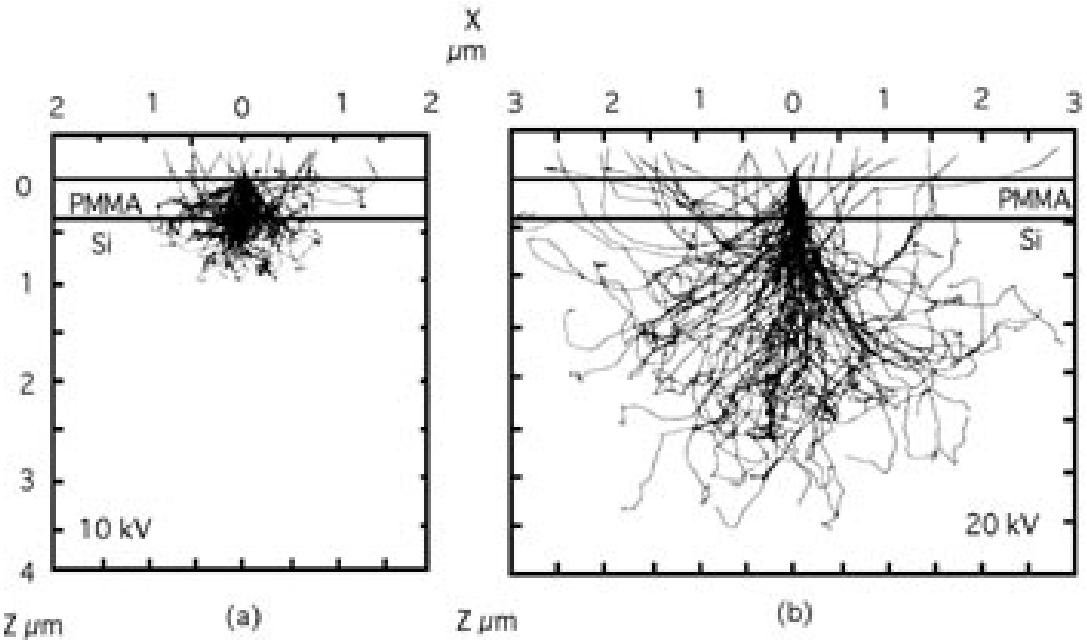

Figure 2.2 Monte Carlo simulations of the electron beam interaction with a PMMA coated Si wafer at beam accelerating voltages of (left) 10 kV and (right) 20 kV. Image reproduced from McCord.[4]

2.4.2 Nanopatterning

EBL was performed on pieces of Si wafer that had been spin-cast with a 65 nm thick PMMA resist to create arrays of dots. Dots were generated by focusing the electron beam on a specific point until the desired exposure dose was achieved. The size of the dots generated by EBL was controlled by varying the exposure dose of the electron beam in the PMMA resist. As shown in Figure 2.3, dot size increases as the exposure dose is increased. This technique can be used until the exposure dose is greater than 200 fC, at

which point the electron beam begins to cross-link the PMMA resist. The cross-linked PMMA is not removed during development, and is therefore undesirable.

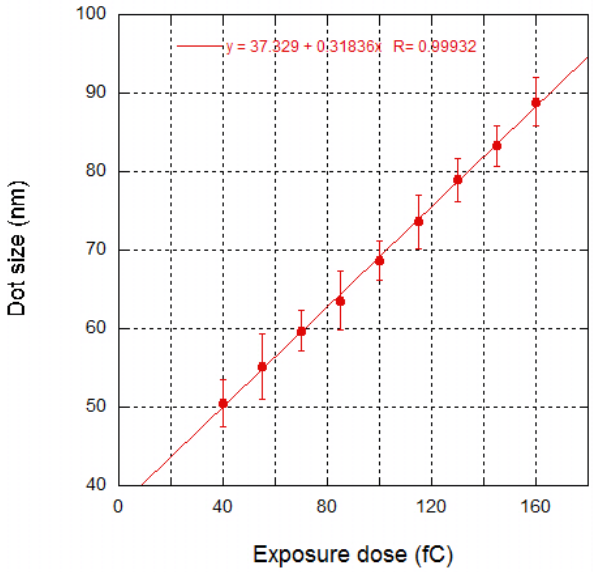

Figure 2.3 Correlation between the diameter of the nanodots and the e-beam exposure dose. Larger patterns can be produced by increasing the exposure dose. The linear regression line and equation are included.

2.4.3 Silanization

While APTMS is commonly used to direct the electrostatic self-assembly of negatively charged Au NPs on Si substrates, it is often used in conjunction with another functional molecule that repels or prevents the Au NPs from non-specifically depositing on the non-aminosilane patterned areas[7-11]. In other cases, the resist remains on the Si surface to enable easy removal of non-specifically bound Au NPs[7, 12].

The initial design of the chemical template for the electrostatic self-assembly of Au NPs consisted of dots of positively charged APTMS surrounded by dodecyltrimethoxysilane (C12TMS). The hydrophobic C12TMS would prevent any non-specific deposition of Au NPs. However, this design was unsuccessful.

The first plan was to deposit the aminosilane first, remove the resist, and then deposit the C12TMS. This protocol proved to be successful in directing the self-assembly of the Au NPs. However, using APTMS resulted in the formation of a raised halo around which the nanoparticles would assemble, as seen in Figure 2.4a. This halo was most likely due to the gellation of the APTMS during the gas phase silanization.[13] In order to prevent the formation of this halo, 3-aminopropyldimethylethoxysilane (APDMES) was used to functionalize the nanopatterns. APDMES features only one ethoxy-group, which deters the self-gellation during gas-phase silanization, but still enables monolayer formation and nanoparticle assembly, as seen in Figure 2.4b.

By swapping the aminosilanes, a problem arose. Depositing C12TMS after removing the resist caused the entire surface to become hydrophobic and no Au NPs would self-assemble. Since the APDMES neither gels, nor has the ability to cross-link like the APTMS, it appears that the C12TMS would deposit between adjacent APDMES molecules and render the dot hydrophobic due to the long alkyl chain of the C12TMS.

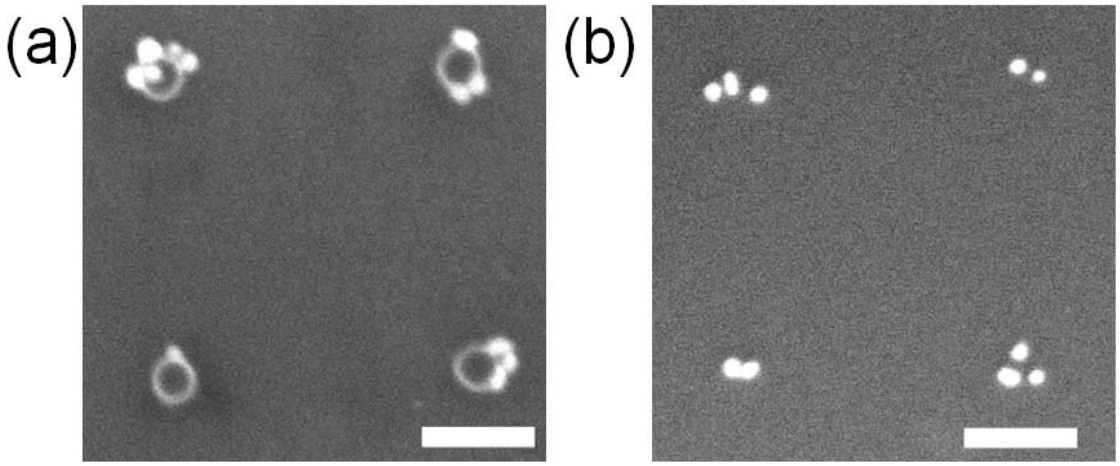

Figure 2.4 Self-assembled gold nanoparticles on (a) APTMS and (b) APDMES nanopatterns. The halos that form on the APTMS nanopatterns are not present in the APDMES nanopatterns because APDMES only has a single ethoxy group and cannot gellate like APTMS which has three methoxy groups. Scale bars are 200 nm.

The next design for the chemical template involved depositing the C12TMS before spinning the PMMA. This would ensure that the entire wafer was already hydrophobic when the resist was removed. It would still be possible to pattern the dots and give them a positive charge with the APDMES, since an O_2 plasma treatment after development would clean the surface and allow for the APDMES to bind to the surface.

However, this design was flawed. After spin-casting, there was not a uniform layer of PMMA on the wafer, as seen in Figure 2.5. The hydrophobic C12TMS prevented good wetting of the PMMA resist. The contact angle of water on C12TMS is 100°, but the contact angle of water on PMMA is 70°. Since the C12TMS surface is of lower energy than the PMMA, the PMMA cannot successfully wet the surface.

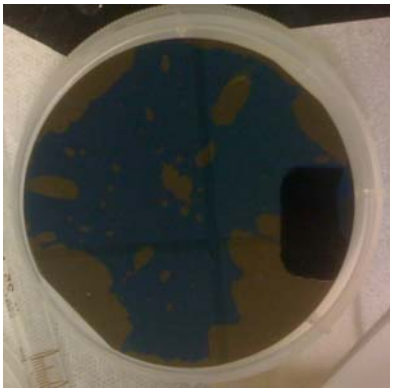

Figure 2.5 An example of a poorly spun-casted PMMA film on a C12TMS coated Si wafer. The blue areas are the PMMA.

A workaround to this problem was created. Rather than allowing the silanization of the C12TMS to occur overnight, the silanization was stopped after 3 hrs. The contact angle of the surface was found to be ~70°, which indicates an incomplete monolayer had formed. Due to the lower contact angle, the PMMA was able to spin cast on the wafer

successfully. This workaround was used to successfully pattern the Au NPs, but another, superior system was discovered.

It was found that the bare SiO_2 was perfectly capable of preventing non-specific binding of the Au NPs while allowing the directed self-assembly of the Au NPs on the APDMES dots. This was preferred over the incomplete monolayer of C12TMS because it did not have to rely upon a technique that produced a random, albeit functional, result. Thus, the final system for the electrostatic self-assembly of Au NPs on a chemical template was determined. The scheme for this system is illustrated in Figure 2.6.

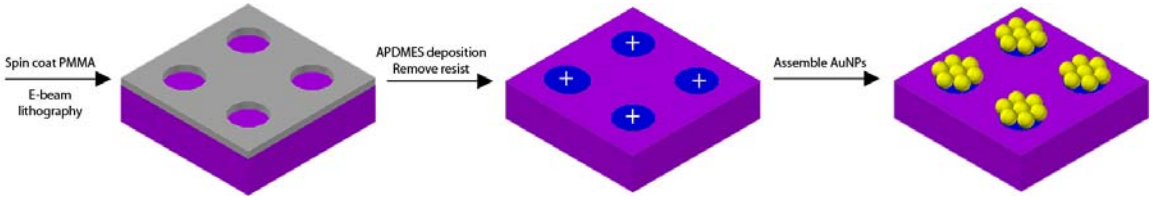

Figure 2.6 Scheme for creating the chemical template and patterning gold nanoparticles. PMMA is spun-coated on a Si wafer. After e-beam lithography and development of the dot patterns, aminosilane is deposited in the patterned areas via gas-phase silanization. After removing the remaining PMMA resist, the sample is dipped into a solution of citrate-capped Au NPs to induce self-assembly.

2.4.4 Size Effects on Self-Assembly

Monomers, dimers, trimers, and quatramers of 37 nm diameter, citrate-capped Au NPs are formed on 41, 50, 56, and 69 nm diameter aminosilane nanodots, as seen in Figure 2.7a-d. The number of Au NPs that assemble on the positively charged nanodot should increase as the size of the nanodot increases. It was previously reported that colloids would assemble until the electric field of the negatively charged colloids compensated for the electric field of the positively charged chemical template.[1, 12] Therefore, if the size of the Au NPs are altered, then it should be expected that different numbers of nanoparticles will assemble on the same sized nanodot.

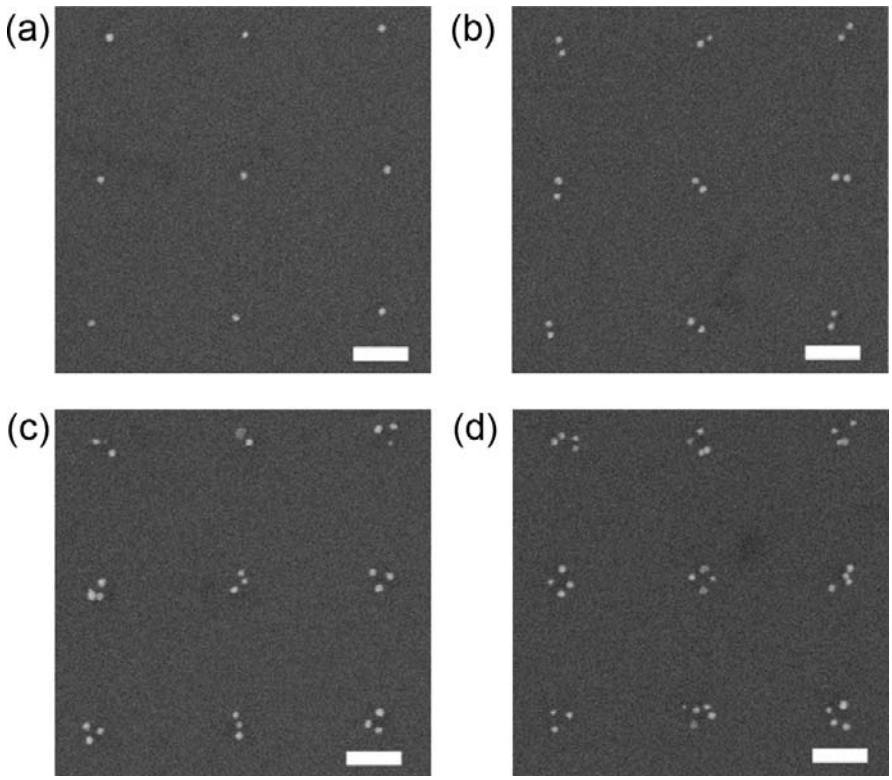

Figure 2.7 Gold nanoparticles assembled as (a) monomers, (b) dimers, (c) trimers, and (d) quatramers on 41, 50, 56, and 69 nm diameter nanodots, respectively. Scale bars are 200 nm.

Citrate-capped Au NPs were synthesized[3] with 29.6 ± 4.5, 36.5 ± 5.1, and 50.3 ± 10.3 nm diameters. Figure 2.8 shows the number of Au NPs that assembled on different sized nanodots for the 30, 37, and 50 nm diameter Au NPs. As expected, as the size of the nanoparticle increases, the number of nanoparticles that deposit decreases for the same sized pattern. This is a result of the increased negative electric field of one nanoparticle due to the increased size and surface area of larger Au NPs. Thus, fewer Au NPs are necessary to compensate for the electric field of the positively charged aminosilane nanodot. The variance in the number of Au NPs that assemble on the nanodot is due to the variance in the size of both the Au NPs and the nanodots. If it were possible to manufacture monodisperse Au NPs and nanodots, it would be expected that the number

of nanoparticles that assemble on a nanodot would be more uniform. Furthermore, the choice in Au NP size was limited by the EBL's theoretical, 20 nm feature resolution limit.

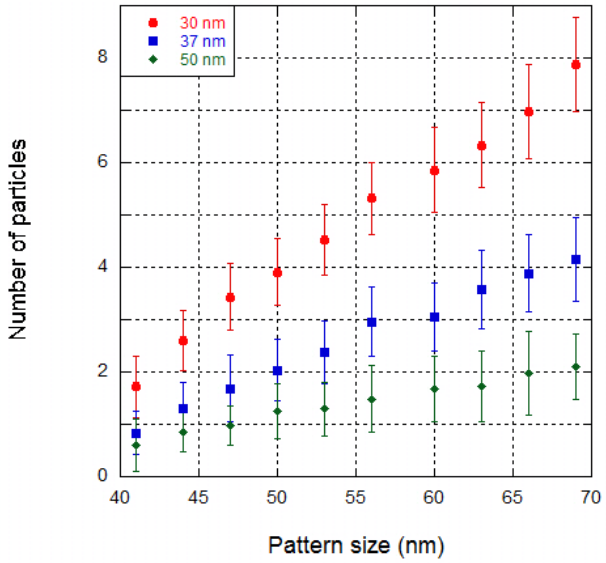

Figure 2.8 Plot of the number of particles that assemble on nanodots for different sized nanoparticles.

2.4.5 pH Sensitivity of the Electrostatic Self-Assembly

The electrostatic self-assembly of the Au NPs is pH sensitive. The Au NPs are capped with citrate molecules, which feature three carboxylic acid groups. The pKa value of the carboxylic acid group is 4.5. Thus, at pH's above 4.5, the Au NPs maintain their negative charge. The UV-Vis spectra shown in Figure 2.9 shows the absorption spectra for citrate capped Au NP solutions at different pH's. While the spectra at pH's of 7.0 and 9.5 look the same, the spectra at pH = 2.5 is much broader. The broad peak is a sign of Au NP aggregation. Since the pH of the solution is lower than the pKa value of the carboxylic acids on the citrate, the carboxylic groups protonate. As a result of this

protonation, the Au NPs no longer have a charge-charge repulsion to stabilize them and they begin to aggregate.

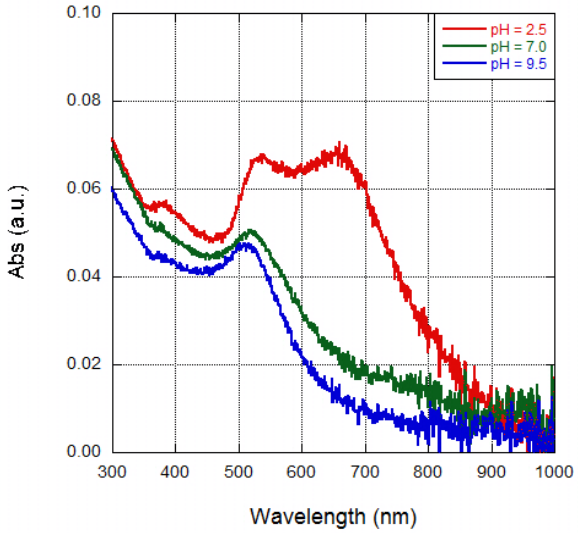

Figure 2.9 UV-Vis spectra of citrate capped Au NPs at different pH's. The broad peak around 670 nm for the pH = 2.5 indicates aggregation.

The aminosilane features a primary amine group. The pKa value of the amine is ~9.5. Therefore, at pH values above 9.5, the amine deprotonates to a neutral state. The pH sensitivity of the aminosilane's ability to direct electrostatic self-assembly is illustrated in Figure 2.10a. To test the pH sensitivity, an APDMES patterned sample was first immersed in a citrate capped Au NP solution with a pH = 11, imaged via SEM, then immersed in a citrate capped Au NP solution with a pH = 6, and imaged again with SEM. The SEM image in Figure 2.10b shows that the Au NP solution with a pH = 11 does not pattern on the APDMES cross, save for a few instances where there are clumps of aggregated Au NPs. These patterned Au NPs are most-likely due to localized pH fluctuations. However, after reimmersing the same sample in the pH = 6 solution, excellent Au NP patterning was achieved, as seen in Figure 2.10c. Thus, the electrostatic self-assembly is sensitive to the pH of the Au NP solution.

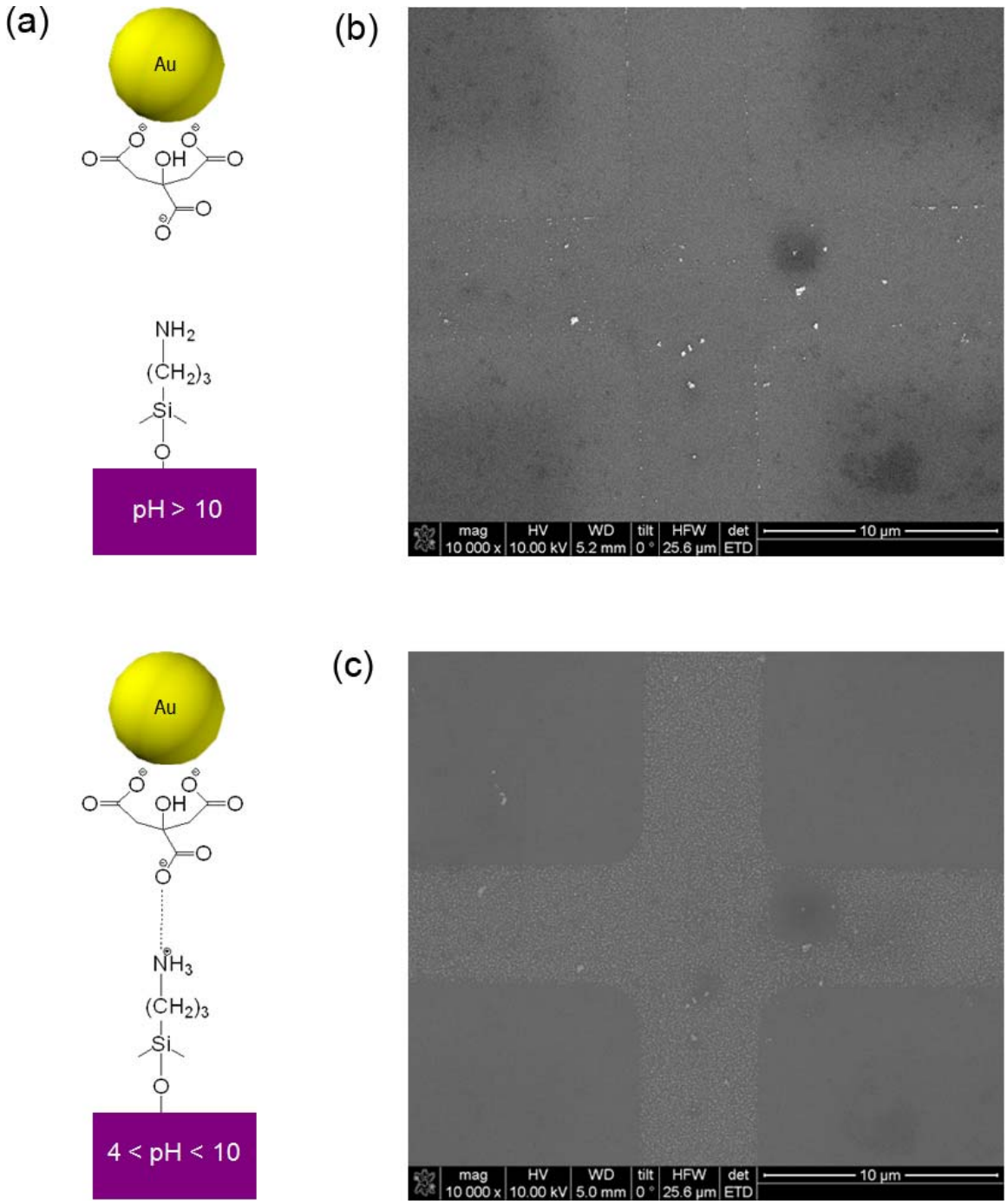

Figure 2.10 The pH sensitivity of the electrostatic self-assembly of citrate capped Au NPs on aminosilane patterns. (a) An illustration of the deprotonation and protonation of the aminosilane at basic and neutral pH's, respectively. The electrostatic attraction is only possible while the aminosilane is protonated to an NH_3^+ state. (b) An SEM micrograph of a large cross patterned with APDMES after immersion in a citrate capped Au NP solution with a pH = 11. Minimal Au NPs are self-assembled. (c) An SEM micrograph of the same large cross after it was immersed in a second solution of citrate capped Au NPs with a pH = 6. Excellent patterning of the Au NPs is visible, highlighting the pH sensitivity of the Au NP assembly.

2.4.6 Effects of Self-Assembly Time

In previous work on the electrostatic assembly of nanoparticles, substrates were left in the nanoparticle solutions overnight to reach equilibrium.[12] However, the electrostatic assembly should be rather quick due to the strong long-range attraction between the negatively charged particles and the positively charged nanopattern. In order to determine exactly how long this system takes to reach equilibrium, samples were immersed in 50 nm Au NP solutions for 10, 20, 30 and 60 minutes. The number of Au NPs that assemble on different sizes of aminosilane nanodots for the aforementioned immersion times is visualized in Figure 2.11 and summarized in Table 2.1. The standard deviations were omitted from Figure 2.11 for clarity, but in Table 2.1 it shows the standard deviations were less than 1 for all data points. Thus, it can be concluded that there is no difference in the number of Au NPs that assemble depending if the immersion time is greater than 10 minutes.

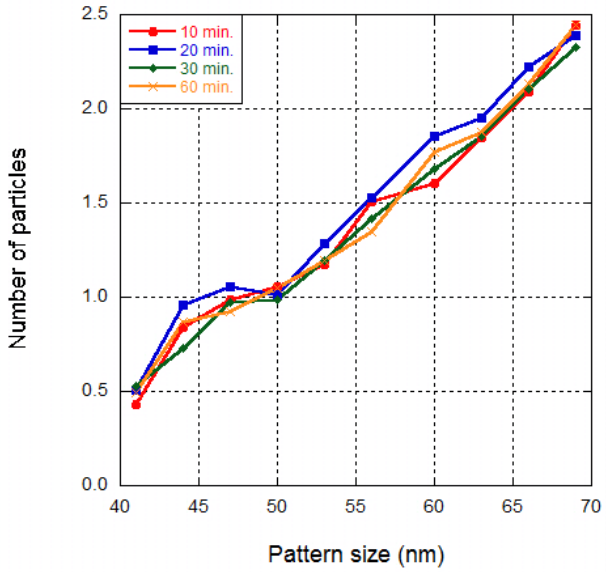

Figure 2.11 Plot of the number of particles that assemble on different size nanodots for different immersion times in the gold nanoparticle solution.

Table 2.1 Data for the number of Au NPs that self-assemble on different sized nanodots at different immersion times

Pattern Size (nm)	10 min.	20 min.	30 min.	60 min.
41	0.43 ± 0.50	0.51 ±0.50	0.53 ±0.50	0.49 ±0.53
44	0.84 ±0.40	0.96 ±0.19	0.73 ±0.45	0.87 ±0.46
47	0.99 ± 0.25	1.06 ±0.33	0.97 ±0.39	0.92 ±0.39
50	1.06 ± 0.37	1.01 ±0.35	0.99 ±0.36	1.05 ±0.34
53	1.17 ± 0.38	1.28 ±0.53	1.20 ±0.43	1.20 ±0.49
56	1.51 ± 0.53	1.53 ±0.56	1.41 ±0.50	1.35 ±0.58
60	1.60 ±0.62	1.86 ±0.60	1.68 ±0.57	1.77 ±0.61
63	1.84 ±0.59	1.95 ±0.56	1.85 ±0.59	1.88 ±0.58
66	2.09 ±0.60	2.22 ±0.60	2.11 ±0.64	2.13 ±0.57
69	2.44 ±0.58	2.39 ±0.59	2.33 ±0.63	2.44 ±0.73

From the data, it appears that longer immersion times are of little consequence. The diffusion constant, *D*, of a Au NP in solution can be calculated using the Stokes-Einstein equation,

$$D = \frac{k_b T}{6\pi\eta r}, \tag{1}$$

where k_b is the Boltzmann constant, T is the temperature of the solution (300°K), η is the viscosity of the solution (1 cP), and r is the radius of the particle. For a 50 nm Au NP, D ~ 878.9 nm^2/s, and the diffusion length, $(Dt)^{3/2}$, of the particle is ~ 34.2 μm^3 after 20 minutes. For a 1 wt% solution of 50 nm Au NPs, there is approximately 1 nanoparticle per 12.6 μm^3. Since the particle can diffuse outside of its "box" in 20 minutes simply through Brownian motion, it is safe to say that after 20 minutes, under the influence of an

attractive electrostatic force, the negatively charged Au NPs should self-assemble in an equilibrium manner after 20 minutes.

2.4.7 Salt Concentration Effects on Self-Assembly

The effect of the salt concentration on the loading density of the Au NPs was also investigated. It was expected that by introducing NaCl, the salt would screen the repulsion between the like-charged Au NPs and a larger number of particles would assemble on the same sized nanodot. Samples were dipped for 20 minutes in 30 nm Au NP solutions with NaCl concentrations of 0, 1, 2, 5, and 10 mM, and withdrawn at 10 um/s. The number of particles that assembled on various sized nanodots is illustrated in Figure 2.12 and summarized in Table 2.2. As the NaCl concentration increases, the number of particles that deposit on the nanopattern increases, as expected due to the charge screening effects of the NaCl. Curiously, the NaCl does not seem to have as great of an effect at screening the positive charge from the aminosilane nanodot, since the self-assembly is still very fast. However, the standard deviations of the data increase as the salt concentration increased, indicating that the presence of NaCl leads to more imprecise patterning.

Since the Au nanoparticles are better screened from one another's charge-charge repulsion, the Au nanoparticles are able to more closely pack on each nanodot. Further evidence of the screening effects of the NaCl is seen in the SEM images of samples from the NaCl study, Figure 2.13. In Figure 2.13 there is some non-specific deposition as a result of the charge screening effects of NaCl. What is interesting is that when NaCl is added to the Au NP solution too soon, the concentration spike of NaCl causes the Au NP

solution to turn from red to purple until additional Au NP solution is added. The change in color suggests that the NaCl is effective enough at screening the particle-particle repulsion to enable aggregation of the Au NPs. This is evident in Figure 2.13b, which shows enhanced non-specific deposition. Conversely, when the NaCl is added when the Au NP solution is nearly at total volume, there was no color change in the solution and very little non-specific deposition (Figure 2.13a). Thus, the order in which the NaCl is added is crucial to the patterning of the Au NPs.

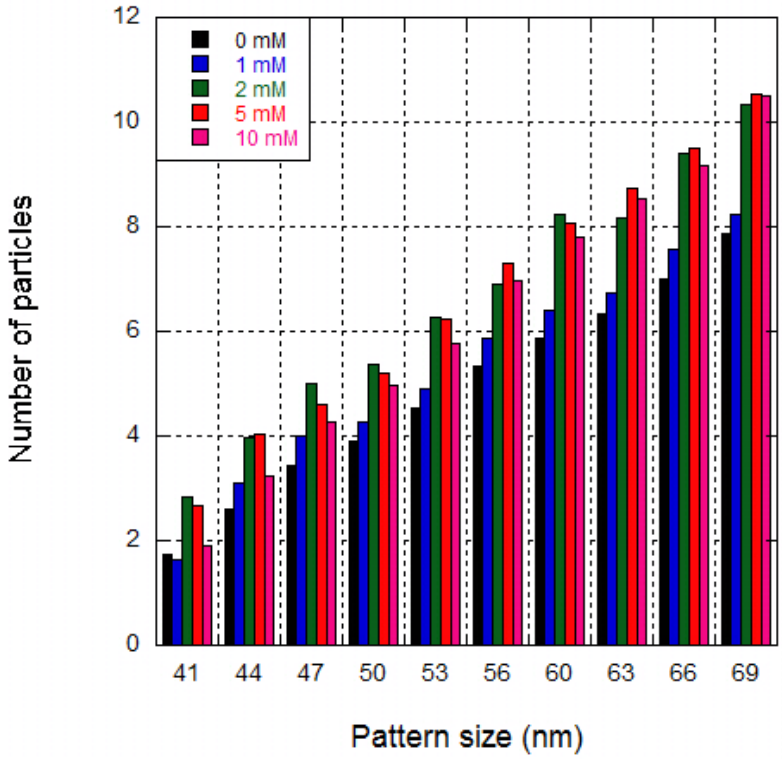

Figure 2.12 Plot of the number of particles that assemble on different sized nanodots for different concentrations of NaCl.

Table 2.2 Data for the number of Au NPs that self assemble on different sized nanodots for different concentrations of NaCl

Pattern Size (nm)	0 mM	1 mM	2 mM	5 mM	10 mM
41	1.72 ± 0.58	1.62 ± 0.56	2.84 ± 0.58	2.66 ± 0.62	1.91 ± 0.62
44	2.60 ± 0.56	3.10 ± 0.55	3.98 ± 0.64	4.03 ± 0.70	3.25 ± 0.79
47	3.43 ± 0.64	4.00 ± 0.68	5.00 ± 0.71	4.59 ± 0.86	4.26 ± 0.71
50	3.91 ± 0.64	4.26 ± 0.81	5.38 ± 0.74	5.20 ± 0.91	4.97 ± 0.92
53	4.53 ± 0.68	4.90 ± 0.89	6.27 ± 0.86	6.24 ± 0.87	5.76 ± 0.83
56	5.32 ± 0.69	5.88 ± 1.10	6.91 ± 0.88	7.30 ± 1.01	6.98 ± 0.86
60	5.86 ± 0.81	6.39 ± 0.81	8.23 ± 1.10	8.08 ± 1.19	7.79 ± 1.12
63	6.33 ± 0.81	6.75 ± 0.97	8.18 ± 1.24	8.74 ± 0.90	8.53 ± 1.20
66	6.99 ± 0.90	7.57 ± 1.06	9.41 ± 1.02	9.49 ± 1.09	9.17 ± 1.21
69	7.87 ± 0.90	8.25 ± 0.83	10.33 ± 1.17	10.55 ± 1.21	10.49 ± 1.23

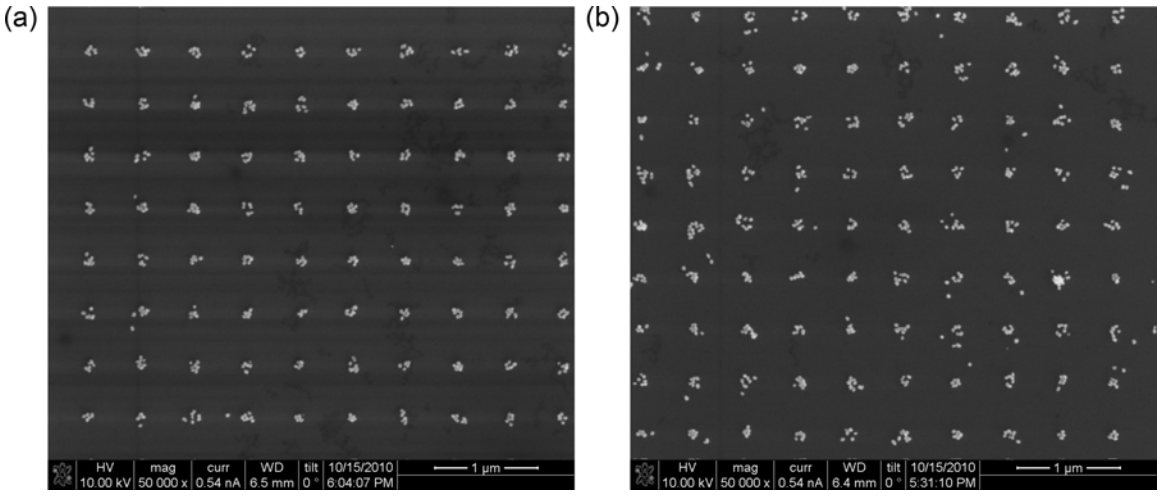

Figure 2.13 Citrate-capped, 37 nm Au NPs patterned on 69 nm aminosilane nanodots from a 1 mM NaCl solution of Au NPs. For (a), the solution was prepared by adding 4 mL of Au NP solution, 50 uL of 0.1 M NaCl, and then 0.95 mL of additional Au NP solution. For (b) the solution was prepared by adding 1 mL of Au NP solution, 50 uL of 0.1 M NaCl, and then 3.95 mL of additional Au NP solution. Adding the NaCl to the solution too soon can result in additional non-specific deposition as seen in (b).

The importance of when the NaCl is added to the Au NP solution was further investigated. A small volume of Au NP solution was added to a UV-Vis cuvette, then 5 µl of 1 M NaCl was added to the cuvette, and finally additional Au NP solution was added to bring the total solution volume to 1 mL. The final NaCl concentration was always 5 mM. Table 2.3 shows the different volumes of Au NP solution that were added and the intermediate NaCl concentration after the NaCl is added to the first volume of Au NP solution. In the case of the 100 µL Au NP solution, the NaCl concentration reaches 43.5 mM. The solution color changed from red to purple to clear after adding the NaCl, indicating Au NP aggregation. This was the only solution that showed any noticeable color change after the addition of NaCl. UV-Vis was used to further probe for any Au NP aggregation. UV-Vis spectra and optical images for all solutions after adding NaCl and in their final state are shown in Figure 2.14. From the UV-Vis spectra, it would appear that there is some aggregation in the other solutions. The amount of aggregation decreases the later the NaCl is added to the solution. All of the final solutions appeared red in color, but the second absorption peak around 800 nm is greatest for the solutions in which the NaCl was added sooner. Thus, even though the solutions are still red, there is still some irreversible aggregation that occurs when the NaCl is added due to the charge screening.

Table 2.3 A list of the solutions for the study of the effect of when the NaCl is added on the aggregation of the Au NPs. The intermediate NaCl concentration is also listed for each solution. The final NaCl concentration for each solution was 5 mM

Initial Au NP volume (µL)	Volume of 1 M NaCl (µL)	Final Au NP volume (µL)	Intermediate NaCl concentration (mM)
100	5	895	47.6
150	5	845	32.3
200	5	795	24.4
300	5	695	16.4
500	5	495	9.9
995	5	0	5.0

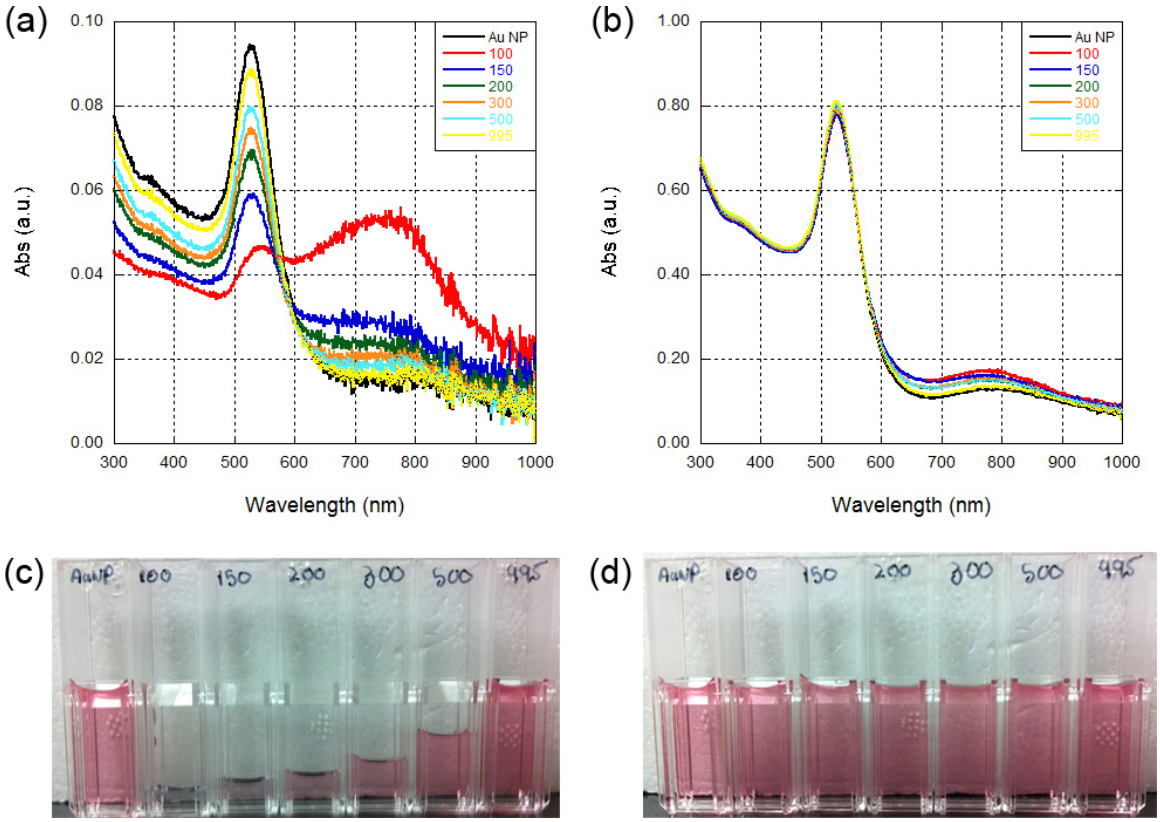

Figure 2.14 UV-Vis spectra of Au NP solutions (a) after adding NaCl to the initial Au NP solution volume and (b) after the final Au NP solution volume is added. Optical images of the Au NP solutions (c) after adding NaCl to the initial Au NP solution volume and (d) after the final Au NP solution volume is added.

The Debye length, κ^{-1}, is the scale over which mobile charge carriers screen out electric fields. The Debye length provided by an ionic salt is given by

$$\kappa^{-1} = (8\pi N_A \lambda_B I)^{-1/2}, \tag{2}$$

where λ_B is the Bjerrum length of the medium (~0.7 nm for water at room temperature), N_A is Avogadro's number, and I is the concentration of the salt in mol/dm^3 (mol/L). The Debye length for NaCl is plotted up to a concentration of 100 mM in Figure 2.15. As the concentration of the NaCl increases, the screening length exponentially decreases. At 50 mM, κ^{-1} = 1.37 nm, so the Au NPs can get fairly close to each other. Based on the intermediate concentrations listed in Table 2.3, it appears that Au NP aggregation

aggressively begins when the Debye length reaches a critical value between 1.71 and 1.41 nm. In other words, once the Au NPs are able to get within ~1.5 nm of each other, the Au NPs are able to aggregate.

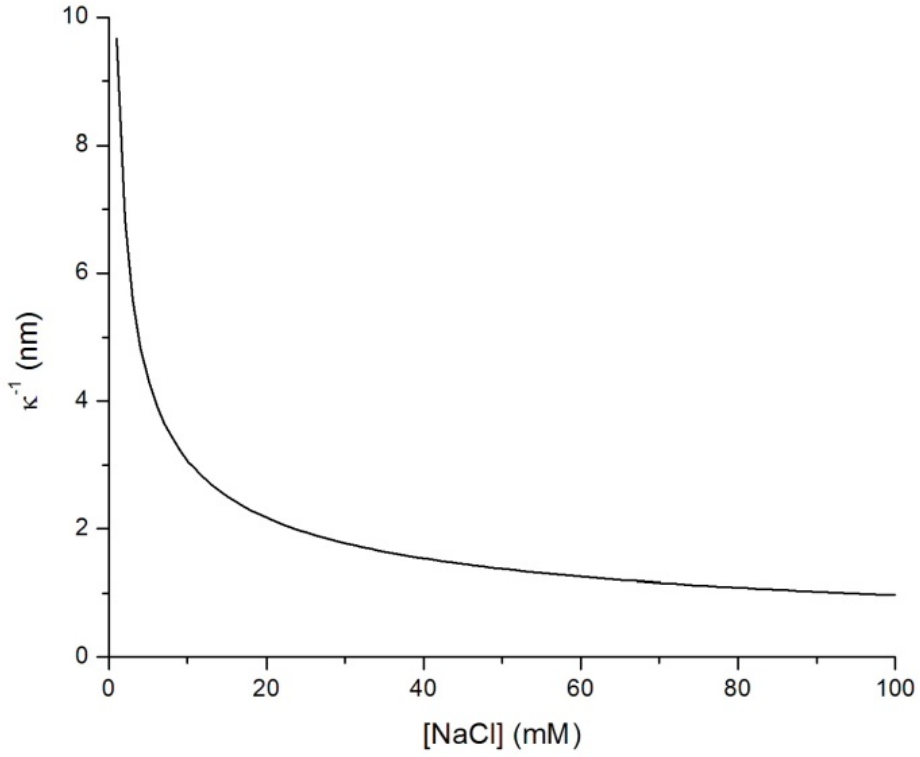

Figure 2.15 A plot of the Debye length, κ^{-1}, as a function of the concentration of NaCl in water.

2.5 Conclusions

In conclusion, we have demonstrated a simple technique to pattern Au NPs using chemically patterned templates. Unlike other systems that use aminosilanes to electrostatically pattern Au NPs, this system does not require an additional functional molecule to prevent non-specific deposition on unpatterned areas. By controlling the relative sizes of the Au NPs and the aminosilane dots, it is possible to control the number

of Au NPs that self-assemble on the aminosilane dot. Also, this system allows very fast assembly of the Au NPs, taking 20 minutes to reach equilibrium. Using NaCl to screen the inter-particle repulsion allowed for greater numbers of particles to assemble on the same sized chemical pattern. However, caution should be used in regard to when the NaCl solution is added to the Au NP solution. If the NaCl is added too soon, the spike in concentration can lead to unwanted aggregation of Au NPs in solution. If the NaCl concentration reaches some value between 32 an 48 mM, massive aggregation of the Au NPs rapidly occurs.

2.6 References

1. Lee, I.; Zheng, H. P.; Rubner, M. F.; Hammond, P. T., Controlled cluster size in patterned particle arrays via directed adsorption on confined surfaces. *Adv. Mater.* **2002,** *14* (8), 572-577.
2. Maury, P.; Peter, M.; Crespo-Biel, O.; Ling, X. Y.; Reinhoudt, D. N.; Huskens, J., Patterning the molecular printboard: patterning cyclodextrin monolayers on silicon oxide using nanoimprint lithography and its application in 3D multilayer nanostructuring. *Nanotechnology* **2007,** *18* (4).
3. Frens, G., CONTROLLED NUCLEATION FOR REGULATION OF PARTICLE-SIZE IN MONODISPERSE GOLD SUSPENSIONS. *Nature-Physical Science* **1973,** *241* (105), 20-22.
4. McCord, M. A.; Rooks, M. J., Electron Beam Lithography. In *SPIE's Handbook of Microlithography, Micromachining, and Microfabrication*, Rai-Choudhury, P., Ed. SPIE: Bellingham, Washington, 1997; Vol. 1, pp 139-250.
5. Farnesi Camellone, M.; Reiner, J. C.; Sennhauser, U.; Schlapbach, L., Formation of electron traps in amorphous silica. *Phys. Rev. B* **2007,** *76* (12), 125205.
6. Zhang, J. F.; Taylor, S.; Eccleston, W., Electron trap generation in thermally grown SiO2 under Fowler-Nordheim stress. *Journal of Applied Physics* **1992,** *71* (2), 725-734.
7. Maury, P.; Escalante, M.; Reinhoudt, D. N.; Huskens, J., Directed assembly of nanoparticles onto polymer-imprinted or chemically patterned templates fabricated by nanoimprint lithography. *Adv. Mater.* **2005,** *17* (22), 2718-+.
8. Huang, H. W.; Bhadrachalam, P.; Ray, V.; Koh, S. J., Single-particle placement via self-limiting electrostatic gating. *Appl. Phys. Lett.* **2008,** *93* (7).
9. Ma, L.-C.; Subramanian, R.; Huang, H.-W.; Ray, V.; Kim, C.-U.; Koh, S. J., Electrostatic Funneling for Precise Nanoparticle Placement: A Route to Wafer-Scale Integration. *Nano Letters* **2007,** *7* (2), 439-445.
10. Li, Q. G.; Zheng, J. W.; Liu, Z. F., Site-selective assemblies of gold nanoparticles on an AFM tip-defined silicon template. *Langmuir* **2003,** *19* (1), 166-171.
11. Zheng, J. W.; Zhu, Z. H.; Chen, H. F.; Liu, Z. F., Nanopatterned assembling of colloidal gold nanoparticles on silicon. *Langmuir* **2000,** *16* (10), 4409-4412.
12. Manandhar, P.; Akhadov, E. A.; Tracy, C.; Picraux, S. T., Integration of Nanowire Devices in Out-of-Plane Geometry. *Nano Letters* **2010,** *10* (6), 2126-2132.
13. Pallandre, A.; Glinel, K.; Jonas, A. M.; Nysten, B., Binary nanopatterned surfaces prepared from silane monolayers. *Nano Letters* **2004,** *4* (2), 365-371.

Chapter 3

Cross-Linking Electrostatically Self-Assembled Gold Nanoparticles

3.1 Introduction

The electrostatic self-assembly of Au NPs described in the chapter 2 was the first step in a grander factory to generate elements for isotropic metamaterials. The next step would be to cross-link the nanoparticles and lift-off or remove them from the chemical template.

The initial choice for cross-linking would be to use a polymer with multiple thiol groups, since thiol groups have a stronger affinity for binding to Au than the citrate molecules. Thus, the citrate molecules would be displaced and the thiol-functional polymer would network the self-assembled Au NPs into one unit. However, there are no commercially available macromolecules having multiple thiols that could be used. Another problem with a molecule possessing so many thiol groups is that the thiol groups would react with each other to form disulfide bonds. This would cross-link the polymers in solution and render them insoluble. Thus, it became necessary to choose a different direction.

Since the self-assembly of the Au NPs is electrostatic, the Au NPs possess a negative charge even after deposition. In the case of layer-by-layer assemblies of polyelectrolytes, oppositely charged polymers are repeatedly deposited on top of each other to form a multi-layer structure.[1-4] Treating the Au NPs as a negatively charged

polymer, it should be possible to assemble a positively charged polymer on top of the Au NPs, which will bind them together.

Poly(diallyldimethylammonium chloride) (PDDA, Figure 3.1) was chosen because of its quaternary ammonium group. The primary amine that was used to direct the self-assembly of the Au NPs on the chemical template is pH sensitive. If the pH becomes too basic, the amine deprotonates from NH_3^+ to NH_2 and becomes neutral in charge. However, quaternary ammoniums are not pH sensitive. Due to the four bonds on the nitrogen, the nitrogen possesses a permanent, positive charge.

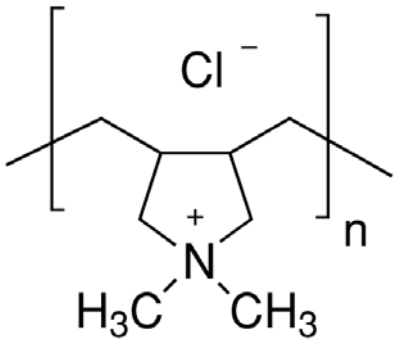

Figure 3.1 The chemical structure for PDDA.

3.2 Experimental

Poly(diallyldimethylammonium chloride) (M_w = 100,000 – 200,000 g/mol, 20 wt. % in water) and all other chemicals were purchased from Sigma Aldrich and used as received.

Citrate-capped Au NPs were self-assembled on APDMES patterned chemical templates as described in Chapter 2. The APDMES patterned sample was dipped into a solution of citrate-capped Au NPs for 20 min. and removed at a rate of 10 μm/s.

3.2.1 PDDA to Cross-link Patterned Au NPs

0.1 and 0.5 mM solutions of PDDA were prepared in D.I. H_2O. 1 mL of the PDDA solution was transferred to a microcentrifugation vial and an already self-assembled Au NP sample was immersed in the solution overnight. Then, samples were dipped in D.I. H_2O before being spray rinsed with 20 mL of D.I. H_2O from a syringe. Some samples were also sonicated in D.I. H_2O for 60 min. After the rinsing, all samples were dipped in Au NP solutions for 20 min. to observe multi-layer patterning of Au NPs.

Samples were visualized with SEM (FEI Nova Nanolab FIB/SEM at 10 keV) after the initial Au NP self-assembly and after the self-assembly of the second layer of Au NPs.

3.2.2 Rinsing Effects on Cross-linking With PDDA

A 0.5 mM solution of PDDA in D.I. H_2O was prepared. An already self-assembled Au NP sample was vertically immersed in the solution for 20 minutes and withdrawn at 10 μm/s. The sample was then either not rinsed, rinsed by spraying 20 mL from a syringe, or stirred in a 40 mL beaker of D.I. H_2O for 10 sec. After rinsing, samples were blown dry with Ar gas. Samples were then vertically immersed in a citrate capped Au NP solution for 20 and then withdrawn at 10 μm/s.

UV-Vis (Cary UV-Vis Bio 50) was used to characterize the Au NP solution after the PDDA coated sample was dipped. SEM was used to visualize the samples after the initial Au NP self-assembly and after re-dipping the PDDA coated samples in Au NP solution.

3.2.3 Lifting-off Cross-linked Au NPs with NaOH

An already self-assembled Au NP sample was cross-linked with PDDA by immersing the sample in a 0.5 mM solution of PDDA for 20 min., removing the sample at 10 μm/s, and then swirling the sample in 40 mL of D.I. H_2O for 10 s. The sample was then dried with Ar gas.

NaOH solutions with concentrations of 1 mM, 10 mM, 100 mM, and 1.0 M were prepared in microcentrifuge tubes. A PDDA cross-linked sample was immersed in each solution for 1 hr. Then, the same samples were reimmersed in the NaOH solution for 10 hrs. The same samples were then immersed in the same solutions and sonicated for 15 min. Finally, the same samples were immersed in the same solutions and sonicated for 60 min. After each immersion in NaOH, the samples were rinsed in 40 mL of D.I. H_2O and blown dry with Ar gas.

The samples were visualized with SEM after the initial patterning and each immersion in the NaOH lift-off solution.

3.2.4 Visualizing Lifted-off, Cross-linked Au NPs

UV-Vis was used to characterize the NaOH solutions that had been used to lift-off the cross-linked Au NPs. The solutions were first centrifuged at 10,000g for 30 min. to concentrate the solutions.

Additional samples of self-assembled Au NPs were prepared for indirect visualization of lifted-off, cross-linked Au NPs. A sample of self-assembled Au NPs was dipped in a 0.5 mM PDDA solution for 20 min., swirled in 40 mL in D.I. H_2O to remove loosely bound PDDA, and sonicated in 1 mL of a 10 mM solution of NaOH in a

microcentrifuge tube for 60 min. to lift-off the cross-linked Au NPs. UV-Vis was used to characterize the lift-off solution. Another sample of self-assembled Au NPs was then immersed into the lift-off solution for 20 min. to self-assemble the cross-linked Au NPs on top of the already self-assembled Au NPs. SEM was used to image the self-assembled Au NP sample before and after immersion in the lift-off solution.

3.2.5 Effects of NaOH on the Surface Chemistry of the Chemical Template

A self-assembled Au NP sample was then dipped in a 0.5 mM solution of PDDA for 20 min. and removed at a rate of 10 μm/s. After gently rinsing in a beaker of D.I. H_2O, the sample was immersed in 1 mL a 10 mM solution of NaOH inside a microcentrifuge vial and sonicated for 1 hr. The sample was removed, rinsed with D.I. H_2O, and blown dry with Ar gas. The sample was then reimmersed into a Au NP solution for 20 min. and withdrawn at 10 μm/s. SEM was performed after the initial Au NP assembly, the lift-off, and the second Au NP assembly.

Pieces of a Si wafer (n-type/phosphorus <100>, Silicon Valley Microelectronics) with a 45 nm thick, thermally grown oxide layer were cleaned by sequentially sonicating for 30 min. in a solution of IPA and acetone (1:1, v:v), drying under Ar gas, sonicating for 15 min. in HNO_3, rinsing in D.I. H_2O, and drying under Ar gas. Oxygen plasma was then used to clean any trace organics from the samples. The pieces of Si wafer were then placed overnight in a desiccator under vacuum with 100 μL of 3-aminopropyldimethylethoxysilane (APDMES) to coat the Si pieces with APDMES. Next, the Si pieces were rinsed with MeOH and D.I. H_2O, sequentially, before being placed on a 50°C hotplate for 3 hrs. The Si pieces were then immersed in an aqueous 10 mM NaOH

solution and sonicated for 1 hr. After the sonication, the samples were rinsed with D.I. H_2O and blown dry with Ar gas.

The samples were probed by measuring the contact angle of a water droplet with the Si surface after cleaning, after APDMES deposition, and after the NaOH sonication. X-ray photoelectron spectroscopy (XPS, Kratos Axis Ultra XPS) was also used to characterize the Si surface chemistry after cleaning, after APDMES deposition, and after the NaOH sonication.

3.3 Results and Discussion

3.3.1 Cross-linking Patterned Au NPs with PDDA

To test that the PDDA was effectively cross-linking the Au NPs, samples that had been cross-linked with PDDA were reimmersed in the Au NP solution. If the PDDA had truly cross-linked the Au NPs, then additional Au NPs would self-assemble on top of the original Au NPs, in the style of layer-by-layer polyelectrolytes.

Previously self-assembled Au NP samples were immersed into solutions of PDDA for 1 hr. The PDDA was diluted from its native solution (20 wt% or ~1.67 mM) because of the high viscosity of the native solution. Samples were dipped in D.I. H_2O and then sprayed with 20 mL of D.I. H_2O from a syringe to remove any non-specifically bound PDDA from the sample. Some samples were then sonicated in D.I. H_2O for 60 min. in an attempt to remove the cross-linked Au NPs from the chemical template. The samples were then immersed in the citrate capped Au NP solution again to form a second layer of Au NPs.

SEM images of the four samples before and after the second immersion in the Au NP solution are shown in Figures 3.2-5. It was possible to re-image the same area on separate occasions due to burn-in from the SEM. As can be seen in Figure 3.3a and c and Figure 3.5a and c, sonicating the samples in D.I. H_2O did not do anything to liberate the Au NPs from the chemical template.

Comparing Figures3.2-5a and c to Figures 3.2-5b and d, respectively, it can be seen that additional Au NP patterning is observed after depositing PDDA. However, in the cases of the sonicated samples, Figures 3.3b and d and Figures 3.5b and d, the additional Au NP patterning occurs all over the sample. In the case of the array of aminosilane dots, it makes sense for there to be additional patterning off of the previously patterned Au NPs.

The molecular weight of the PDDA used is 100,000 to 200,000 g/mol, which corresponds to 614 to 1229 repeat units of PDDA. Assuming that the C-C bond length is 0.154 nm and that there are four C-C bonds per repeat unit, the extended length of the PDDA would be between 757 and 379 nm. In the case of the array of aminosilane dots, there is a 500 nm spacing between the dots. Since the shortest length of the PDDA covers half of this distance, there is the possibility that the PDDA binds partially to the self-assembled Au NPs and the tail of the polymer extends off to the blank Si wafer. Thus, additional Au NPs may pattern on this PDDA tail that is not on the self-assembled Au NPs.

However, in the case of the large alignment mark which is 5 μm wide, the tails of the PDDA should not extend to cover all of the blank Si seen in the four corners of Figures 3.2-5a and c. While this holds true for the non-sonicated samples as seen in

Figures 3.2c and 3.4c, there is Au NP deposition everywhere on the sonicated samples as seen in Figures 3.3c and 3.5c. Thus, it would appear that the sonication causes the PDDA, which is otherwise relatively confined to the previously self-assembled Au NPs, to spread all over the sample and results in Au NP deposition everywhere. Thus, sonication should not be used to remove unbound PDDA.

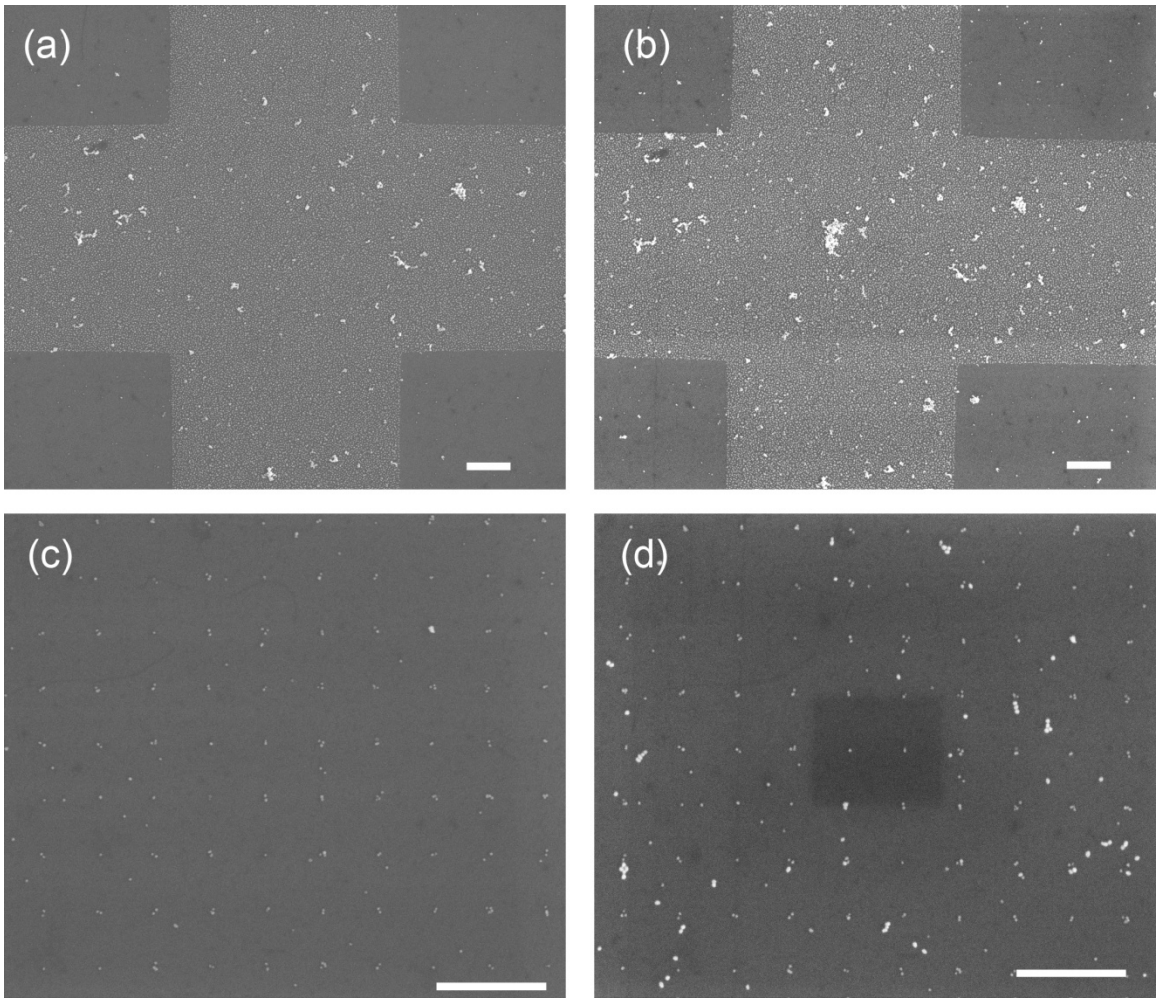

Figure 3.2 SEM images of an already self-assembled Au NP sample (a) and (c) after coating with 0.5 mM PDDA and rinsing with water and (b) and (d) after dipping in Au NPs to self-assemble a second layer of Au NPs. Images (a) and (b) are of a large alignment mark and (c) and (d) are of the array of APDMES dots. Scale bars are 1 μm.

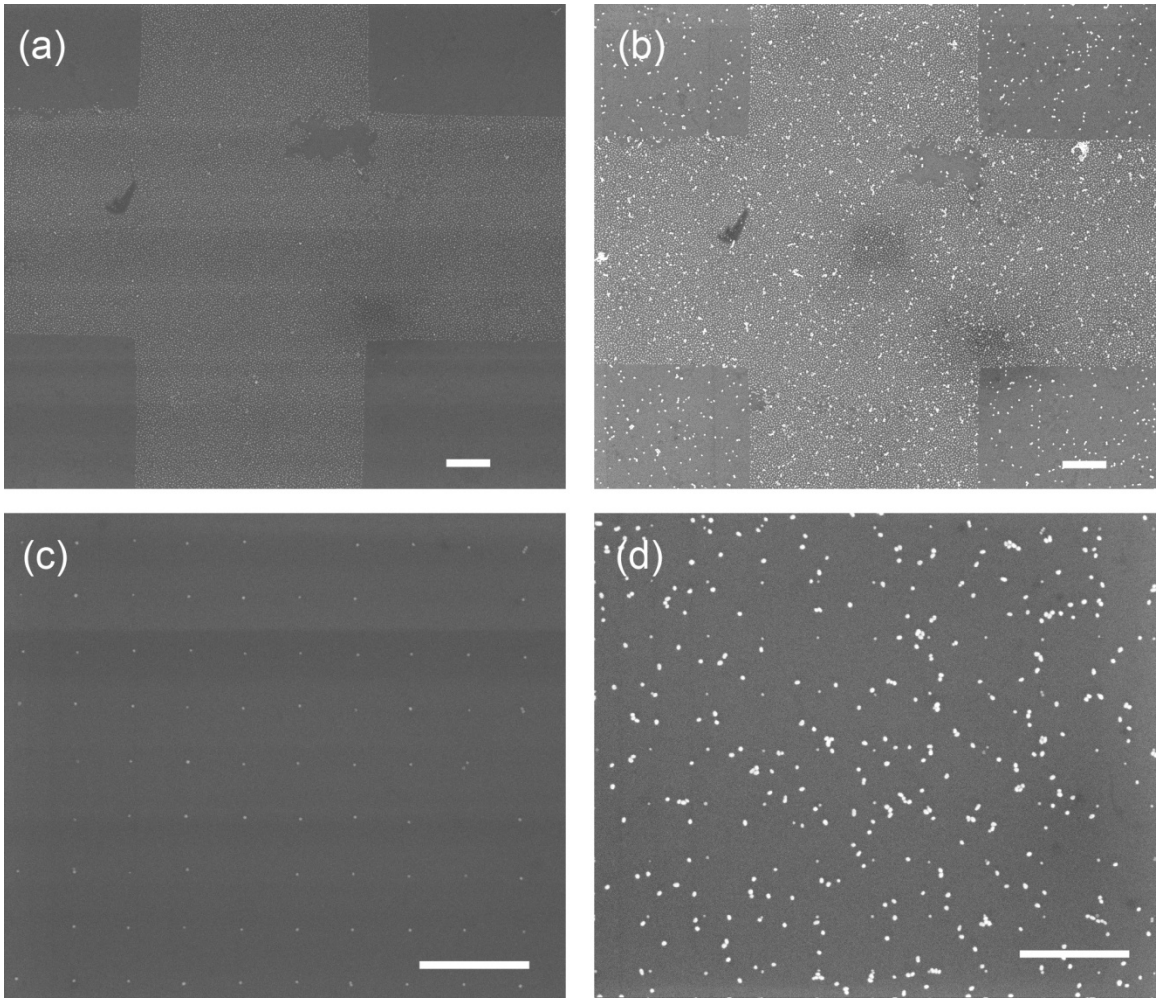

Figure 3.3 SEM images of an already self-assembled Au NP sample (a) and (c) after coating with 0.5 mM PDDA, rinsing with water, and sonicating in water and (b) and (d) after dipping in Au NPs to self-assemble a second layer of Au NPs. Images (a) and (b) are of a large alignment mark and (c) and (d) are of the array of aminosilane dots. Scale bars are 1 μm.

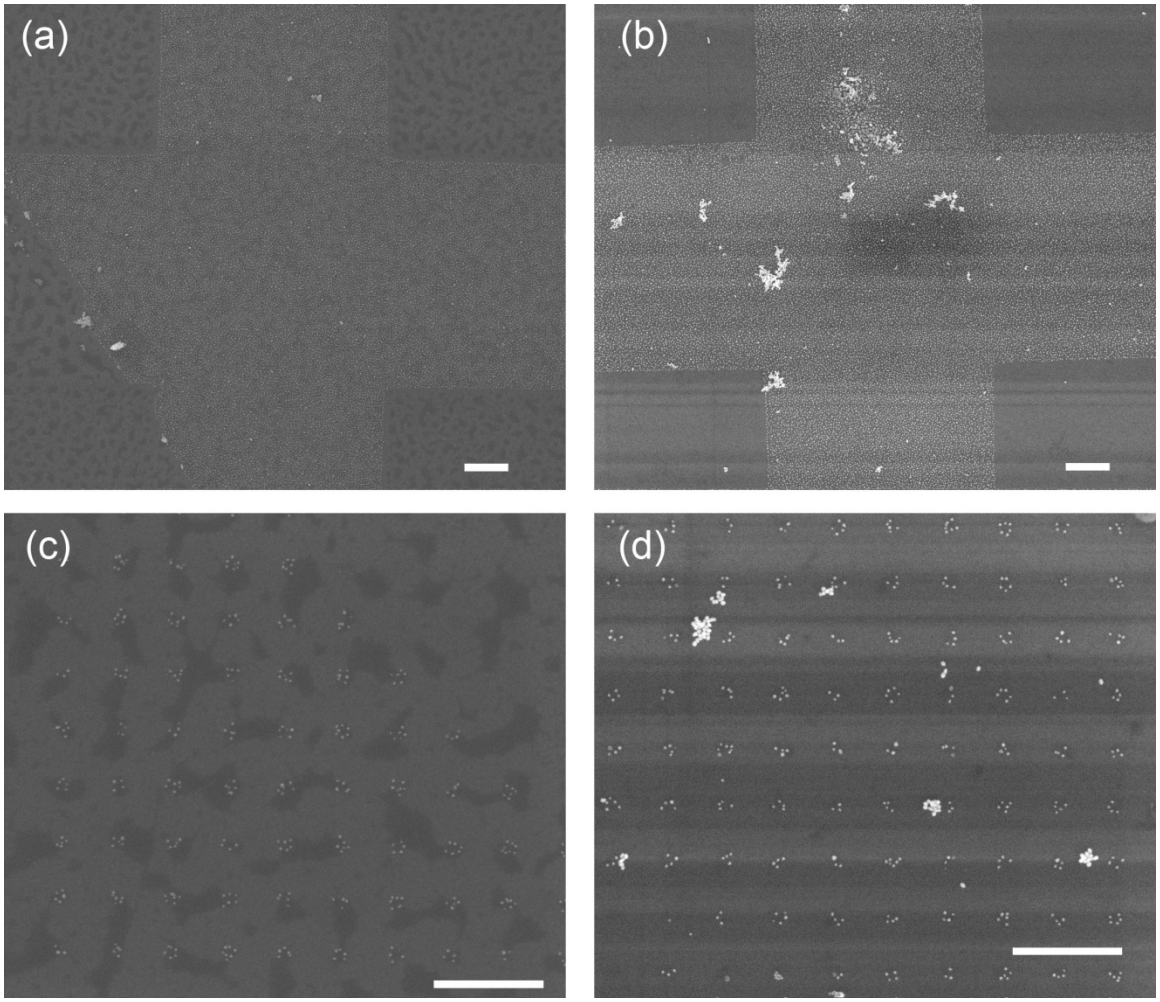

Figure 3.4 SEM images of an already self-assembled Au NP sample (a) and (c) after coating with 0.5 mM PDDA and rinsing with water and (b) and (d) after dipping in Au NPs to self-assemble a second layer of Au NPs. Images (a) and (b) are of a large alignment mark and (c) and (d) are of the array of aminosilane dots. Scale bars are 1 μm.

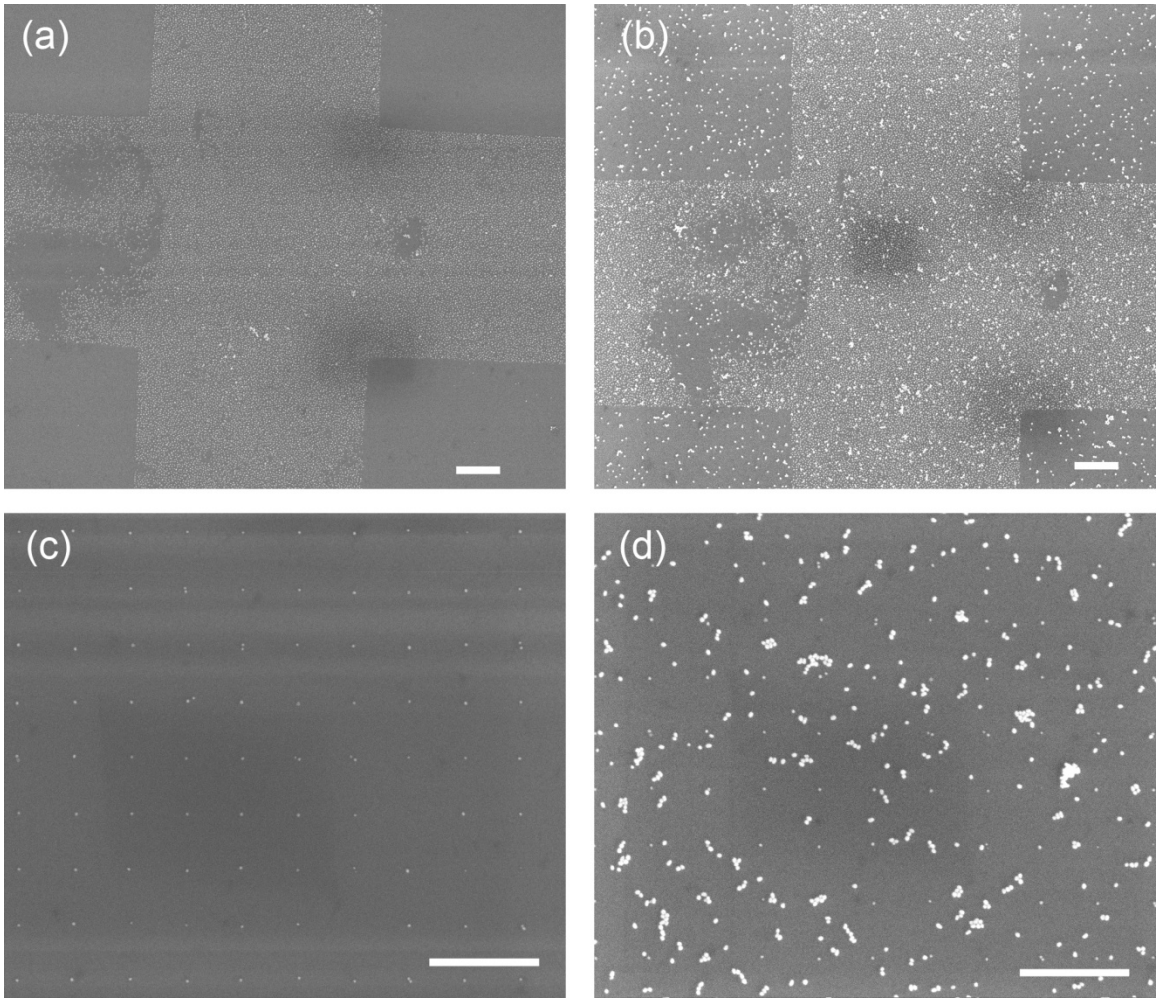

Figure 3.5 SEM images of an already self-assembled Au NP sample (a) and (c) after coating with 0.1 mM PDDA, rinsing with water, and sonicating in water and (b) and (d) after dipping in Au NPs to self-assemble a second layer of Au NPs. Images (a) and (b) are of a large alignment mark and (c) and (d) are of the array of aminosilane dots. Scale bars are 1 μm.

3.3.2 Rinsing Effects on Cross-linking With PDDA

The effects of rinsing the samples after cross-linking with PDDA were also investigated to determine if rinsing was necessary and what type of rinsing would work best. Samples with self-assembled Au NPs were dipped in 0.5 mM PDDA for 20 min. After removing the samples, either no rinsing, rinsing with 20 mL of D.I. H_2O from a syringe, or rinsing by gently stirring the sample in a beaker of D.I. H_2O for 10 sec. was

performed. The samples were then dipped into a solution of citrate-capped Au NPs for 20 min. to allow for multi-layer patterning.

After the sample that was not rinsed was dipped into the Au NP solution, the solution was observed to have changed colors from red to purple, indicating aggregation of the Au NPs. This color change was not observed for the samples that had been rinsed. UV-Vis (Figure 3.6) showed that the Au NP solution from the not rinsed sample had indeed aggregated, while the Au NP solution from the rinsed samples had not aggregated. The UV-Vis for the syringe rinsed sample was not included due to contamination of the Au NP solution with the not rinsed Au NP solution.

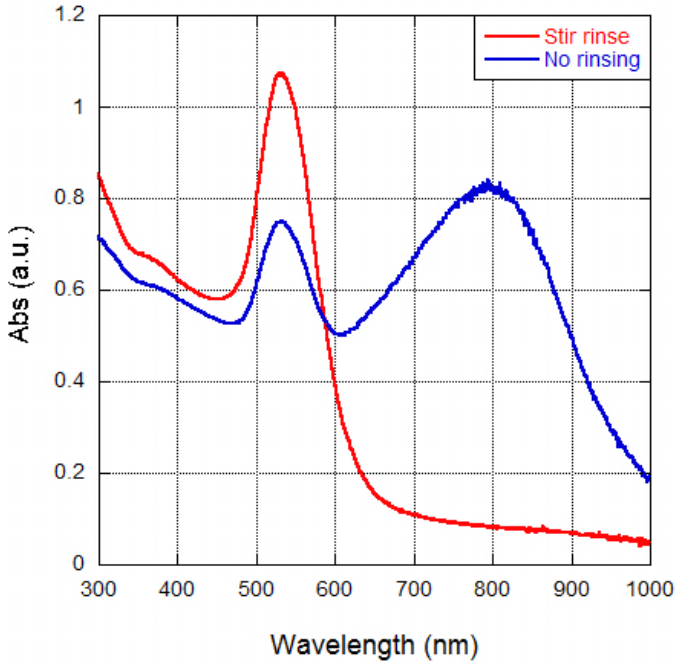

Figure 3.6 UV-Vis of the Au NP solutions from the (blue) not rinsed sample and the (red) stirring rinsed sample after the multi-layer self-assembly on the PDDA cross-linked samples. The absorption peak at 800 nm for the not rinsed sample signifies aggregation of the Au NPs.

SEM images of the not rinsed, syringe rinsed, and stirring rinsed samples after the initial Au NP self-assembly are seen in Figures 3.7a, c, and e, respectively. Images of the

not rinsed, syringe rinsed, and stirring rinsed samples after being cross-linked with PDDA and re-dipped in a Au NP solution for multi-layer self-assembly are seen in Figures 3.7b, d, and f, respectively. Additional Au NP deposition is evident in the rinsed samples, but no additional Au NP deposition is present in the not rinsed sample, Figure 3.7b. Based on the lack of multi-layer self-assembly, the observed color change, and the UV-Vis of the Au NP solution, it appears that all of the PDDA came off of the not rinsed solution in the Au NP solution during what was supposed to be the multi-layer self-assembly.

The rinsed samples both show some degree of additional patterning of Au NPs. This indicates that rinsing is necessary to remove any excess or loosely bound PDDA that is attached to the surface. However, the rinsing does not totally remove all of the PDDA, as evidenced by the additional Au NP patterning in Figures 3.7d and f.

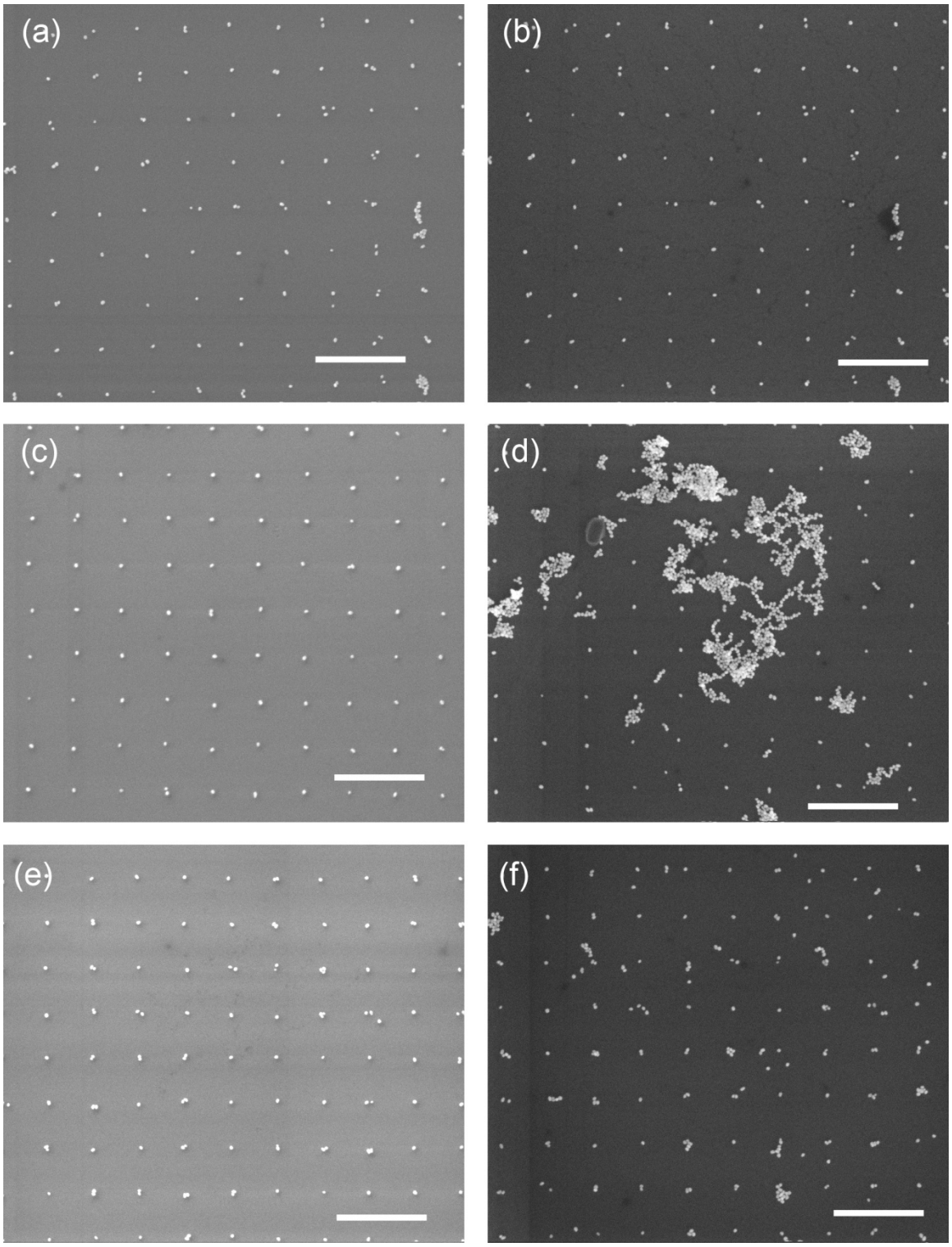

Figure 3.7 SEM images of self-assembled Au NPs (a), (c), and (e) before and (b), (d), and (f) after PDDA deposition and multi-layer Au NP assembly. Samples were either (b) not rinsed, (d) rinsed with 20 mL of D.I. H_2O from a syringe, or (f) rinsed by gently stirring in a beaker of D.I. H_2O before the multi-layer Au NP assembly. The same areas were imaged in the before and after images for each sample. Scale bars are 1 μm.

3.3.3 Lifting-off Cross-linked Au NPs with NaOH

Since the end goal is to use the cross-linked Au NPs as building blocks for optical metamaterials, it is necessary to lift-off the cross-linked Au NPs from the chemical template. It was previously shown in Section 2.4.5 that the self-assembly of the citrate-capped Au NPs on the aminosilane is pH sensitive. Thus, by altering the local pH to basic conditions, it is expected that the Au NPs will be liberated from the chemical template because the electrostatic attraction will no longer hold them there.

Solutions of NaOH with concentrations of 1 mM, 10 mM, 100 mM, and 1 M were prepared in order to optimize the lift-off conditions. The calculated pH's of these solutions are pH = 11, 12, 13, and 14, respectively. Thus, in every solution, the primary amine of the APDMES should be deprotonated and lift-off should occur. Initially, cross-linked, self-assembled Au NP samples were immersed in a NaOH solution for 1 hr. and then for 10 hrs. The samples were then sonicated in a NaOH solution for 15 min., which was followed by 60 min. of additional sonication if lift-off was not observed. The same sample was repeatedly exposed to the same NaOH solution under different conditions to consistently track the effects of the NaOH on the lift-off.

Figures 3.8, 9, 10, and 11 show SEM images for a sample of cross-linked, self-assembled Au NPs as prepared, and after various exposures to a 1 mM, 10 mM, 100 mM, and 1 M solution of NaOH, respectively. Figure 3.8 shows that for 1 mM NaOH, no lift-off occurs until the sample is sonicated for 60 min. Even then the lift-off is minimal, as only a few of the Au NPs self-assembled on the aminosilane dots actually lifted-off of the sample. This could be because the pH of this NaOH solution is fairly close to the pKa of the amine on the APDMES, so the amine is not totally deprotontaed.

For the 10 mM sample, as seen in Figure 3.9, there is only minimal lift-off after 15 min. of sonication. The sample was sonicated for 60 min., but there were no visible features of the self-assembly after the sonication. Burn-in from the previous SEM imaging was present, (Figure 3.12a) which served as a marker for where the previously self-assembled Au NPs used to be. Upon zooming in, there were no distinguishing features (Figure 3.12b). Due to the absence of any Au NPs on the sample, it would appear that lift-off was successful.

In the case of the 100 mM NaOH sample, no lift-off is observed except for after 15 min. of sonication. In that case, there are some peculiar effects. In the case of the alignment mark, the areas of the alignment mark that were not previously imaged had their Au NPs lift off. However, the area of the alignment mark that had been previously imaged still had the self-assembled Au NPs present. The reason for this specific area not lifting-off could be that the SEM imaging causes carbon deposition, which may have formed a thin layer on top of the patterned area which deterred lift-off. In the case of the aminosilane dots, some of the Au NPs had lifted-off, while others did not. Sonication for 60 min. was not explored.

Lastly, for the 1 M NaOH sample, there appears to be some sort of delamination occurring after 10 hrs. of immersion on the area of the aminosilane dots that had been previously imaged via SEM. Also, the alignment mark does not appear to be as sharp as it was previously. After sonication for 15 min., the area that appeared to be delaminating has completely peeled off. The outline of the delamination is seen in Figure 3.11 as is the burn-in on the Si substrate from the SEM imaging. The delamination is probably a result of the aforementioned carbon film that was deposited during SEM imaging. It is also

worth noting that all of the Au NPs have lifted-off. The alignment mark is not shown after 15 min. of sonication because it was no longer visible.

It should be noted that simply immersing the cross-linked Au NP sample into the NaOH solutions did not lift-off the Au NPs. Only in the case of the 1 M NaOH solution is there any change in the self-assembled Au NPs after 10 hrs. of immersion in the NaOH. This solution has the highest pH, and therefore should work the best at deprotonating the APDMES and enabling lift-off. However, none of the solutions show much lift-off until sonication is used. So, why is sonication necessary to liberate the Au NPs from the APDMES?

A previous study suggested that the protonated amine draws in the citrate capped Au NP and then a permanent bond forms.[5] Since the conditions for the formation of an amide bond to form are not present in this system[6, 7], one possibility is that the NH_3^+ of the APDMES replaces the citrate ion and electrostatically binds the Au NP core to the substrate when it self-assembles. Some Au NP synthesis protocols use a ligands with a quaternary ammonium ion to stabilize the Au NPs[8] or a primary amine to stabilize the Au NPs[9]. Also, in the case of Au NR synthesis using citrate-capped Au NP seeds, the citrate is displaced by the ammonium groups of the CTAB molecule during the rod growth.[10, 11] Thus, there is precedent for a positively charged nitrogen group to displace the citrate ion at the Au NP surface. Following this reasoning, the PDDA may also replace the citrate ions on the Au NP surface due to its ammonium group. However, it is expected that the NH_3^+ would only hold the Au NPs at the surface while the amine is protonated, and should not bind the Au NP under basic, deprotonated conditions.

Another possible reason that sonication is needed to lift-off the Au NPs is that the van der Waals forces between the surface and the Au NPs are causing the Au NPs to remain at the surface. Previous work on the electrostatic self-assembly of Au NPs showed that van der Waals forces dominate as a citrate-capped Au NP comes within 10 nm of an APTES patterned SiO_2 surface.[12] The van der Waals interaction energy, *W(z)*, is given by

$$W(z) = -A * a/6z, \quad (1)$$

where *A* is the Hamaker constant for the system of SiO_2/APTES/water/Au (5.7×10^{-20} J, or 0.36 eV), *a* is the diameter of the Au NP (20 nm), and *z* is the distance between the Au NP and the substrate.[12] While the Hamaker constant assumes that APTES is being used, the system being investigated uses APDMES. However, since the two aminosilanes are very similar, the Hamaker constant for the APTES system should provide a close approximation for the APDMES system.

For a Au NP that is 1 nm away from the substrate surface, *W(z)* is calculated to be -1.19 eV. This value is nearly two orders of magnitude greater than the thermal kinetic energy ($1.5k_bT$ = 38.7 eV) of the Au NP at 300°K. Since it is expected that the actual distance between the Au NP and the substrate is smaller than 1 nm, the actual *W(z)* is less than -1.19 eV and still a few orders of magnitude larger than the thermal kinetic energy. Thus, the van der Waals forces are more than adequate at keeping the Au NPs bound to the substrate in the absence of the electrostatic attraction and sonication is necessary to overcome the van der Waals forces and liberate the Au NPs from the substrate.

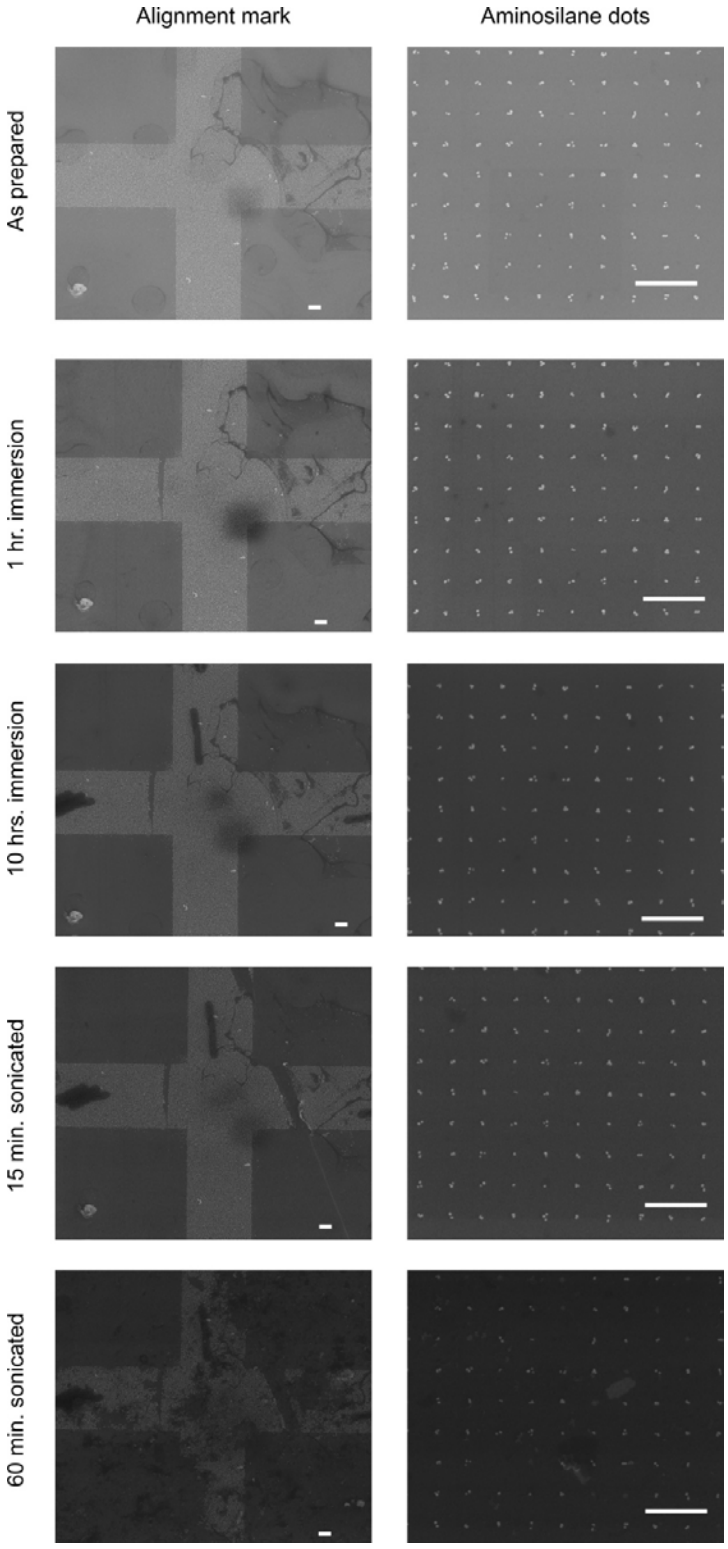

Figure 3.8 SEM images of a sample of self-assembled Au NPs that were cross-linked with PDDA and exposed to a 1 mM NaOH solution for various times and conditions in order to lift-off the cross-linked Au NPs. Scale bars are 1 μm.

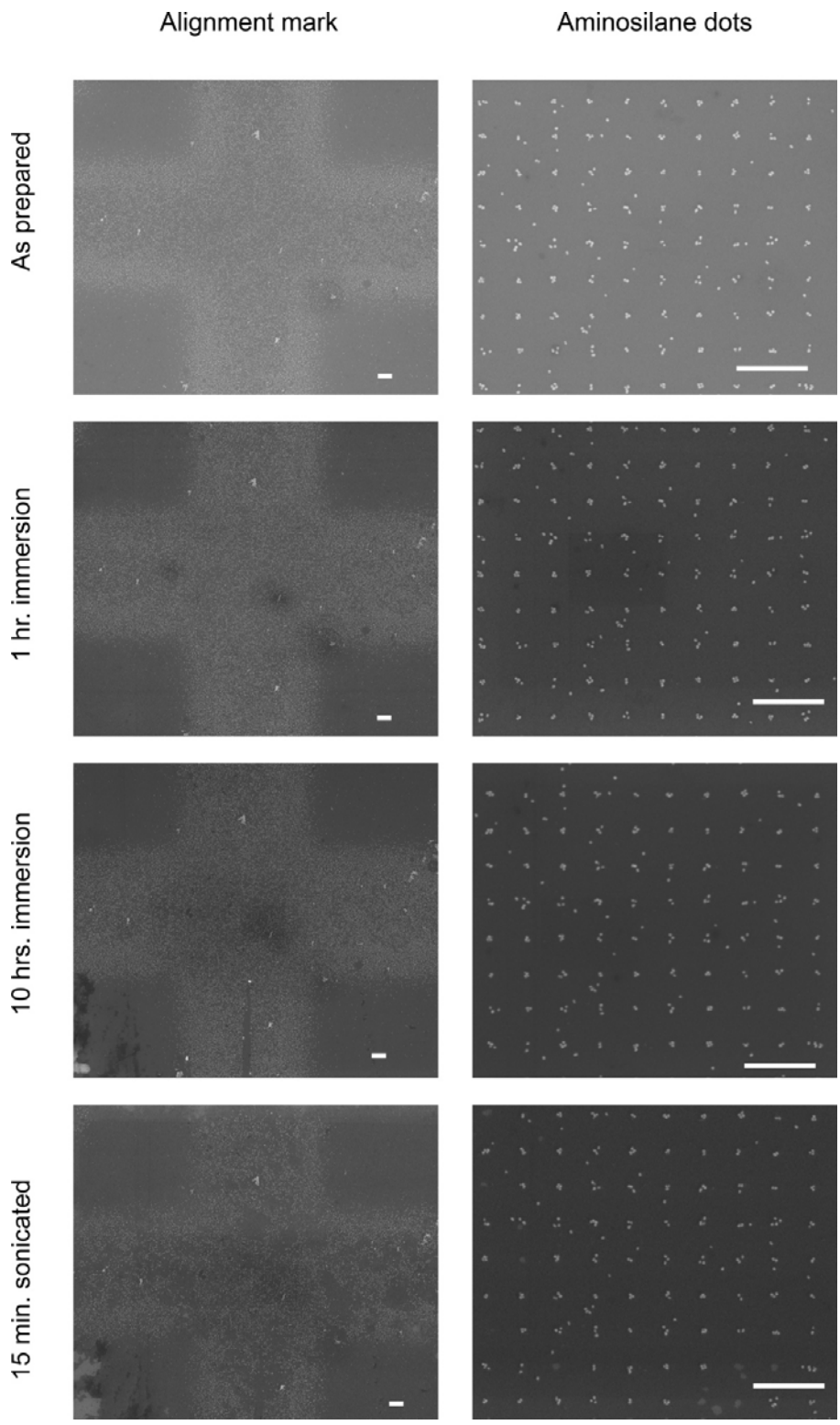

Figure 3.9 SEM images of a sample of self-assembled Au NPs that were cross-linked with PDDA and exposed to a 10 mM NaOH solution for various times and conditions in order to lift-off the cross-linked Au NPs. Scale bars are 1 um.

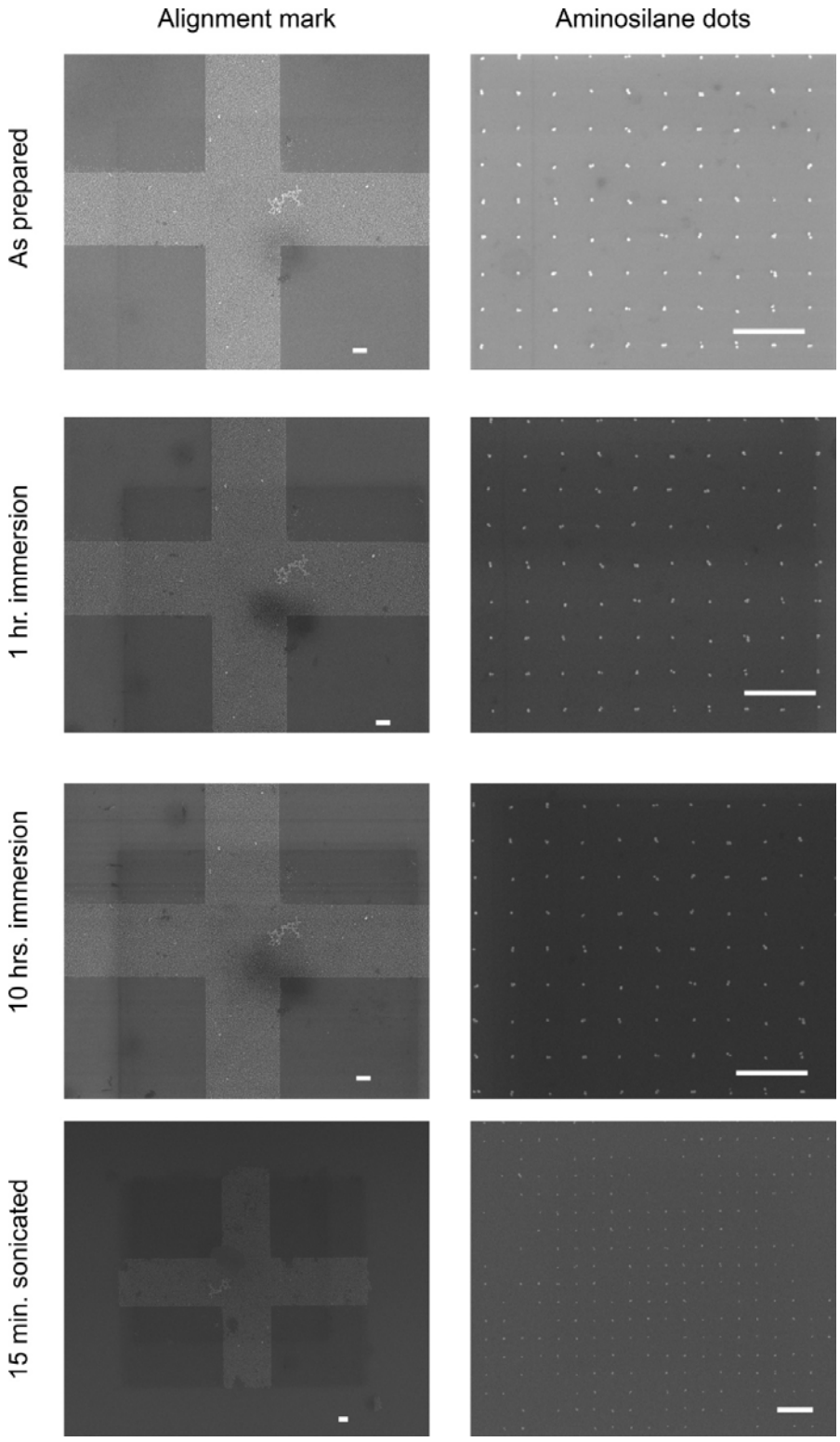

Figure 3.10 SEM images of a sample of self-assembled Au NPs that were cross-linked with PDDA and exposed to a 100 mM NaOH solution for various times and conditions in order to lift-off the cross-linked Au NPs. Scale bars are 1 um.

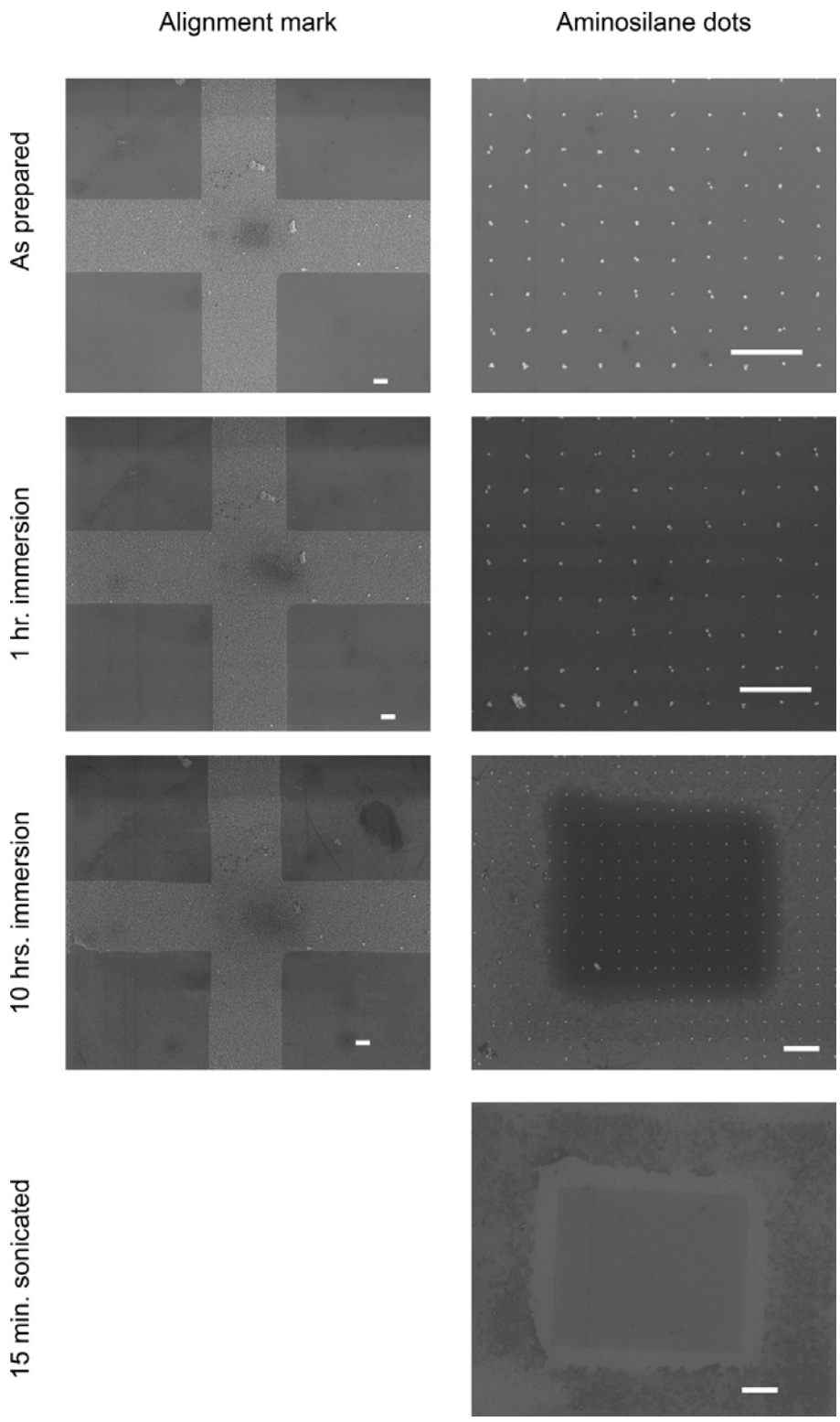

Figure 3.11 SEM images of a sample of self-assembled Au NPs that were cross-linked with PDDA and exposed to a 1 M NaOH solution for various times and conditions in order to lift-off the cross-linked Au NPs. Scale bars are 1 um. The alignment mark was not imaged after 15 min. of sonication because it was not visible.

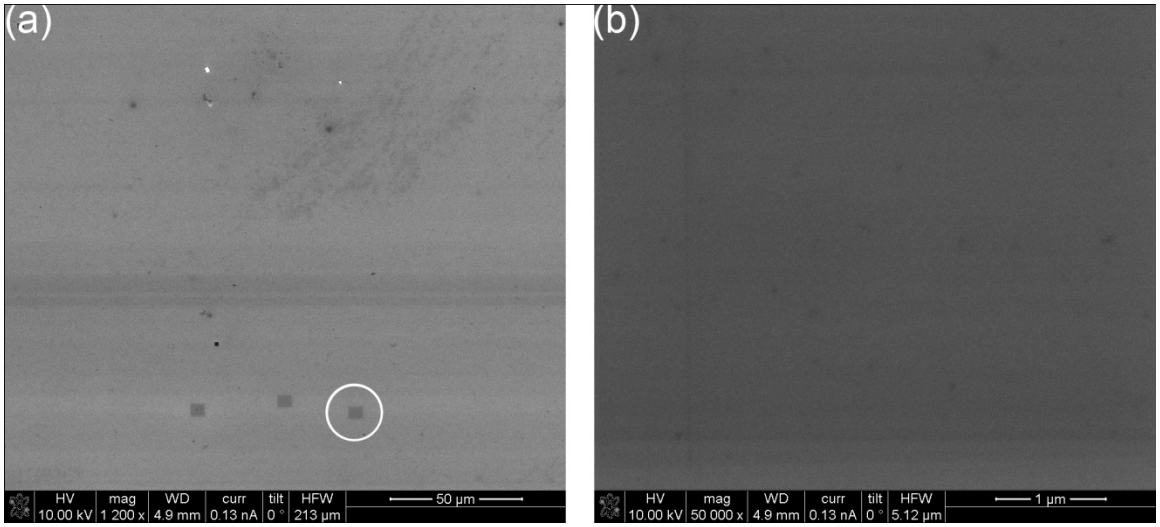

Figure 3.12 SEM images of the cross-linked, self-assembled Au NP sample after sonicating in 10 mM NaOH for 60 min. (a) A zoomed out view of the sample showing three burned-in areas from previously imaged aminosilane dot arrays. (b) A zoomed in view of the circled burn-in area in (a). The absence of Au NPs indicates that the sonication was successful at lifting-off the Au NPs.

3.3.4 Visualizing the Lifted-off, Cross-linked Au NPs

After lifting-off the Au NPs with sonication in NaOH solutions, the solutions were centrifuged to concentrate the lifted-off, cross-linked Au NPs. However, no precipitate was seen in the centrifuged samples except in the case of the 1 M NaOH solution. The precipitate was whitish in color, which does not correspond to the color of Au NP solutions. The UV-Vis absorption of the 10 mM, 100 mM, and 1 M NaOH solutions are seen in Figure 3.13 as well as the absorption plot for an Au NP solution as a reference. As seen in the UV-Vis plot, there is no absorption from the NaOH solutions. This could mean that either there are no Au NPs present in the lift-off solutions, or the concentration of the Au NPs in the lift-off solutions is too low to be detected by the UV-Vis. Since the SEM images show that the Au NPs are no longer on the sample, the most

likely situation is that the Au NPs are in the lift-off solutions, but at concentrations too low to be detected.

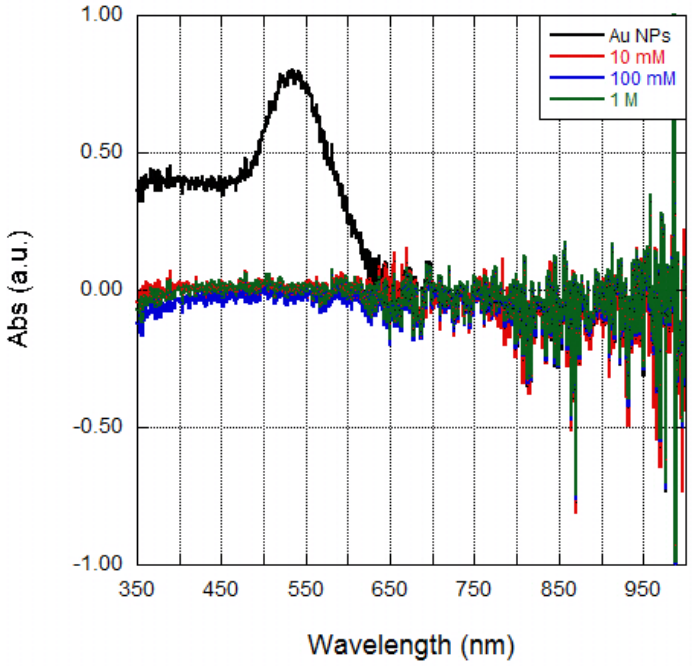

Figure 3.13 UV-Vis absorption of the NaOH lift-off solutions after lifting-off the PDDA cross-linked Au NPs. The Au NP curve is included for reference.

In order to determine the threshold for the number of Au NPs that must be present in solution to be detected by the UV-Vis, a small volume of Au NP solution was added to D.I. H_2O and UV-Vis was used to characterize the sample. The UV-Vis spectra for 1 mL solutions containing different quantities of Au NPs is shown in Figure 3.14. For 10^7 Au NPs, there appears to be some surface plasmon absorption detected, but it is difficult to discern from the noise of the signal. Only if there are above ~10^8 Au NPs per 1 mL of solution can the UV-Vis clearly discern the presence of the Au NPs. Presuming that there are four Au NPs per aminosilane dot, and there are 10 arrays of 20 by 20 dots and that the Au NPs pack such that there is one Au NP per 0.05 µm diameter circle on the alignment mark which is a 50 µm across and 5 µm wide cross, there are 257,916 self-assembled Au

NPs per sample. This is nearly two orders of magnitude lower than what the UV-Vis can safely detect. Thus, UV-Vis should not be relied upon to detect the lifted-off Au NPs.

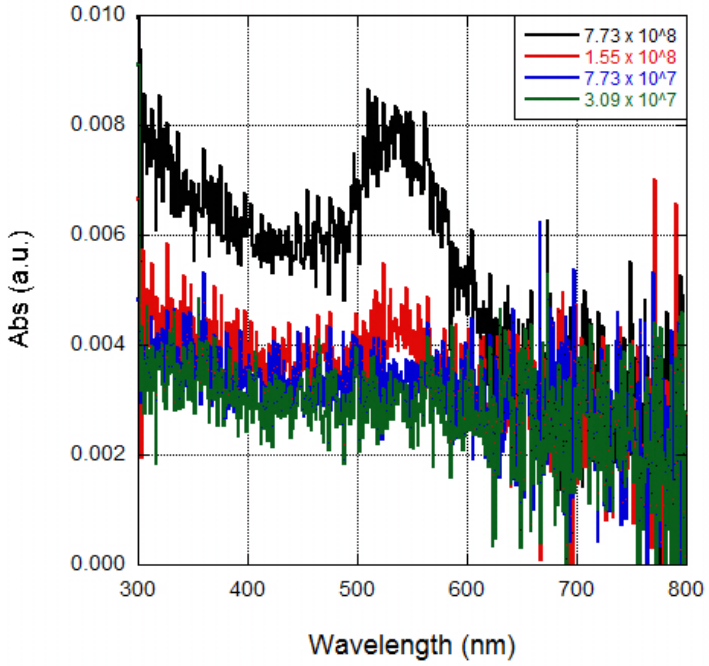

Figure 3.14 UV-Vis of Au NP solutions containing different quantities of Au NPs, as listed in the legend.

To indirectly visualize the lifted-off, cross-linked Au NPs, a self-assembled Au NP sample was cross-linked with PDDA, then lifted off in 10 mM NaOH. Another self-assembled Au NP sample was immersed into the lift-off solution in order to direct the self-assembly of the lifted-off, cross-linked Au NPs onto the self-assembled Au NPs. Since the cross-linked Au NPs are cross-linked by PDDA, the PDDA should be able to electrostatically bind to the self-assembled Au NPs on the immersed sample, which would effectively self-assemble the cross-linked Au NPs on the self-assembled Au NPs on the sample. This multi-layer assembly would enable indirect observation of the cross-linked Au NPs.

Figure 3.15a shows the UV-Vis of the lift-off solution used to collect the cross-linked Au NPs. The lift-off solution did show a white precipitate, which could be some sort of carbon or polymer that causes the absorption around 300 nm. The UV-Vis shows no absorption peak around 525 nm, so no Au NPs were detected. But, as mentioned above, the number of particles expected in solution is too low to be detected via UV-Vis.

Figures 3.15b and c show the alignment mark on a sample of self-assembled Au NPs before and after immersion in the NaOH lift-off solution. The black areas deposited on the alignment mark in Figure 3.15c were not deposited anywhere else on the sample, not even on the aminosilane dot areas. In fact, no additional patterning was observed on the self-assembled Au NPs on the aminosilane dots.

Figure 3.15d is a zoomed in image of one of the black areas seen in Figure 3.15c. The darkened area appears to be transparent and there do not seem to be any additional Au NPs on this area. The aggregate to the right of the darkened area is somewhat translucent, but also does not contain any additional Au NPs.

Since no additional Au NPs were patterned, but this black film appears to have been patterned, the question arises: what is the black film? Based on the study for lifting-off with NaOH in Section 3.3.3, the black film could be carbon film that had been deposited during SEM imaging and removed from the surface during the lift-off. The black areas are visually similar to those seen in the 10 hr. immersion image of the aminosilane dots in Figure 3.11, but it is impossible to say what the black areas are for sure.

Interestingly, no cross-linked Au NPs were patterned on top of the self-assembled Au NP sample. This could be due to the low concentration of cross-linked Au NPs in

solution. The self-assembled Au NP sample was only immersed in the lift-off solution for 20 min. While this time is sufficient for Au NPs to self-assemble, that self-assembly occurs from a solution containing ~10^{13} Au NPs. This is seven orders of magnitude greater than the theoretical number of cross-linked Au NPs in the lift-off solution. Therefore, it could simply be that overnight immersion would be necessary to allow the cross-linked Au NPs to pattern on the self-assembled Au NP sample.

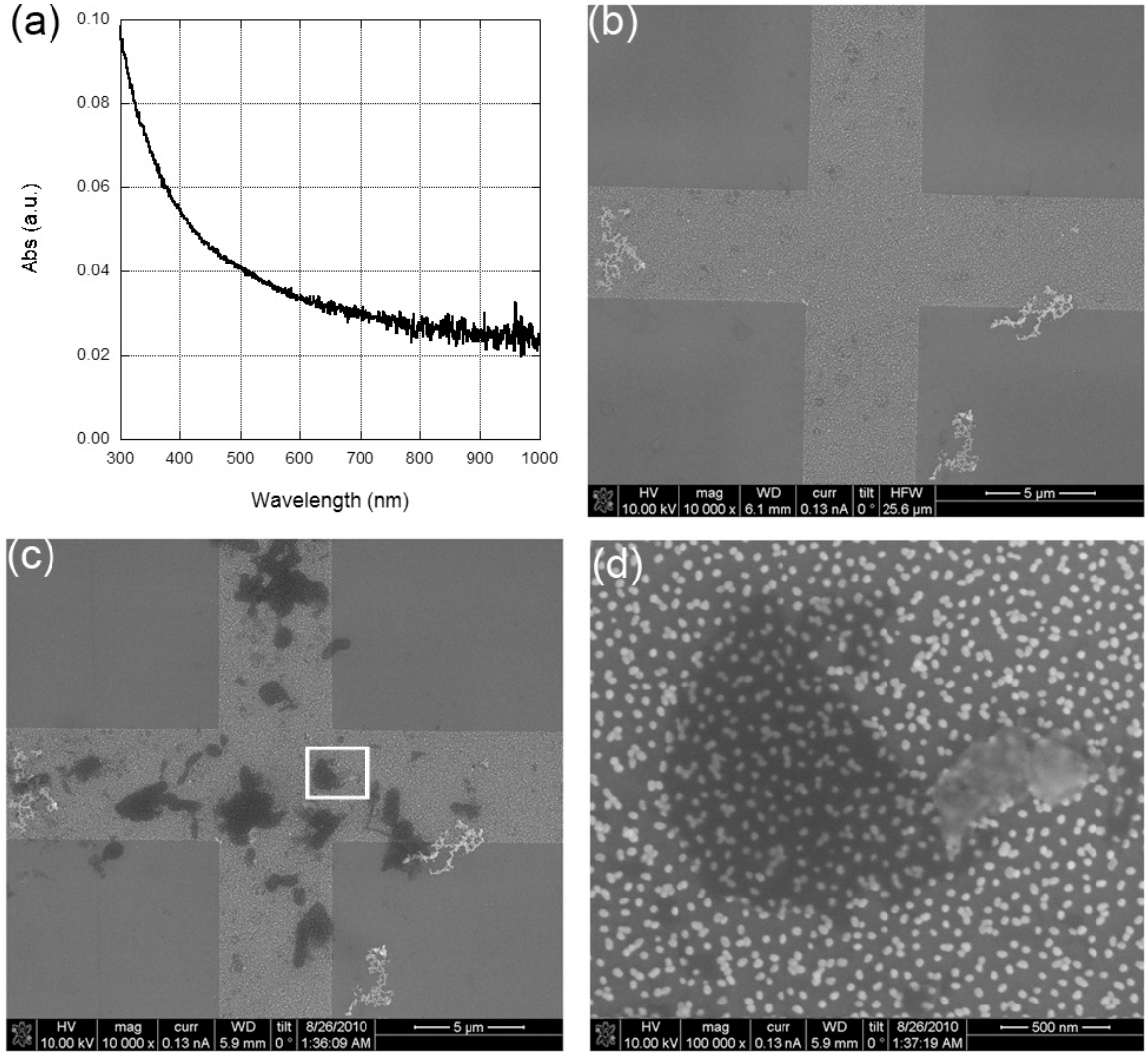

Figure 3.15 (a) UV-Vis of the 10 mM lift-off solution used to collect the PDDA cross-linked Au NPs. SEM images of a self-assembled Au NP sample (b) before and (c) after immersion into the NaOH lift-off solution. (d) A zoomed in image of the black spot encompassed by the white box in (c)

3.3.5 Effects of NaOH on Surface Chemistry

Since the self-assembly of the Au NPs is electrostatic, when the Au NPs are removed, the APDMES chemical template should still be intact and ready to self-assemble additional Au NPs. A self-assembled Au NP sample was cross-linked with PDDA and the Au NPs were lifted-off using sonication in 10 mM NaOH for 1 hr. The sample was then re-dipped in a Au NP solution to enable Au NPs to self-assemble on the APDMES pattern again. Figure 3.16 shows the same region of the same sample after the initial Au NP self-assembly, the lift-off, and the second Au NP self-assembly.

The initial Au NP self-assembly, as seen in Figure 3.16a, looks successful. There is fairly consistent self-assembly and no non-specific deposition. The lift-off appears to have been successful based on Figure 3.16b. The second self-assembly, as seen in Figure 3.16c, however, was not successful. There is Au NP deposition, but it is inconsistent, non-specific, and features large clumps of Au NPs. This would suggest that something happens to the chemical template during the lift-off process.

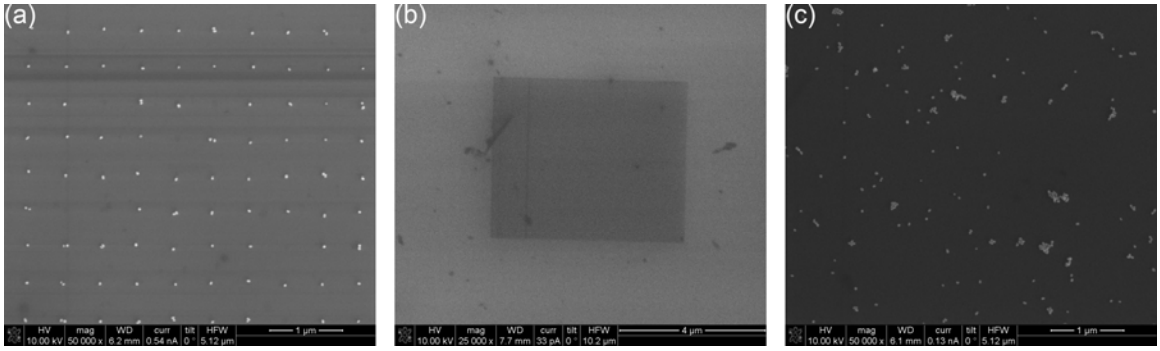

Figure 3.16 SEM images of a self-assembled Au NP sample (a) before and (b) after cross-linking with PDDA and sonication in 10 mM NaOH to induce Au NP lift-off, and (c) after an attempted second self-assembly of Au NPs.

To investigate if the lift-off process had any adverse effects on the APDMES chemical template, XPS and water contact angles were used to characterize a cleaned

piece of Si wafer, an APDMES coated piece of Si wafer, and an APDMES coated piece of Si wafer that was sonicated in 10 mM NaOH for 60 min to simulate the Au NP lift-off conditions. Table 3.1 lists the relative atomic percentages of Si 2p, C 1s, N 1s, and O 1s for the three samples, as determined by XPS.

Pieces of a Si wafer with a 45 nm thick, thermally grown oxide layer were cleaned by sonication in an acetone/IPA solution (1:1, v:v), then sonication in HNO_3, and an oxygen plasma treatment. The HNO_3 and oxygen plasma treatment hydroxylate the surface. This means that there are OH groups bonded to the Si atoms instead of just O atoms. This makes the surface very hydrophilic, no contact angle could be measured, and primes it for silanization. After the APDMES treatment, the contact angle of the surface is 62.85° ± 1.90°, which is moderately hydrophilic. This value seems to agree well with what has been reported in the literature.[13] However, after the NaOH sonication, the surface becomes so hydrophilic that the contact angle could not be measured. This would seem to suggest that the surface has reverted back to its hydroxylated state despite the APDMES coating. Yet, the XPS data tell a different story.

The XPS data in Table 3.1 show a decreased amount of C 1s and an increased amount of N 1s for both of the APDMES coated samples. The decreased amount of C 1s is rather curious, since the addition of the APDMES should increase the amount of carbon present on the Si surface due to the silane's propyl-chain. However, since it is impossible to keep sample surfaces free from contamination, except maybe in the cleanest of clean rooms, it is expected that a "clean" wafer should show some type of signal for C 1s. Interestingly, the APDMES coated samples both showed a larger peak for alkyl-chain type carbon than the clean Si wafer. This increase in alkyl-chain carbon is

due to the propyl-chain in the APDMES. Since the majority of the C 1s peak on the clean wafer is not from alkyl-chain type carbon, but double-bonded carbons, it could be that atmospheric carbon contamination like CO_2, is adsorbed on the surface.

The XPS data for the N 1s peak shows an increase in N 1s composition for the APDMES coated samples over the clean wafer. The clean wafer still shows some N 1s composition, but this is most likely due to the N_2 atmosphere of the XPS chamber. In fact, the APDMES coated samples showed larger peaks for amine-type nitrogen than the clean wafer. This type of nitrogen is present as the amino-group in the APDMES. Thus, it makes sense that the increased amount of amine-type nitrogen would correspond to the APDMES coated samples. What is also interesting is that both of the APDMES coated samples are composed of roughly the same amount of nitrogen. This would indicate that the lift-off conditions do not damage the silane or remove it from the Si substrate.

Table 3.1 Relative atomic percentages for a clean Si wafer, an APDMES coated Si wafer, and an APDMES coated Si wafer that was sonicated in 10 mM NaOH for 60 min. as determined by XPS

	Si 2p	**C 1s**	**N 1s**	**O 1s**
Clean wafer	38.19	10.95	0.38	50.48
APDMES	39.45	8.93	0.60	51.02
NaOH sonics	40.16	8.11	0.67	51.06

While the XPS data show that the APDMES is still present after the lift-off, the contact angle is very hydrophilic and no Au NPs self-assembled. The hydrophilic contact angle may be due to the amine group of the APDMES, which is deprotonated from the basic solution. However, the question still exists as to why the second Au NP self-assembly failed. The only difference between the XPS study and the actual lift-off conditions is that the actual lift-off conditions involve SEM imaging at some point prior to the lift-off. It could be that the electron beam of the SEM damages the silanes, a la

EBL, which would then prevent the silane from directing the self-assembly after the lift-off.

3.4 Conclusions

PDDA was used to cross-link self-assembled Au NPs. The PDDA was capable of enabling multi-layer Au NP self-assembly. However, additional Au NPs were often patterned off of the initial Au NPs due to the large molecular weight of the PDDA. When using PDDA, for the cross-linking, care should be taken to rinse the sample in D.I. H_2O to prevent loosely bound PDDA from coming off of the sample into the Au NP solution.

NaOH was used to lift-off PDDA cross-linked, self-assembled Au NPs from an APDMES chemical template. While no lift-off was observed using 1 mM NaOH, lift-off was observed at higher concentrations of NaOH when combined with sonication. Sonication was required to lift-off the Au NPs due to van der Waals forces binding the Au NPs to the substrate despite the lack of electrostatic forces binding the Au NPs at the surface.

Visualizing the lifted-off Au NPs via UV-Vis is highly unlikely since the number of lifted-off particles is several orders of magnitude less than the detection limit of the UV-Vis. Indirect observation of the Au NPs using an additional self-assembly of the lifted-off, crosslinked Au NP sample proved unsuccessful, but may have succeed if greater immersion time was allowed. Self-assembling several orders of magnitude more Au NPs may allow the lifted-off Au NPs to be detected by UV-Vis.

Sonication in NaOH does not appear to affect the APDMES, as XPS confirmed similar surface chemistry of an APDMES coated sample both before and after the

sonication in NaOH. The hydrophilic contact angle of the sample may be a result of the deprotonation of the APDMES from the NaOH exposure.

3.5 References

1. Lee, I.; Zheng, H. P.; Rubner, M. F.; Hammond, P. T., Controlled cluster size in patterned particle arrays via directed adsorption on confined surfaces. *Adv. Mater.* **2002,** *14* (8), 572-577.
2. Gole, A.; Murphy, C. J., Polyelectrolyte-Coated Gold Nanorods: Synthesis, Characterization and Immobilization. *Chem. Mat.* **2005,** *17* (6), 1325-1330.
3. Zheng, H. P.; Lee, I.; Rubner, M. F.; Hammond, P. T., Two component particle arrays on patterned polyelectrolyte multilayer templates. *Adv. Mater.* **2002,** *14* (8), 569-572.
4. Kim, H.-J.; Lee, K.; Kumar, S.; Kim, J., Dynamic Sequential Layer-by-Layer Deposition Method for Fast and Region-Selective Multilayer Thin Film Fabrication. *Langmuir* **2005,** *21* (18), 8532-8538.
5. Manandhar, P.; Akhadov, E. A.; Tracy, C.; Picraux, S. T., Integration of Nanowire Devices in Out-of-Plane Geometry. *Nano Letters* **2010,** *10* (6), 2126-2132.
6. Gunanathan, C.; Ben-David, Y.; Milstein, D., Direct Synthesis of Amides from Alcohols and Amines with Liberation of H2. *Science* **2007,** *317* (5839), 790-792.
7. Carey, F. A., *Organic Chemistry*. 5th ed.; McGraw-Hill: New York, 2003.
8. Brust, M.; Walker, M.; Bethell, D.; Schiffrin, D. J.; Whyman, R., SYNTHESIS OF THIOL-DERIVATIZED GOLD NANOPARTICLES IN A 2-PHASE LIQUID-LIQUID SYSTEM. *J. Chem. Soc.-Chem. Commun.* **1994,** (7), 801-802.
9. Porta, F.; Krpetić, Z. e.; Prati, L.; Gaiassi, A.; Scarì, G., Gold-Ligand Interaction Studies of Water-Soluble Aminoalcohol Capped Gold Nanoparticles by NMR. *Langmuir* **2008,** *24* (14), 7061-7064.
10. Jana, N. R.; Gearheart, L.; Murphy, C. J., Seed-Mediated Growth Approach for Shape-Controlled Synthesis of Spheroidal and Rod-like Gold Nanoparticles Using a Surfactant Template. *Adv. Mater.* **2001,** *13* (18), 1389-1393.
11. Jana, N. R.; Gearheart, L.; Murphy, C. J., Wet Chemical Synthesis of High Aspect Ratio Cylindrical Gold Nanorods. *The Journal of Physical Chemistry B* **2001,** *105* (19), 4065-4067.
12. Ma, L.-C.; Subramanian, R.; Huang, H.-W.; Ray, V.; Kim, C.-U.; Koh, S. J., Electrostatic Funneling for Precise Nanoparticle Placement: A Route to Wafer-Scale Integration. *Nano Letters* **2007,** *7* (2), 439-445.
13. Pallandre, A.; Glinel, K.; Jonas, A. M.; Nysten, B., Binary nanopatterned surfaces prepared from silane monolayers. *Nano Letters* **2004,** *4* (2), 365-371.

Chapter 4

Directed Self-Assembly of Gold Nanorods Using a Chemically Patterned Template

4.1 Introduction

The self-assembly of Au NPs was accomplished using a chemical template, as described in Chapter 2. However, Au NRs are more promising for optical metamaterials because they are doubly resonant, and the longitudinal plasmon absorption is stronger than for Au NPs. Also, a NIM was previously fabricated using Au NRs.[1] Thus, the next step was to self-assemble Au NRs.

Since the electrostatic self-assembly of Au NPs with a chemical template was successful, Au NRs would be self-assembled in a similar fashion. As discussed in Section 1.1.3, Au NRs are synthesized in solution with CTAB as a surfactant. The CTAB forms a amphiphilic bilayer with positively charged ammonium heads and alkyl-chain tails. Thus, the Au NRs possess a positive charge, as synthesized.

Previous self-assemblies of Au NRs were in solution and mediated by the pH of the solution[2], a biotin-steptavidin end-to-end[3] and side-by-side linkage[4], mouse immunoglobin[5], dipole moments[6], and altering the solvent system[7-9]. There has also been limited self-assembly of polyelectrolyte coated Au NRs on surfaces via electrostatics.[10]

Three different approaches were used to electrostatically self-assemble Au NRs on a chemical template. The first approach involved coating the Au NRs with a polyelectrolyte to give the Au NRs a negative charge and using the aminosilane chemical

template that was used for the Au NP self-assembly. The second approach used the Au NRs as synthesized, coated with CTAB, and an EBL defined template of negatively charged polyelectrolyte. The third approach replaced the CTAB with a carboxylic acid terminated, thiol-functional molecule to give the Au NRs a negative charge and the APDMES chemical template that was used for the Au NP self-assembly.

4.2 Experimental

N-type/phosphorus Si <100> wafers were purchased from Silicon Valley Microelectronics. Poly(methyl methacrylate) (PMMA, PMMA 950k A2) was purchased from MicroChem. All other chemicals were purchased from Sigma Aldrich and used as received.

Zeta potential measurements were conducted on a Zetasizer Nano (Malvern Instruments). SEM was performed using a Phillips XL30 FEG and a FEI Nova Nanolab Dualbeam Focused Ion Beam Workstation and Scanning Electron Microscope TEM was performed using a Jeol 3011 HRTEM at 300 keV.

4.2.1 Polyelectrolyte-coated Au NRs Self-Assembled on an APTMS Chemical Template

Au NRs were synthesized as reported elsewhere.[11] A CTAB-capped Au NP seed solution was prepared by adding 0.3 mL of an ice-cold 10 mM $NaBH_4$ aqueous solution to an aqueous solution containing 4.7 mL of 0.1 M CTAB and 25 μL of 50 mM $HAuCl_4$. A growth solution was prepared by first adding 30 mL of 0.1 M CTAB, followed by additions of 0.3 mL of 50 mM $HAuCl_4$, 0.57 mL of 1.0 M HCl, 360 μL of 10 mM

$AgNO_3$, and 240 μL of 0.1 M L-ascorbic acid. The addition of ascorbic acid turns the solution colorless. 72 μL of the 5 min. old, CTAB-capped Au NP seed solution was added to the growth solution to initiate Au NR growth. The growth solution was kept at 30°C overnight for Au NR growth. Centrifugation at 10,000 *g* for 30 min. was performed twice to separate the Au NRs from excess CTAB and left-over starting materials. The supernatant was discarded each time and the Au NRs were re-dispersed in D.I. water after the first round of centrifugation.

CTAB-capped Au NRs were coated with the polyelectrolyte poly(sodium-4-styrenesulfonate) (PSS, average M_w ~70,000 g/mol, 30 wt. % in H_2O) as reported elsewhere.[10] After the second round of centrifugation, for every 1.5 mL of Au NR solution that was centrifuged, 1 mL of 1 mM NaCl solution and 0.2 mL of a solution containing 10 mg/mL PSS and 1 mM NaCl were added to the centrifuge tube. After 60 min. of incubation, the solution was centrifuged at 10,000 *g* for 30 min. After the supernatant was discarded and the solution was resuspended in D.I. H_2O, the solution was centrifuged process was repeated.

Chemical templates were generated using EBL. PMMA was spin-cast on Si wafers at 4000 rpm for 60 sec. to generate ~65 nm thick films. Wafers were baked at 150°C on a hotplate for 2 min. prior to spin-casting and baked again at 170°C in an oven for 30 min. after spinning. After EBL (Raith 150), samples were developed in an MIBK:IPA (1:3 v:v) solution for 20 sec., rinsed in IPA for 30 sec., and blown dry with N_2 gas. Oxygen plasma was used to remove any trace organics from the exposed Si surface.

3-aminopropyltrimethoxysilane (APTMS) was deposited onto the EBL patterned areas by placing the patterned sample in a desiccator under vacuum with 100 μL of APTMS overnight. The sample was then removed, rinsed sequentially with MeOH and D.I. H_2O, blown dry with Ar gas, and placed on a hotplate at 140°C for 30 min.

The PMMA resist was removed by sonicating the sample in acetone for 2 hrs. The newly exposed Si surface was coated with n-dodecyltrimethoxysilane (C12TMS) by placing the sample in a desiccator under vacuum overnight with 100 μL of C12TMS. The sample was then removed, rinsed sequentially with MeOH and D.I. H_2O, and placed on a hotplate at 140°C for 30 min.

Samples were immersed into a PSS-coated Au NR solution for 15 min. to allow for the self-assembly of the Au NRs on the APTMS pattern. SEM was used to characterize the Au NR self-assembly.

4.2.2 Self-assembly of Au NRs on an Electron-Beam Lithography Cross-linked Poly(sodium-4-styrenesulfonate) Template

Au NRs were synthesized as reported elsewhere.[11] A CTAB-capped Au NP seed solution was prepared by adding 0.3 mL of an ice-cold 10 mM $NaBH_4$ aqueous solution to an aqueous solution containing 4.7 mL of 0.1 M CTAB and 25 μL of 50 mM $HAuCl_4$. A growth solution was prepared by first adding 30 mL of 0.1 M CTAB, followed by additions of 0.3 mL of 50 mM $HAuCl_4$, 0.57 mL of 1.0 M HCl, 360 μL of 10 mM $AgNO_3$, and 240 μL of 0.1 M L-ascorbic acid. The addition of ascorbic acid turns the solution colorless. 72 μL of the 5 min. old, CTAB-capped Au NP seed solution was added to the growth solution to initiate Au NR growth. The growth solution was kept at

30°C overnight for Au NR growth. Centrifugation at 10,000 *g* for 30 min. was performed twice to separate the Au NRs from excess CTAB and left-over starting materials. The supernatant was discarded each time and the Au NRs were re-dispersed in D.I. H_2O.

Patterns of EBL cross-linked PSS were prepared as described elsewhere.[12] A 0.5 wt. % filtered 1:2 v/v H_2O:EtOH solution of PSS was prepared and spin-coated at 5000 rpm for 60 sec. on a Si wafer to achieve an ~20 nm thick film of PSS. PSS was cross-linked using EBL with a 2,000 μC/cm^2 exposure dose. Samples were developed in D.I. H_2O, which removed all of the PSS except that which was cross-linked by the EBL. Oxygen plasma was then used to remove any trace organics on the Si wafer surface.

C12TMS was deposited on the bare Si surface by placing the sample in a desiccator under vacuum overnight with 100 μL of C12TMS. The sample was then removed, gently rinsed sequentially with MeOH and D.I. H_2O, and placed on a hotplate at 140°C for 30 min.

The cross-linked PSS sample was immersed into a solution of twice-washed, CTAB-coated Au NRs to allow the Au NRs to self-assemble on the PSS features. SEM was used to view the self-assembled Au NRs.

4.2.3 Self-assembly of 11-Mercaptoundecanoic-coated Au NRs on an APDMES Chemical Template

Au NRs were synthesized as reported elsewhere.[11] A CTAB-capped Au NP seed solution was prepared by adding 0.3 mL of an ice-cold 10 mM $NaBH_4$ aqueous solution to an aqueous solution containing 4.7 mL of 0.1 M CTAB and 25 μL of 50 mM $HAuCl_4$. A growth solution was prepared by first adding 30 mL of 0.1 M CTAB, followed by

additions of 0.3 mL of 50 mM $HAuCl_4$, 0.57 mL of 1.0 M HCl, 360 μL of 10 mM $AgNO_3$, and 240 μL of 0.1 M L-ascorbic acid. The addition of ascorbic acid turns the solution colorless. 72 μL of the 5 min. old, CTAB-capped Au NP seed solution was added to the growth solution to initiate Au NR growth. The growth solution was kept at 30°C overnight for Au NR growth. Centrifugation at 10,000 *g* for 30 min. was performed twice to separate the Au NRs from excess CTAB and left-over starting materials. The supernatant was discarded each time and the Au NRs were re-dispersed in D.I. H_2O after the first centrifugation.

The ligand exchange of CTAB for 11-mercaptoundecanoic acid (MUA) was performed as reported elsewhere.[6] After the second round of centrifugation, the concentrated Au NRs are re-dispersed in an aqueous, 20 mM MUA, 100 mM NaOH solution and allowed to incubate overnight. The solution is then centrifuged for 30 min. at 10,000 *g*. The supernatant is discarded and the Au NRs are re-dispersed in 100 mM NaOH. Centrifugation is repeated three more times.

To return the MUA-capped Au NR solution to a neutral pH, the solution is either centrifuged an additional three times, but re-suspended in D.I. H_2O each time, or 10 mL of the Au NR solution is dialyzed overnight against 2 L of D.I. H_2O with 3,500 MWCO dialysis tubing.

APDMES chemical templates were prepared as described in Section 2.2.1 and 2.2.2. PMMA was spin-cast on Si wafers with a 45 nm thick, thermally grown oxide at 4000 rpm for 60 sec. to generate ~65 nm thick films. Wafers were baked at 150°C on a hotplate for 2 min. prior to spin-casting and baked again at 170°C in an oven for 30 min. after spinning. After EBL (Raith 150), samples were developed in an MIBK:IPA (1:3

v:v) solution for 20 sec., rinsed in IPA for 30 sec., and blown dry with N_2 gas. Oxygen plasma was used to remove any trace organics from the exposed Si surface.

The exposed Si wafer surface was functionalized with APDMES by placing the samples into a desiccator with 100 μL of silane in a watch glass, pulling a vacuum, and leaving the desiccator overnight. Samples were then rinsed with MeOH and D.I. H_2O, and blown dry with Ar. Then, the samples were placed on a hotplate at 50°C for 3 hrs.

APDMES chemical template samples were vertically immersed in the MUA-capped Au NR solution for 30, 60, or 120 min. to allow the Au NRs to self-assemble on the APDMES chemical template. The samples were removed at 10 μm/s. SEM was used to visualize the Au NR self-assembly.

4.3 Results and Discussion

4.3.1 Polyelectrolyte-coated Au NRs Self-assembled on an APTMS Chemical Template

Au NRs were coated with PSS by a charge-charge interaction between the CTAB and the PSS. The zeta potential of the Au NR solution after coating the Au NRs with PSS was -29.8 mV, indicating that the Au NRs have a negative surface charge. Relatively, the zeta potential of CTAB coated Au NRs was +36.3 mV, indicating a positive surface charge.

Chemical template of APTMS dots were immersed into the PSS-coated Au NR solution for 15 min. One of the chemical templates had the rest of the Si surface coated with C12TMS and one template just had bare Si. Figure 4.1 shows the SEM of the

APTMS dots for both samples. For the sample with C12TMS (Figure 4.1a) there is minimal self-assembly, but it is limited to the APTMS patterned areas. For the sample with base Si (Figure 4.1b), there was also minimal self-assembly that was limited to the APTMS patterned areas, but there were also areas where there was a lot of non-specific deposition. The non-specific deposition is most likely due to the fact that there is nothing preventing the Au NRs from depositing on the bare Si. With the C12TMS, a hydrophobic layer is present, which deters the water soluble Au NRs from depositing.

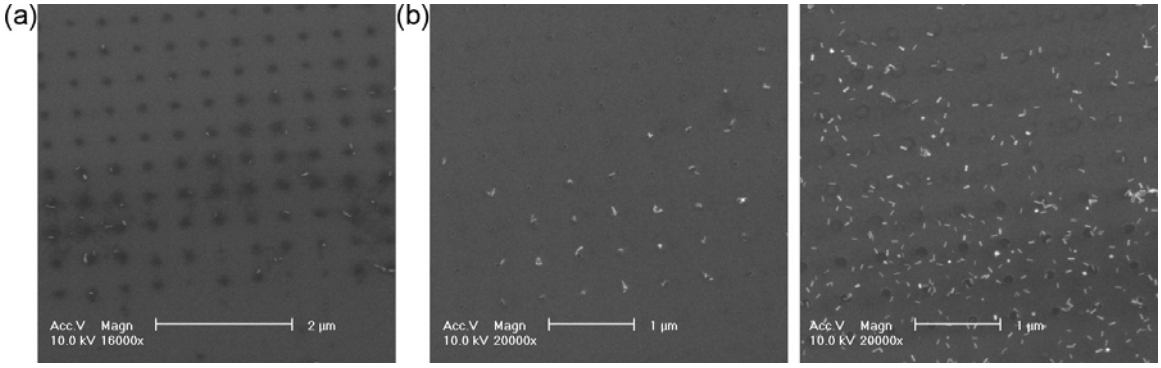

Figure 4.1 SEM images of self-assembled PSS-coated Au NRs on an APTMS chemical template (a) with C12TMS coating the rest of the Si surface and (b) with nothing coating the rest of the Si surface.

Additional samples of APTMS chemical templates with C12TMS covering the remaining Si were prepared. The samples were dipped in the PSS-coated Au NRs for 15 min. and imaged via SEM. Figure 4.2a shows a characteristic image from these samples. There is minimal self-assembly of the Au NRs on the APTMS chemical template. In order to determine if there was a problem with the APTMS or C12TMS that was inhibiting the Au NR self-assembly, the sample was immersed into a solution of citrate-capped Au NPs and then imaged again with SEM (Figure 4.2b). Based on the good self-assembly of the citrate-capped Au NPs, it is safe to say that the silanes are not inhibiting the Au NR self-assembly.

Since the silanes are not inhibiting the Au NR self-assembly, then the Au NRs themselves must be inhibiting the self-assembly. Despite the negative zeta potential of the solution, the Au NRs may not have a good PSS monolayer coating them. The molecular weight of the PSS used to coat the Au NRs was 70,000 g/mol. Previous attempts to coat Au NRs with this size PSS required Au NRs that were 500-600 nm in length and 25-30 nm in width to ensure that the PSS fully coated the Au NRs without any excess PSS dangling off of the Au NRs.[10] For the Au NRs used here, they were ~65 nm long and ~15 nm wide. Due to the shorter sized Au NRs, a smaller molecular weight PSS should have been used to prevent electrostatic bridging of Au NRs by the same PSS molecule and to ensure good wrapping of the Au NR with the PSS molecule.[13] However, no smaller PSS was commercially available at the time. The other option would have been to use larger Au NRs, but that would have required a different APTMS pattern.

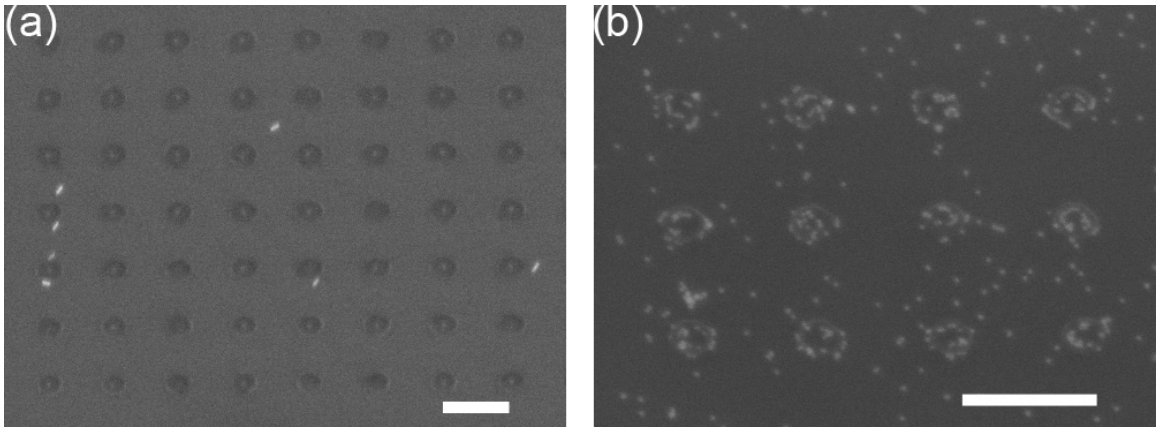

Figure 4.2 SEM images of (a) PSS-coated Au NRs self-assembled on an APTMS chemical template and (b) the same template with self-assembled citrate-capped Au NPs.

4.3.2 Self-assembly of Au NRs on an Electron-Beam Lithography Cross-linked Poly(sodium-4-styrenesulfonate) Template

Samples of PSS films on Si were patterned using EBL as described elsewhere.[12] Generally, EBL is used to write a pattern in PMMA, which acts as a positive resist. The electron-beam causes scission of the PMMA where it has been exposed, and these areas are developed. However, if a large enough exposure dose is used, the electron beam generates enough free electrons in the resist to cause the resist to cross-link.[14] The cross-linked resist will no longer be soluble in common solvents. Thus, a polymer resist like PMMA or PSS can be used as a negative resist.

EBL patterned samples of cross-linked PSS were developed by either spraying the sample with D.I. H_2O from a syringe, sonicating the sample in D.I. H_2O, or immersing the sample in D.I. H_2O. In all cases, the unexposed PSS was rinsed off of the sample, leaving only the cross-linked PSS.

CTAB-capped Au NRs were self-assembled by immersing a cross-linked PSS sample into the Au NR solution for 10 min. SEM was used to image the self-assembled Au NRs. Figure 4.3 shows the SEM images of the samples. The SEM images show lots of non-specific deposition of the Au NRs on the sample. Based on the image on the left, it looks like the Au NRs non-specifically deposit at a higher density than the Au NRs that are patterned on the PSS. This non-specific deposition may be due to incomplete removal of the PSS from the development step. Also, it is worth noting that the PSS pattern appears to be damaged in both SEM images. This damage is most likely from the 30 sec. of sonication that was used to remove the unexposed PSS.

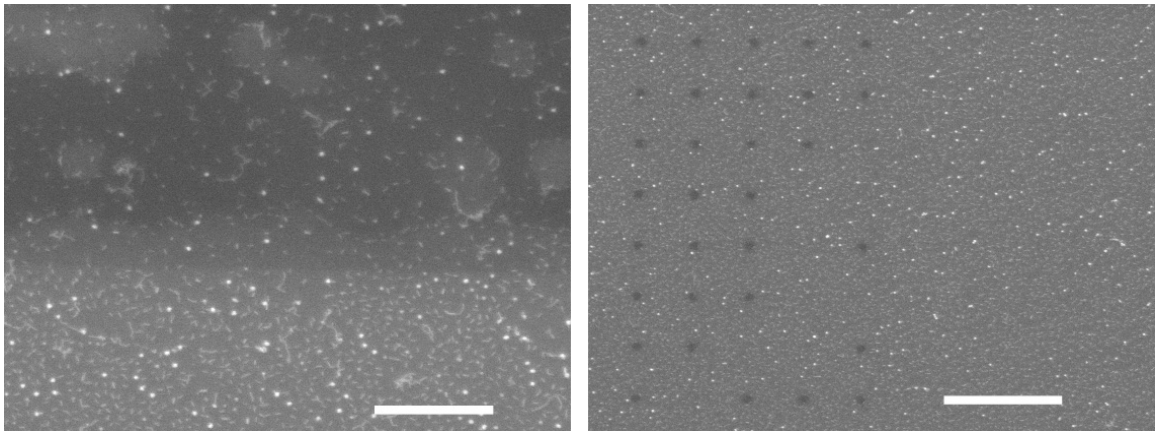

Figure 4.3 SEM images of CTAB-capped Au NRs self assembled on PSS chemical templates. Scale bars are 1 μm.

In order to prevent non-specific deposition of the Au NRs on the bare Si, the bare Si was coated with C12TMS after sonicating the sample for 30 sec. in D.I. H_2O to develop the sample. The C12TMS should provide a hydrophobic monolayer that will prevent the non-specific deposition of the hydrophilic Au NRs. SEM images of self-assembled Au NRs on the C12TMS treated, PSS sample are seen in Figure 4.4. Neither image shows any non-specific deposition of Au NRs, which means that the C12TMS served its purpose. However, there is still minimal patterning of the Au NRs and the PSS is again damaged.

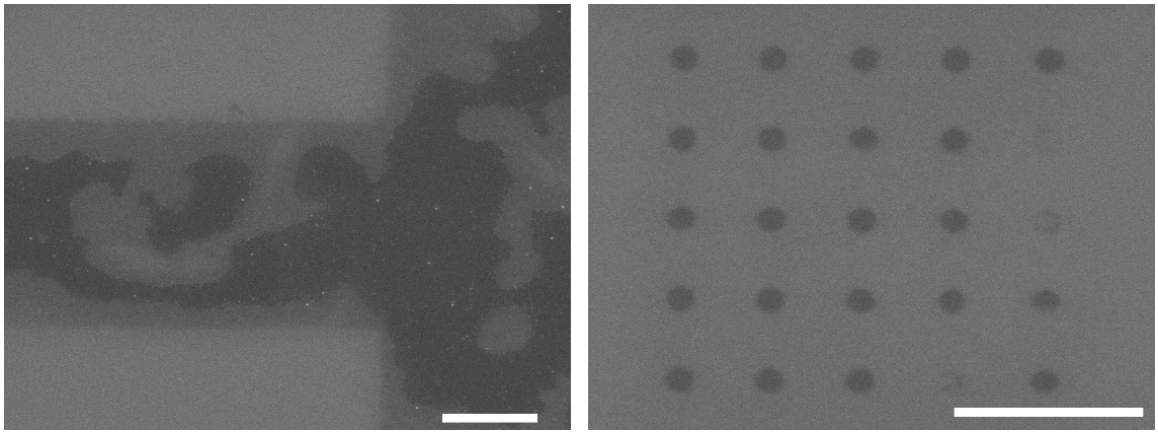

Figure 4.4 SEM images of CTAB-capped Au NRs self assembled on PSS chemical templates that have C12TMS coating the exposed Si. Scale bars are 2 μm.

In order to prevent the PSS pattern from being damaged during the development step, the exposed PSS samples were instead rinsed with 20 mL of D.I. H_2O from a syringe. Oxygen plasma was also used after development in order to remove any trace PSS that remained on the surface and to prime to the surface for C12TMS deposition. Three samples were prepared. Longer immersion times were also used to allow more time for the Au NRs to self-assemble. The first sample, **1**, was simply developed and immersed into the Au NR solution for 30 or 90 minutes to allow self-assembly. The second sample, **2**, was developed and treated with oxygen plasma before being immersed into the Au NR solution for 30 or 90 minutes. The third sample, **3**, was developed, received oxygen plasma, and was coated with C12TMS to make the non-patterned areas hydrophobic before being immersed into the Au NR solution for 30 or 90 minutes. SEM images of samples **1**, **2**, and **3** are seen in Figures 4.5, 4.6, and 4.7, respectively.

The rinsing with 20 mL of D.I. H_2O from a syringe seems to have had the desired effect. All of the PSS patterns in Figures 4.5 – 4.7 are still intact and do not appear damaged. Thus, sonication appears to be too rough on the patterns for development.

The SEM images show that there is non-specific deposition of Au NRs on sample **1**, but this was expected since it is essentially the same sample as in Figure 4.3. However, it should be noted that there are additional Au NRs self-assembled on the PSS after both 30 and 90 min. than seen in Figure 4.5. This is due to the longer immersion times of the PSS samples in the Au NR solution.

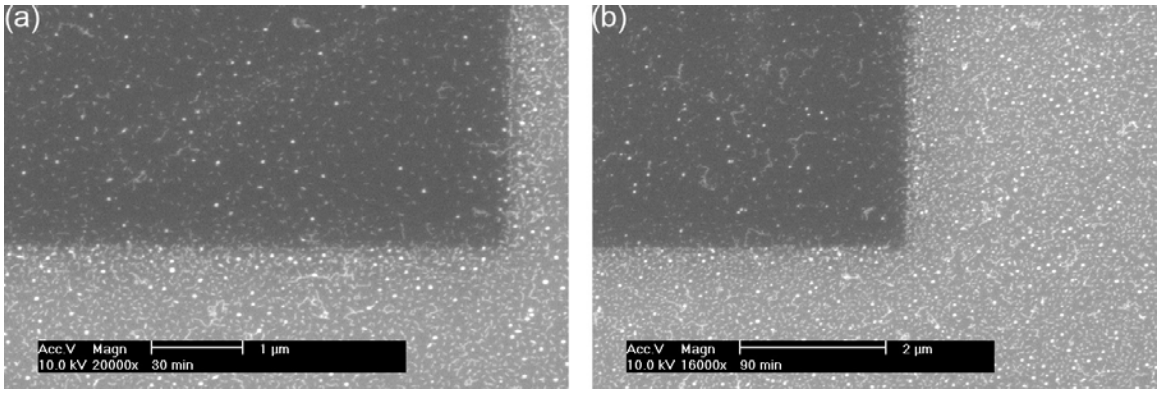

Figure 4.5 SEM images of self-assembled CTAB-coated Au NRs self-assembled on a cross-linked PSS sample after (a) 30 min. and (b) 90 min. of immersion. The dark rectangles are the patterned PSS.

For sample **2**, the SEM images show improved non-specific patterning of the Au NRs. In both the 30 and 90 min. images, the bare Si is not coated with Au NRs as it was for sample **1**. There is still some non-specific deposition, especially in Figure 4.6a, but this was a great improvement. Since the oxygen plasma seems to have prevented the massive non-specific deposition of the Au NRs, it would seem that the rinsing with D.I. H_2O works to develop the PSS pattern, but does not completely remove the PSS from the surface. The oxygen plasma, however, can clean away any leftover PSS and expose the bare Si surface.

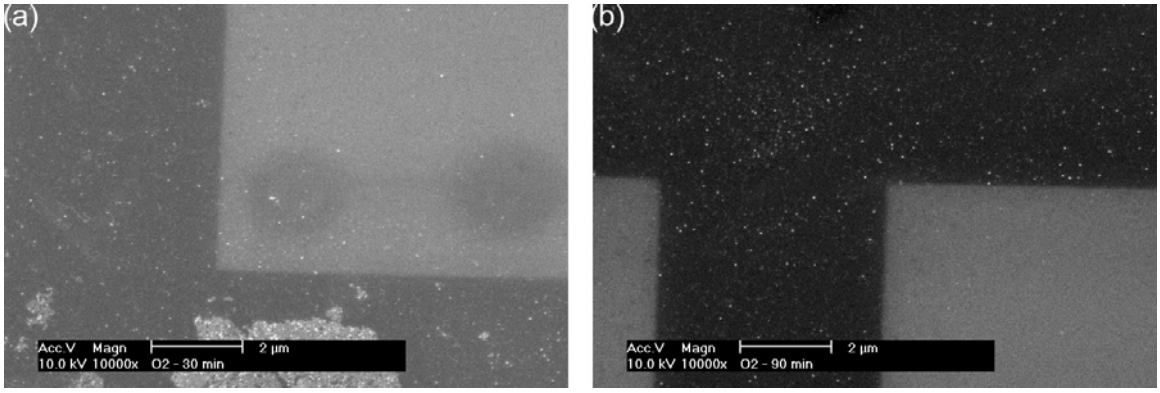

Figure 4.6 SEM images of self-assembled CTAB-coated Au NRs self-assembled on an oxygen plasma cleaned, cross-linked PSS sample after (a) 30 min. and (b) 90 min. of immersion.

Lastly, for sample **3**, the SEM images show good, selective self-assembly of the Au NRs on the PSS pattern. Like in the case of sample **2**, there is some non-specific deposition of the Au NRs. This is could be due to van der Waals interactions between the Au NRs and the Si surface, since the C12TMS provides a hydrophobic monolayer that repels the hydrophilic Au NRs. Also, the Au NRs may deposit on the C12TMS if the CTAB bi-layer is disrupted, which would expose the hydrophobic tail of the CTAB molecule that is bound to the Au NR. The exposure of the CTAB tail would enable preferential patterning on the hydrophobic C12TMS surface.

Figure 4.7c shows Au NRs patterned on 100 nm PSS squares. There is very good Au NR selectivity for the PSS pattern. It is interesting that the majority of the Au NRs that self-assemble on the PSS are seen on the perimeter of the PSS square. Unlike monolayers of silanes, the PSS has a surface height of ~30 nm, which exposes the sides for Au NR patterning. It is understandable that the Au NRs would prefer to have their longitudinal faces in contact with the PSS to maximize the electrostatic attraction between the CTAB ligand and the PSS. But, there are very few Au NRs on top of the PSS squares, even though the PSS surface is large enough to seat an entire Au NR.

A possible explanation is that when the Au NRs are drawn to the PSS squares, they are not static. The electrostatic force keeps them in proximity, but the Brownian motion of the Au NR allows it to move along the PSS surface. However, once the PSS template is removed from solution, the Au NRs no longer have a medium to move around in and they must stick to the PSS. One reason that the Au NRs are almost exclusively seen on the sides of the PSS is because a meniscus can more favorably form between the PSS square and the SiO_2 surface than on the PSS square's surface. Thus, the Au NRs

would be directed to the sides of the PSS squares since the solution can better wet the sides of the squares.

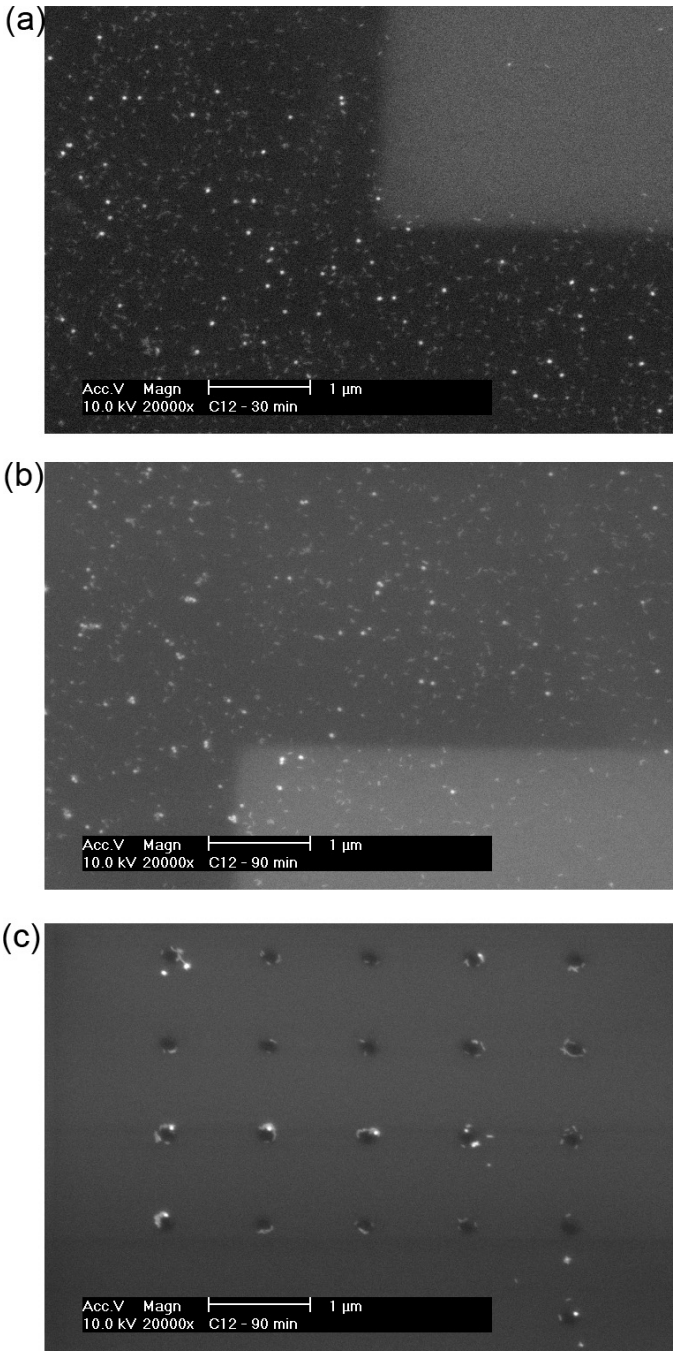

Figure 4.7 SEM images of self-assembled CTAB-coated Au NRs self-assembled on a C12TMS coated, cross-linked PSS sample after (a) 30 min. and (b) and (c) 90 min. of immersion. Large alignment marks are seen in (a) and (b), while an array 100 nm squares are seen in (c).

Another reason that the Au NRs are almost exclusively seen on the sides of the PSS is because this may be the location that is most energetically favorable for the Au NRs as the PSS sample is removed from the aqueous medium. As discussed in section 3.3.3, the van der Waals binding energy becomes very strong as the gold colloid comes in close (< 10 nm) proximity of the template surface. If the Au NRs pattern along side the PSS squares, then they would be closer to the samples surface than if they were patterned on top of the PSS. Since the Au NRs are closer to the surface, the van der Waals forces are stronger and the interaction energy is maximized.

One way to reduce the tendency of the Au NRs to pattern along the sides of the PSS would be to reduce the PSS thickness to ~ 5 nm or less using oxygen plasma. If the PSS were made this thin, then the solution would not be able to preferentially wet the sides of the PSS squares and the van der Waals forces should significantly contribute to binding the Au NRs at the PSS surface instead of just contributing when the Au NRs are along the PSS square's side.

4.3.3 Self-assembly of 11-Mercaptoundecanoic-coated Au NRs on an APDMES Chemical Template

Synthesized Au NRs had dimensions of 65.7 ± 10.5 nm length and 13.3 ± 2.6 nm width. A TEM image and the UV-Vis absorption spectra of the Au NRs before and after being capped with MUA are seen in Figure 4.10. The UV-Vis shows that exchanging the CTAB for MUA does not alter the UV-Vis absorption of the Au NRs, indicating that no aggregation or geometrical change occurs during the ligand exchange. The TEM image shows some gold nanocubes in addition to Au NRs. These are common by-products of

Au NR synthesis.[15-17] After three rounds of centrifugation to reduce the pH of the solution, the pH of the MUA-capped Au NR solution is ~7.4 and the color of the solution is still red.

The ligand exchange of CTAB for MUA requires the MUA to be dissolved in a basic solution. The MUA is not soluble in D.I. H_2O because the carboxylic acid group is not completely deprotonated and the large hydrophobic, alkyl chain prevents the ligand from dissolving in the D.I. H_2O. However, it was previously reported that the MUA would be soluble in a pH = 10 solution of D.I. H_2O, which would ensure that the MUA is deprotonated.[6] Here, a 100 mM solution of NaOH in D.I. H_2O (calculated pH = 13) is used to ensure that the MUA is deprotonated. Sonication is used to help solubilize the MUA, since it has a tendency to clump together like flour in water when baking.

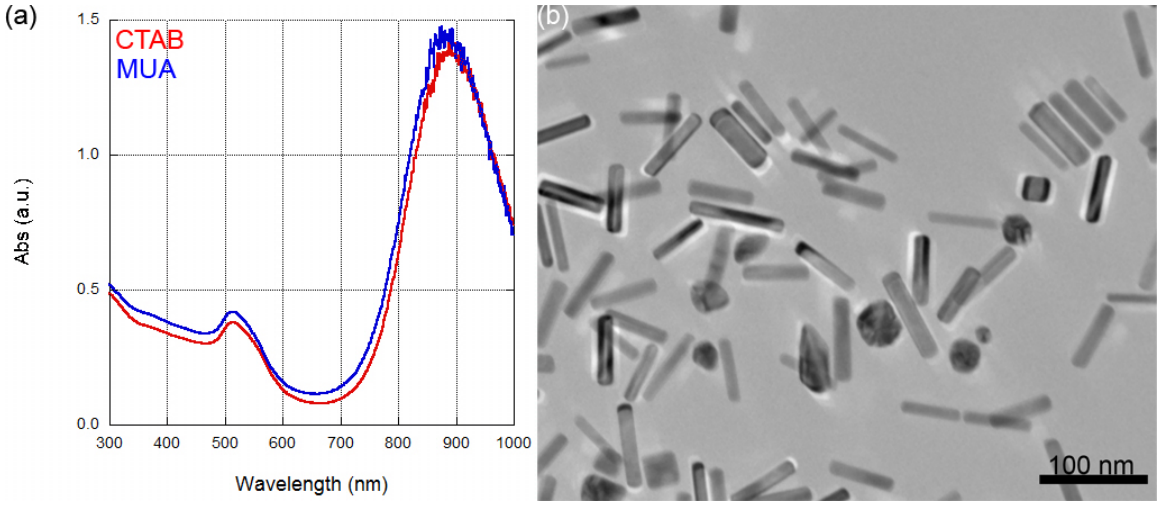

Figure 4.8 (a) UV-Vis absorption of Au NRs as synthesized with CTAB (red) and after the CTAB is replaced with MUA as the ligand (blue). (b) TEM image of the Au NRs.

Depending on how much CTAB is left over in the Au NR solution after centrifugation, the CTAB and deprotonated MUA may complex via a charge-charge interaction to form a white, flakey aggregate during the ligand exchange. If this occurs,

care must be taken to continue to centrifuge in 100 mM NaOH additional times until no more aggregate is visible. Sonication can fragment the aggregates in solution before centrifugation.

When performing the centrifugation to return the MUA-capped Au NR solution to a basic pH, it is critical not to centrifuge the solution too many times. A MUA-capped Au NR solution was centrifuged four times at 10,000 *g* for 30 min. and the Au NRs were re-dispersed in D.I. H_2O after discarding the supernatant. The Au NRs were soluble in the D.I. H_2O except after the fourth centrifugation. In this case, the Au NRs precipitated as a black solid on the side of the centrifugation tube. Only after sonication were the Au NRs re-suspended in the D.I. H_2O. However, the Au NR solution, which was previously red in color, was then purplish. UV-Vis absorption and a TEM image of the purplish Au NR solution are seen in Figure 4.9 Compared to the twice centrifuged Au NR solution, the four times centrifuged Au NR solution has drastically diminished surface plasmon absorption peaks that appear to be slightly red-shifted. This, in addition to the low-solubility of the Au NRs and the color change suggest that the Au NRs have aggregated. TEM, as seen in Figure 4.11b, confirmed large aggregates of the Au NRs.

The cause of this aggregation is not well understood. It also occurs while cleaning the CTAB coated Au NRs after three rounds of centrifugation. However, not all of the Au NRs are rendered insoluble like in the case of the MUA-capped Au NRs. Initially, it was thought that maybe the centrifugation was generating enough shear forces to remove the MUA from the surface. The force exerted on a MUA (M_w = 218.36 g/mol) molecule during the 10,000 *g* centrifugation was calculated to be 3.55 x 10^{-20} N.

$$F = M_w * a = \left(\frac{218.36\ g}{mol} * \frac{mol}{6.022*10^{23}} * \frac{kg}{1000\ g}\right) * \left(10000 * \frac{9.81\ m}{s^2}\right) = 3.55 * 10^{-20}\ N. \quad (1)$$

Multiplying this force by the length of a Au-S bond (~ 1 Å) yields an energy of 22.2 peV. The bond energy for the S-Au bond is 1.6 eV. Even if the Au NR was used in place of the MUA, the force and energy are still a few orders of magnitude below the S-Au bond energy (1.73 x 10^{-11} N, 11 meV). Thus, the centrifugation is not likely strong enough to simply shear away the MUA ligand from the Au NR surface.

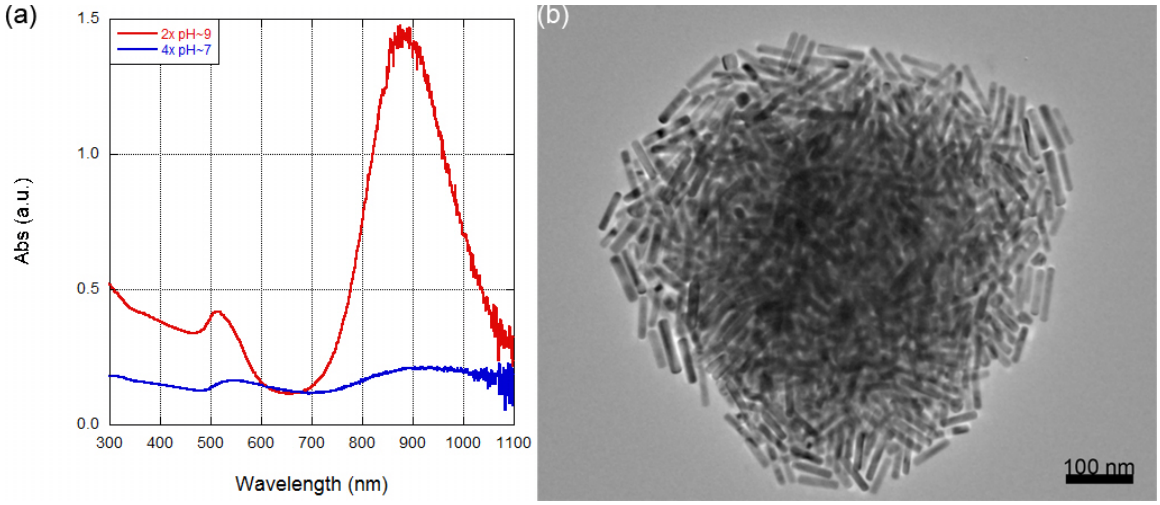

Figure 4.9 (a) UV-Vis absorption of MUA-capped Au NRs as they are returned to a neutral pH by centrifugation and resispersing in D.I. H_2O. Absorption spectra are shown for the MUA-capped Au NRs after two (red) and four (blue) rounds of centrifugation, when the pH of the Au NR solution is 9 and 7, respectively. (b) TEM of an aggregate of Au NRs from the 4x centrifuged solution.

However, the centrifugation force is still strong enough to force the Au NRs into a pellet. For the MUA coated Au NRs, as the pH is returned to a neutral state, the MUA has less of a tendency to be deprotonated. If the MUA coated Au NRs are not deprotonated, then there is no charge-charge repulsion between the Au NRs. As the Au NRs are forced together by the centrifugation, the hydrophobic alkyl chains of the MUA ligands may interact with each other to intertwine like a lipid bilayer. Since this interaction is entropically favorable, the hydrophobic alkyl chain does not want to be in the aqueous environment, it could be very difficult to separate the Au NRs after the MUA

ligands are intertwined. The aggregate seen in Figure 4.9b shows that most of the Au NRs are coupled side-by-side, which would allow for maximum MUA-MUA interaction. Furthermore, the heads of the Au NRs are also almost always oriented perpendicular to a Au NR side. Likewise, as the CTAB is removed during the centrifugation, the bi-layer of CTAB molecules that formed may be disrupted and a similar effect with the CTAB molecules may occur as theorized with the MUA ligands.

APDMES chemical template samples were dipped in a pH = 7.4 solution of MUA-capped Au NRs for 30 and 60 min. The Au NR solution was returned to a neutral pH using centrifugation. SEM images of the self-assembled Au NRs are seen in Figure 4.10. Au NRs were self-assembled on the alignment mark after 30 min. However, there was improved patterning on the aminosilane nanodots after 60 min. This suggests that the Au NRs require a longer time to self-assemble on the APDMES chemical template due the anisotropic shape and greater inertia of the Au NRs.

Dialysis was also used to reduce the pH of the MUA-capped Au NR solution to ~ 7. A 10 mL volume of the Au NR solution was placed in 3,500 MWCO dialysis tubing and left in a beaker containing 2 L of D.I. H_2O overnight. The pH of the D.I. H_2O increased from 7.4 to 7.9 and the resistance of the D.I. H_2O decreased from 1.8 MΩ to 0.8 MΩ, which both indicate that the dialysis was successful in removing NaOH from the Au NR solution. APDMES chemical templates were immersed in the dialyzed Au NR solution for 1 hr. and then imaged with SEM. Figure 4.11 shows the SEM of the large alignment mark.

Unlike the samples where the Au NRs were returned to a neutral pH by centrifugation, the dialyzed Au NRs did not pattern well (Figure 4.11). The color of the

Au NR solution became pinkish after the dialysis, but was reddish before the dialysis. The color change indicates that the Au NR solution has somehow changed. The most likely explanation is that the Au NRs aggregated during the dialysis, which would make them more difficult to pattern.

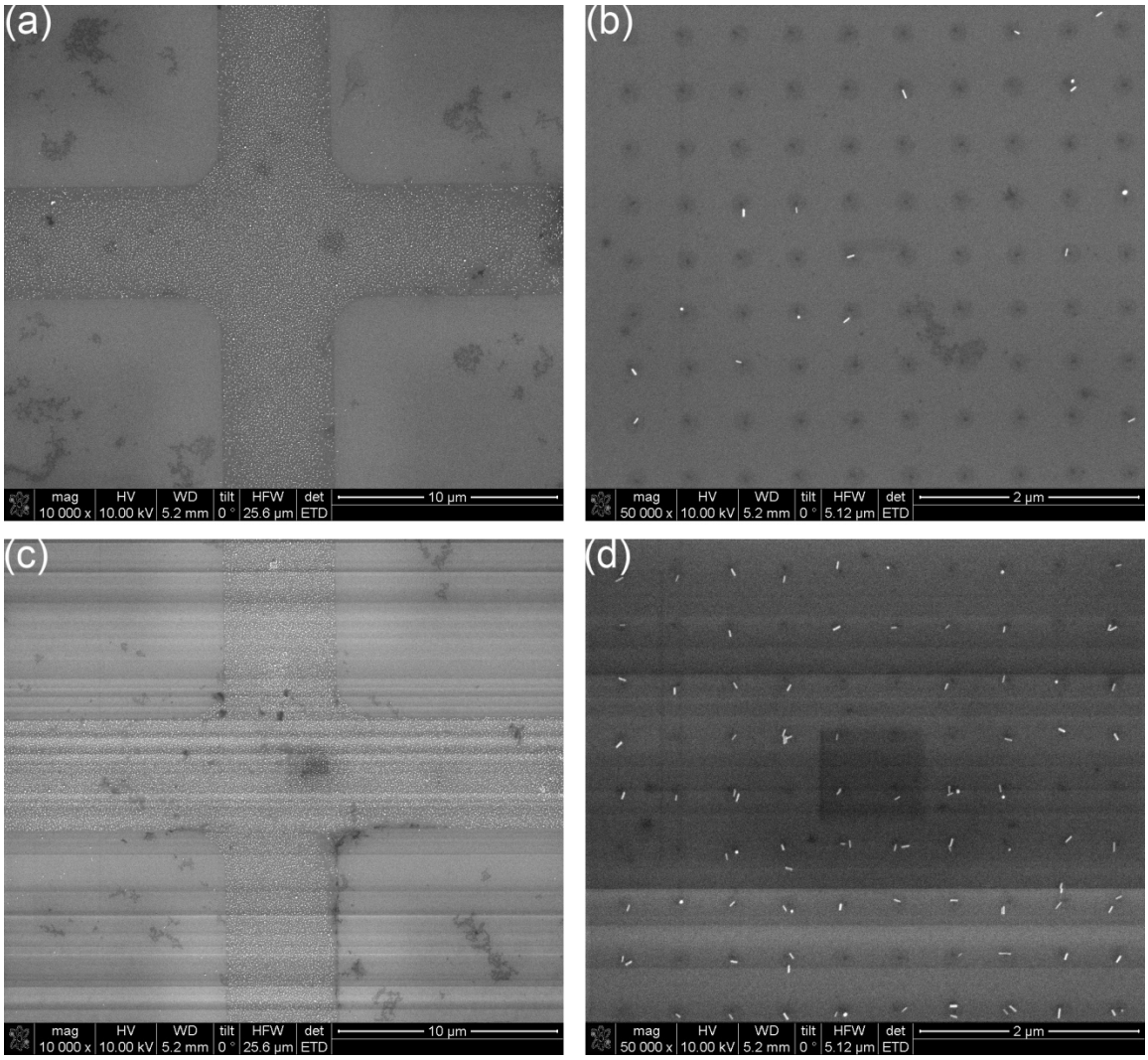

Figure 4.10 SEM of self-assembled MUA-capped Au NRs on an APDMES template after (a) and (c) 30 min. and (b) and (d) 60 min. of immersion in the Au NR solution. Images are of (a) and (c) a large alignment mark and (b) and (d) aminosilane dots.

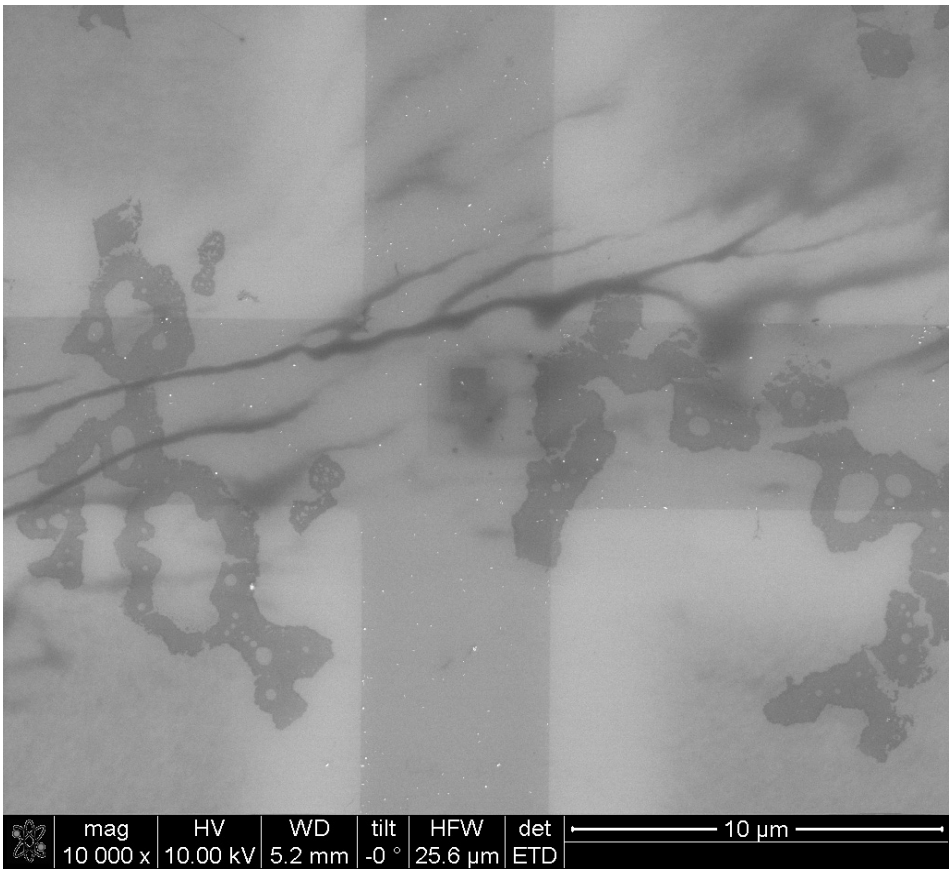

Figure 4.11 SEM of self-assembled MUA-capped Au NRs on an APDMES alignment mark. The Au NRs were returned to a neutral pH using dialysis.

4.4 Conclusions

Three techniques for self-assembling Au NRs on chemical templates via electrostatics have been presented. This first method, which uses polyelectrolyte coated Au NRs displayed limited success. This is most likely due to poor wrapping of the PSS on the CTAB-capped Au NR which results because the sizes of the PSS and the Au NR are not well matched for this technique.[10, 13] Using compatible PSS and Au NR sizes should improve the Au NR patterning.

The second method, which used a cross-linked PSS chemical template to self-assemble CTAB-coated Au NRs, displayed more success. Developing the cross-linked

PSS samples by sonicating in D.I. H_2O tended to damage the PSS pattern, while developing by rinsing with D.I. H_2O did not cause any damage. Oxygen plasma was used to remove any remaining PSS traces after development and C12TMS was deposited on the exposed SiO_2 surface in order to reduce the amount of non-specific deposition of AU NRs. However, these processes did not entirely prevent the non-specific deposition. Also, due to the relief height of the PSS pattern, Au NRs preferred to pattern on the sides of small PSS patterns instead of on the top of the PSS. The preference for the side patterning may be due to preferred wetting of the sides of the PSS squares by the solution and increased van der Waals forces when the Au NRs bind along the side of the PSS, since the Au NRs are closer to the substrate in this position. This effect may be resolved by using oxygen plasma to thin the PSS film to a height that would limit the ability of the solution to wet the sides of the PSS square and enable strong van der Waals forces when the Au NRs are on top of the PSS as well as when the Au NRs are on the edges of the PSS.

The final method, which used MUA-capped Au NRs and an APDMES chemical template displayed good self-assembly with minimal non-specific deposition. However, this technique suffered from slow self-assembly kinetics and inconsistent patterning of nano-sized APDMES patterns. The ligand exchange of MUA for CTAB proved to be sensitive to the pH of the solution. If the pH of the MUA-capped Au NR solution dropped too low, then the Au NRs would begin to aggregate due to insufficient electrostatic repulsion. Dialysis was also used to return the MUA-capped Au NR solution to a neutral pH, but this technique suffered from Au NR aggregation and poor Au NR patterning.

4.5 References

1. Shalaev, V. M.; Cai, W. S.; Chettiar, U. K.; Yuan, H. K.; Sarychev, A. K.; Drachev, V. P.; Kildishev, A. V., Negative index of refraction in optical metamaterials. *Opt. Lett.* **2005,** *30* (24), 3356-3358.
2. Orendorff, C. J.; Hankins, P. L.; Murphy, C. J., pH-Triggered Assembly of Gold Nanorods. *Langmuir* **2005,** *21* (5), 2022-2026.
3. Caswell, K. K.; Wilson, J. N.; Bunz, U. H. F.; Murphy, C. J., Preferential End-to-End Assembly of Gold Nanorods by Biotin−Streptavidin Connectors. *J. Am. Chem. Soc.* **2003,** *125* (46), 13914-13915.
4. Gole, A.; Murphy, C. J., Biotin−Streptavidin-Induced Aggregation of Gold Nanorods: Tuning Rod−Rod Orientation. *Langmuir* **2005,** *21* (23), 10756-10762.
5. Chang, J.-Y.; Wu, H.; Chen, H.; Ling, Y.-C.; Tan, W., Oriented assembly of Au nanorods using biorecognition system. *Chemical Communications* **2005,** (8), 1092-1094.
6. Walker, D. A.; Wilmer, C. E.; Kowalczyk, B.; Bishop, K. J. M.; Grzybowski, B. A., Precision Assembly of Oppositely and Like-Charged Nanoobjects Mediated by Charge-Induced Dipole Interactions. *Nano Letters* **2010,** *10* (6), 2275-2280.
7. Fava, D.; Nie, Z.; Winnik, M. A.; Kumacheva, E., Evolution of Self-Assembled Structures of Polymer-Terminated Gold Nanorods in Selective Solvents. *Adv. Mater.* **2008,** *20* (22), 4318-4322.
8. Nie, Z. H.; Fava, D.; Kumacheva, E.; Zou, S.; Walker, G. C.; Rubinstein, M., Self-assembly of metal-polymer analogues of amphiphilic triblock copolymers. *Nat. Mater.* **2007,** *6* (8), 609-614.
9. Nie, Z. H.; Fava, D.; Rubinstein, M.; Kumacheva, E., "Supramolecular" assembly of gold nanorods end-terminated with polymer "Pom-Poms": Effect of pom-pom structure on the association modes. *J. Am. Chem. Soc.* **2008,** *130* (11), 3683-3689.
10. Gole, A.; Murphy, C. J., Polyelectrolyte-Coated Gold Nanorods: Synthesis, Characterization and Immobilization. *Chem. Mat.* **2005,** *17* (6), 1325-1330.
11. Carbó-Argibay, E.; Rodríguez-González, B.; Pacifico, J.; Pastoriza-Santos, I.; Pérez-Juste, J.; Liz-Marzán, L. M., Chemical Sharpening of Gold Nanorods: The Rod-to-Octahedron Transition. *Angewandte Chemie International Edition* **2007,** *46* (47), 8983-8987.
12. Ofir, Y.; Samanta, B.; Xiao, Q.; Jordan, B. J.; Xu, H.; Arumugam, P.; Arvizo, R.; Tuominen, M. T.; Rotello, V. M., Polyelectrolyte negative resist patterns as templates for the electrostatic assembly of nanoparticles and electroless deposition of metallic films. *Adv. Mater.* **2008,** *20* (13), 2561-2566.
13. Gittins, D. I.; Caruso, F., Tailoring the Polyelectrolyte Coating of Metal Nanoparticles. *The Journal of Physical Chemistry B* **2001,** *105* (29), 6846-6852.
14. McCord, M. A.; Rooks, M. J., Electron Beam Lithography. In *SPIE's Handbook of Microlithography, Micromachining, and Microfabrication*, Rai-Choudhury, P., Ed. SPIE: Bellingham, Washington, 1997; Vol. 1, pp 139-250.
15. Jana, N. R.; Gearheart, L.; Murphy, C. J., Seed-Mediated Growth Approach for Shape-Controlled Synthesis of Spheroidal and Rod-like Gold Nanoparticles Using a Surfactant Template. *Adv. Mater.* **2001,** *13* (18), 1389-1393.

16. Jana, N. R.; Gearheart, L.; Murphy, C. J., Wet Chemical Synthesis of High Aspect Ratio Cylindrical Gold Nanorods. *The Journal of Physical Chemistry B* **2001,** *105* (19), 4065-4067.
17. Nikoobakht, B.; El-Sayed, M. A., Preparation and Growth Mechanism of Gold Nanorods (NRs) Using Seed-Mediated Growth Method. *Chem. Mat.* **2003,** *15* (10), 1957-1962.

Chapter 5

Spherical Assembly of Gold Nanoparticles via Good-solvent Evaporation Process

5.1 Introduction

One of the limitations of using chemical templates to self-assemble nanogold is that the chemical template cannot self-assemble large enough quantities of nanogold that can be easily detected. This problem was discussed in Section 3.2.4, where at least 10^8 Au NPs were needed to be detected by UV-Vis absorption. Thus, a technique was devised to self-assemble Au NPs in solution, in large quantities.

Several studies have demonstrated that the spherical assembly of Au NPs can be achieved by using ligand exchange reactions on the Au NP surface, which is called the mediator-template strategy.[1-5] These approaches exploit the difference in binding energy between Au NPs and the various ligand molecules. The weekly bound template molecules on the Au NPs are removed as the mediator molecules strongly bind to the Au NPs. The size of the spherical beads made from Au NPs could be controlled by the molar ratio of the mediator to the template-coated Au NPs.

It has been reported that submicron-sized polymeric beads can be prepared by using good-solvent evaporation methods.[6-8] The perfect dissolution of polymer with a good-solvent/poor-solvent mixture followed by the complete evaporation of good solvent from the polymer solution can generate monodisperse polymeric beads. The key factor of this method is choosing the correct good-solvent and poor-solvent for the selected

polymer: the two solvents must be miscible and the good-solvent must have a lower boiling point than the poor-solvent. For instance, THF and water can be used for polystyrene (PS) or PS-based block copolymers to prepare a uniform size of beads because THF is miscible with water and has a lower boiling point than water. We found that the CH_2Cl_2/trifluoroacetic acid (TFA) mixture solvent system also works very well for the bead formation using PS or PS containing polymers with this method.

Solvent-selectivity has also been used to assemble Au NRs which were end coated with PS and coated along the sides with CTAB.[9-11] By using mixtures of THF, DMF, and water, the rods were assembled into rings, chains, bundles, spheres, or chains of bundles, as seen in Figure 1.7.

A novel method was developed to prepare spherical assemblies of Au NPs by using a CH_2Cl_2/TFA solution via the good-solvent evaporation method. Au NPs were synthesized and passivated using thiol-terminated PS (HS-PS) to provide Au NPs with excellent solubility and stability in organic solvents. The dissolution of the resulting Au NPs into a CH_2Cl_2/TFA mixture and the subsequent evaporation of CH_2Cl_2 gives rise to the assembly of Au NPs. Various molecular weight HS-PS ligands and different Au NP sizes were tried with different evaporation conditions to control the size of the Au NP assemblies.

5.2 Experimental

Three samples of HS-PS ligands were received from Polymer Source, Inc. and used without further purification: HS-PS1100 (M_n = 1,100 g/mol, M_w/M_n = 1.12, ~11 PS units), HS-PS3000 (M_n = 3,000 g/mol, M_w/M_n = 1.07, ~29 PS units), and HS-PS6500 (M_n

= 6,500 g/mol, M_w/M_n = 1.18, ~63 PS units). All the other chemicals were used as received from Sigma Aldrich.

5.2.1 3 nm Au NP Synthesis

The Au NPs were synthesized by following the procedure as described elsewhere.[12, 13] 3.1 mg $HAuCl_4 \bullet 3H_2O$, 2.0 mg HS-PS1100, and 10 mL THF were added to a 20 mL vial. The solution was stirred for 5 min and then 0.1 mL $LiEt_3BH$ (1.0 M in THF) was added to the solution at once. After 5 min, the solution was stirred gently and left overnight to complete the reaction.

5.2.2 5 nm Au NP Synthesis

The Au NPs were synthesized by a two-phase method as described elsewhere.[3, 5, 14] To a 250 mL flask were added 550 mg tetraoctylammonium bromide (TOAB) and 32 mL toluene. The solution was stirred for 5 min and then 77 mg $HAuCl_4 \bullet 3H_2O$ dissolved in 20 mL water was added to the solution. The solution was stirred for 15 min. The organic layer was collected and 42 mg $NaBH_4$ dissolved in water was added drop wise to the solution. The solution was stirred at room temperature for 24 hrs. 2.6 mL of TOAB-coated Au NPs in the organic layer was taken and transferred to 20 mL flask. Under stirring, a solution of either 18 mg HS-PS1100, 48 mg HS-PS3000, or 63 mg HS-PS6500 dissolved in 2.5 mL toluene and 10 mL THF was added to the flask. The solution was kept stirring at least 24 hrs.

5.2.3 16 nm Au NP Synthesis

The Au NPs were synthesized as described elsewhere.[15] A solution containing 50 mg $HAuCl_4 \bullet 3H_2O$, 1.0 g of oleylamine, and 1.0 mL of toluene was quickly injected into a boiling solution of 1.7 g of oleylamine in 49 mL of toluene. After two hours, heating was stopped and 100 mL of MeOH was added to precipitate the product. The particles were washed by centrifugation at 6,000 *g* for 20 min. to isolate the particles. The supernatant was removed and discarded. The washing was performed three times with 50 mL of MeOH to remove unreacted starting materials and byproducts. After redispersing the particles in toluene, the particles were concentrated and dried in a glass vial using rotary-evaporation. The vial was further dried *in vacuo* for at least 24 hrs.

The solid Au NPs were resuspended in toluene to create a 2 mg/mL concentrated solution. A solution of 2.5 mL toluene and 10 mL THF was prepared with either 18 mg of HS-PS1100, 30 mg of HS-PS3000, or 50 mg of HS-PS6500. To the HS-PS solution, 2 mL of the Au NP solution was added under stirring. The solution was kept stirring overnight.

5.2.4 Purification of Au NPs

For HS-PS1100 functionalized Au NPs, the Au NP solution was concentrated and poured into MeOH. The unbound HS-PS1100 was removed by membrane filtration (MWCO 30,000 g/mol, Millipore Inc.) of the Au NPs using DMF and 1,4-dioxane, sequentially. Finally, the solid Au NPs were recovered by precipitation of the concentrated Au NPs/1,4-dioxane solution into MeOH followed by drying under vacuum for at least 24 hrs.

For HS-PS6500 functionalized Au NPs, the Au NP solution was separated into microcentrifugation tubes, and MeOH was added to precipitate the Au NPs. After centrifugation at 10,000 g for 20 min., the supernatant was removed and the particles were redispersed with 0.3 mL of toluene. 0.5 mL of MeOH was added to the centrifugation tubes, the tubes were shaken to mix the toluene and MeOH, and the centrifugation process was repeated until there was no free HS-PS left in the supernatant as indicated by thin-layer chromatography. Finally, Au NPs were concentrated and dried under vacuum for at least 24 hrs.

5.2.5 Au NPs Assembly by Good-solvent Evaporation

CH_2Cl_2 was added to the dried Au NPs to obtain a 1 g/L concentrated solution. 1 mL of the Au NP solution and an additional 6 mL of CH_2Cl_2 were added to 20 mL vial. The vial was lightly agitated to mix the Au NPs with the additional solvent. Then, 7 mL of TFA was added to the solution within 2 min. The solution was placed in a 100 foot/min. face velocity fume hood, uncapped at room temperature for the complete removal of CH_2Cl_2. The solution was either not stirred or stirred by a stir bar at either 600 or 1,200 rpm during the evaporation. The solution was left to induce the precipitation of aggregate of Au NPs. Assemblies of Au NPs were re-suspended in solution using sonication for 1 min.

5.2.6 Characterization

The Au NPs and spherical beads were characterized by transmission electron microscopy (TEM) on a JEOL 3011 TEM operating at 300 keV. Samples for TEM were

prepared by drop-casting the solution onto carbon-coated copper grids (Ted Pella) and drying the solvent at room temperature. Prepared TEM grids were also analyzed via SEM using either a Phillips XL30 FEG SEM or a Nova Nanolab FIB/SEM. UV-Vis absorption spectra were acquired over the range of 300 - 1000 nm using a Varian Cary 50 spectrophotometer.

5.3 Results and Discussion

5.3.1 Au NP Synthesis and Purification

The syntheses of Au NPs were carried out by the reduction of $HAuCl_4 \bullet 3H_2O$ with $LiEt_3BH$ in THF, with $NaBH_4$ in toluene/water, or with oleylamine in boiling toluene. HS-PS was used as the organic stabilizing ligand of the Au NPs. For Au NPs produced with $LiEt_3BH$, only a low molecular weight HS-PS could be used. From this Au NP synthesis technique, as the molecular weight of the HS-PS increases, the size of the Au NPs increases as well.[13] This occurs because the larger molecular weight HS-PS sterically hinders additional ligands from attaching to the small Au NPs, and thus the Au NPs must be larger in order to achieve the necessary areal polymer density on the Au NP surface to stabilize the Au NPs in solution. However, with the two-phase synthesis and the oleylamine techniques, the particles are synthesized before they are passivated with HS-PS. Thus, HS-PS of various molecular weights could be used with particles produced via these recipes.

From the $LiEt_3BH$ synthesis, 2.5 ± 1.6 nm diameter Au NPs (Au NP_3) were coated with HS-PS1100 to obtain Au NP_3@PS1100. From the two-phase synthesis, 5.4 ±

1.8 nm diameter Au NPs (Au NP_5) were coated with HS-PS1100 and 4.1 ± 1.5 nm diameter Au NPs were coated with HS-PS6500 to obtain Au NP_5@PS1100 and Au NP_5@PS6500, respectively. Lastly, from the oleylamine in toluene synthesis, 16.0 ± 2.0nm Au NPs (Au NP_{16}) were coated with HS-PS1100 and HS-PS6500 to obtain Au NP_{16}@PS1100 and Au NP_{16}@PS6500. The sizes of the Au NPs were determined by analyzing the TEM images of the Au NP samples.

The unbound HS-P1100 from the Au NP@PS1100 solutions was effectively isolated by membrane filtration of Au NP solution. The unbound HS-PS6500 were effectively isolated from the Au NP solutions by repeated centrifugation and resuspension of the Au NP solutions. At least five rounds of centrifugation were required to remove the unbound HS-PS6500.

5.3.2 Assembly of Au NPs as the Good-solvent Evaporates

The assembly of Au NPs was conducted by the good-solvent evaporation method as shown in Figure 5.1. The selection of good-solvent and poor-solvent for polymeric materials is crucial for the preparation of uniform beads. When equal volumes of CH_2Cl_2 and TFA were added to Au NPs, the Au NP@PS were completely dissolved in the solution. As the volume of the solution decreased due to the evaporation of CH_2Cl_2 the resulting solution became hazy and changed color, indicating poor solubility of the Au NPs and the formation of submicron-sized beads in the solution. Ultimately, once all of the CH_2Cl_2 evaporated, the assemblies of Au NPs would precipitate out of solution.

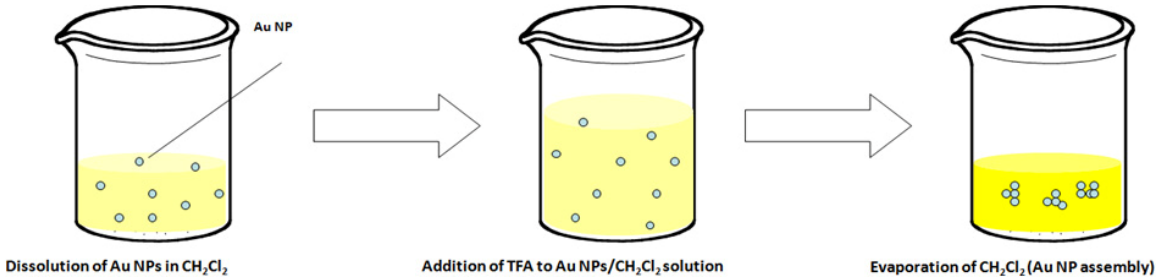

Figure 5.1 Method for producing assemblies of HS-PS capped Au NPs via good-solvent evaporation.

UV-Vis was used to monitor the evolution of the Au NP bead assembly for Au NP_3@PS1100 assembly under 1200 rpm stirring. The UV-Vis spectra of the Au NP solution after 5, 7.5, and 9 hrs. are seen in Figure 5.2. After 5 hrs. of stirring, the solution changed colors from red to purplish, indicating that some Au NP aggregation had begun. The UV-Vis spectrum shows a peak centered at 550 nm, which is slightly red-shifted from the surface plasmon peak of the Au NP_3 (Figure 5.3a). As the stirring continued, at 7.5 hrs, the solution turned a bluish color and the UV-Vis absorption was even more red-shifted, indicating larger aggregates of the Au NPs. Finally, after 9 hrs., the solution was colorless and a film was seen on the bottom of the vial. At this point, there was ~ 2 mL of solvent left in the vial. The UV-Vis of the solution showed a very weak and very broad absorption peak. However, after sonicating the solution, color returned to the solution and a sharper absorption peak was seen from the UV-Vis.

Based on the evolution of the UV-Vis spectra, it would appear that small aggregates of Au NPs form as the CH_2Cl_2 evaporates and the solubility of the Au NPs in the solution decreases. As more CH_2Cl_2 evaporates, the aggregates get larger, presumably from a combination of smaller aggregates fusing together and individual Au NPs joining the aggregates.

UV-Vis absorption spectra and TEM images of the microbeads formed under no stirring, 600 rpm stirring, and 1200 rpm stirring from Au NP_3@PS110, Au NP_5@PS110, Au NP_{16}@PS1100, Au NP_5@PS6500, and Au NP_{16}@PS6500 are seen in Figures 5.3, 5.4, 5.5, 5.6, and 5.7, respectively. The sizes of the assembled microbeads for the various sizes of Au NPs, molecular weights of HS-PS, and stirring conditions are summarized in Table 5.1.

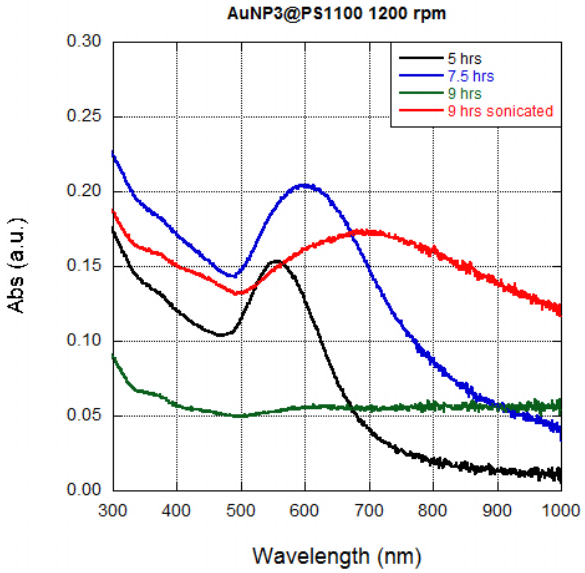

Figure 5.2 UV-Vis absorption spectra of a solution of Au NP3@PS1100 in a mixture of CH_2Cl_2 and TFA as the CH_2Cl_2 evaporates under 1200 rpm stirring.

Microbead assemblies generated from larger molecular weight HS-PS are generally smaller than those generated from lower molecular weight HS-PS. This is likely because the larger molecular weight HS-PS is less soluble in higher concentrations of TFA and the Au NP microbead assemblies precipitate out of solution faster.

No microbead formation was observed for the Au NP_{16}@PS110 system under any evaporation conditions. The UV-Vis absorption spectra show broadened peaks after the CH_2Cl_2 evaporation, but the TEM images only showed arbitrary aggregation. This

arbitrary aggregation may be the cause of the broadened UV-Vis spectra. However, the Au NP_{16}@PS1100 may have formed small microbeads that were not distinguishable in the TEM images. These microbeads may have only been a few Au NPs in size, and therefore indistinguishable from otherwise random aggregation.

In order to get a different view of the aggregates, the TEM grid was imaged via SEM. Figure 5.8 shows SEM images of the TEM grids for the Au NP_{16}@1100 assemblies generated by no stirring and 1200 rpm evaporation. Neither SEM image shows any well defined spherical structures, but both images show large aggregates of the Au NPs. Unfortunately, the SEM image for the evaporation with no stirring, Figure 5.8a, is only zoomed in to 20kx. Higher magnifications were attempted, but there was too much image distortion due to charging effects on the sample. However, Figure 5.8b is zoomed in to 100kx, and individual Au NPs can be resolved. In Figure 5.8b there are no visible distinct spheres, mainly due to the large amount of aggregation. If the SEM image is closely inspected, it is possible to make out what looks like spherical assemblies of Au NPs. Still, the spheres were not well-defined enough to properly assess any microbead assembly from the Au NP16@PS1100 solutions.

As a contrast to Figure 5.8, Figure 5.9 shows SEM images of the Au NP_{16}@PS6500 assemblies from 600 rpm evaporation. Not only are the spherical assemblies easily distinguished at relatively low magnification (Figure 5.9a), higher magnification (Figure 5.9b) shows the Au NPs clearly aggregated within spheres.

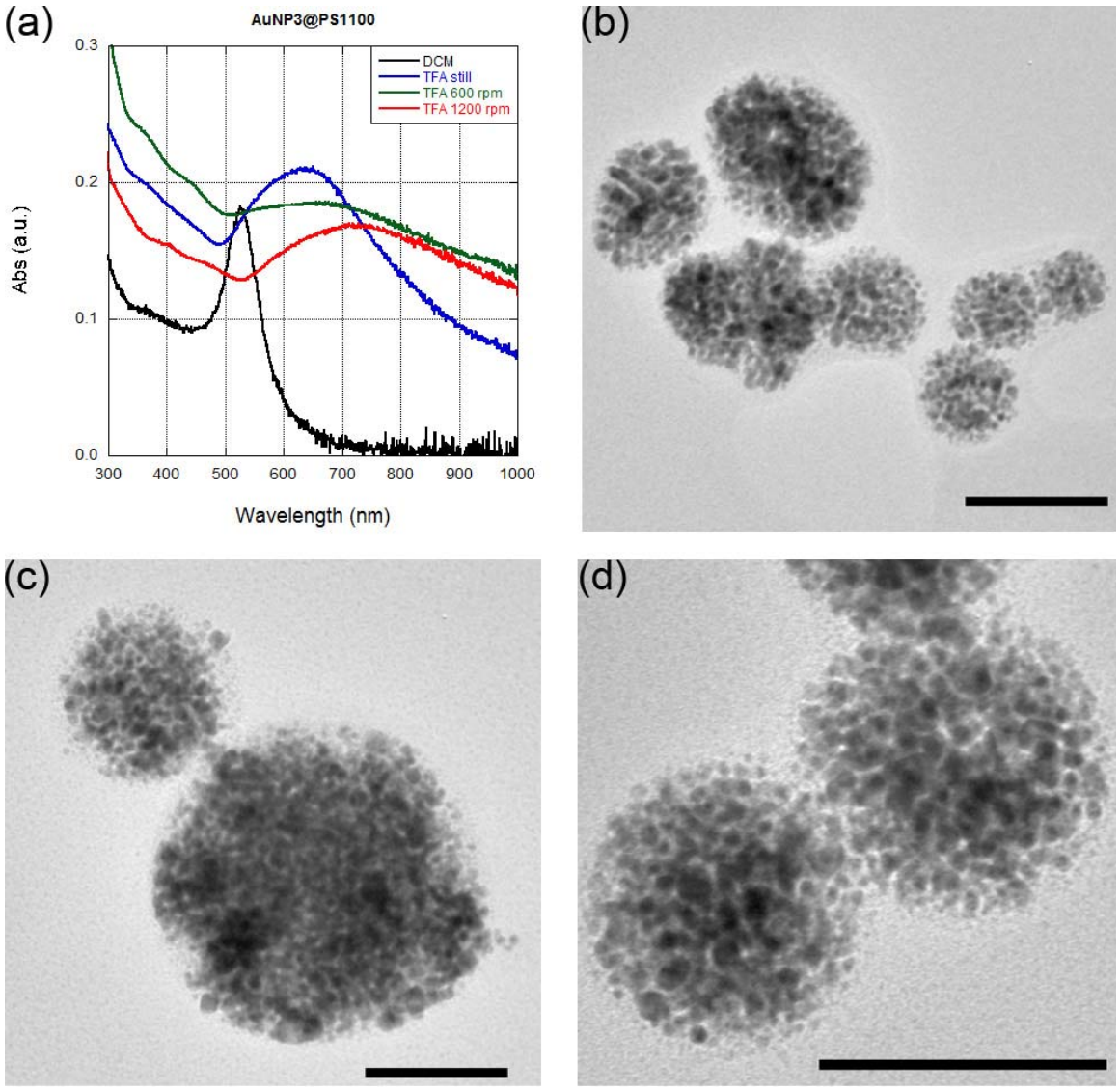

Figure 5.3 (a) UV-Vis spectra of Au NP_3@PS1100 in CH_2Cl_2 and in TFA after self-assembly by no stirring, 600 rpm stirring, and 1200 rpm stirring. Representative TEM images of the self-assembled beads of Au NP_3@PS1100 in TFA from (b) no stirring, (c) 600 rpm stirring, and (d) 1200 rpm stirring.

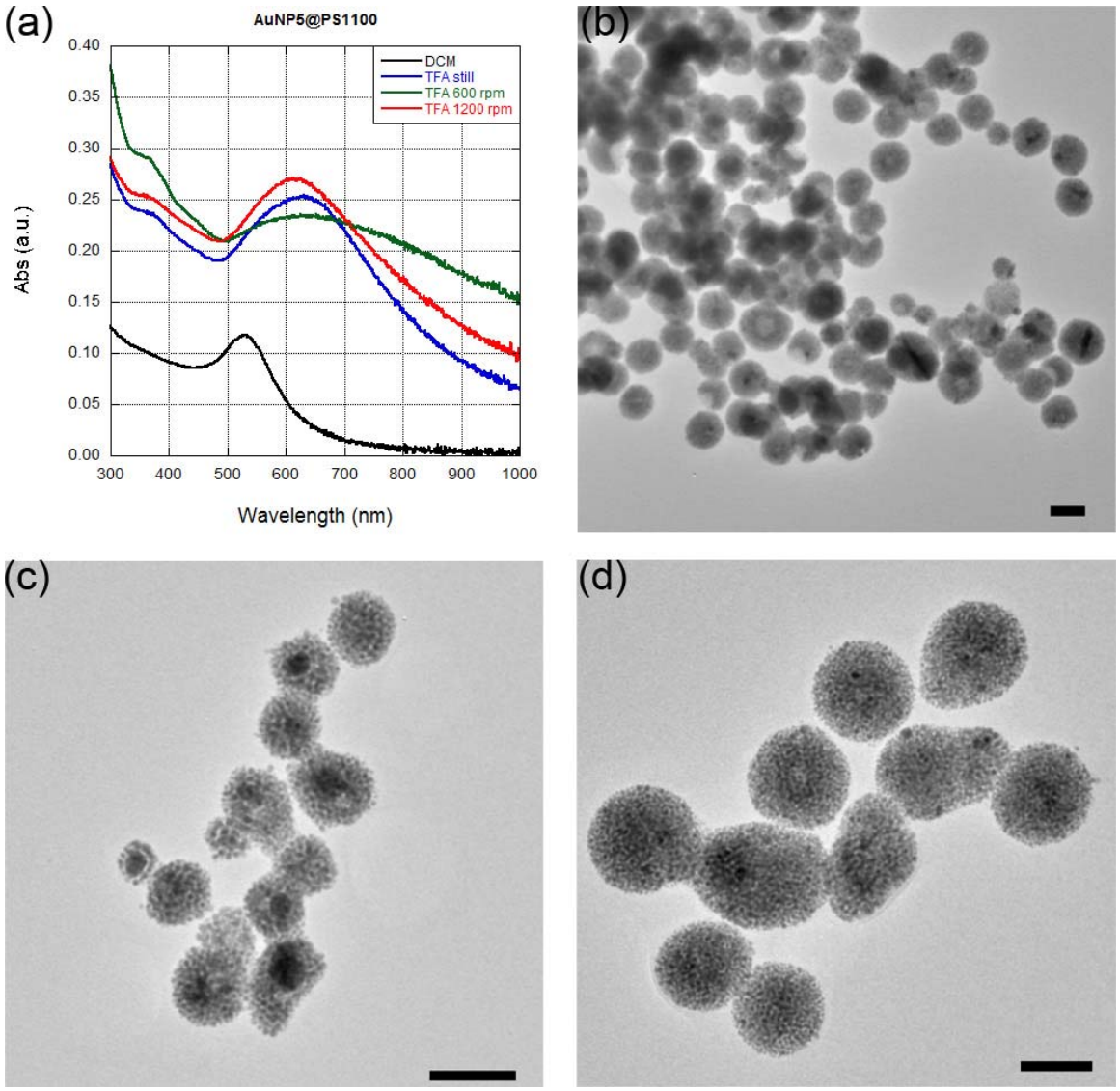

Figure 5.4 (a) UV-Vis spectra of Au NP_5@PS1100 in CH_2Cl_2 and in TFA after self-assembly by no stirring, 600 rpm stirring, and 1200 rpm stirring. Representative TEM images of the self-assembled beads of Au NP_5@PS1100 in TFA from (b) no stirring, (c) 600 rpm stirring, and (d) 1200 rpm stirring.

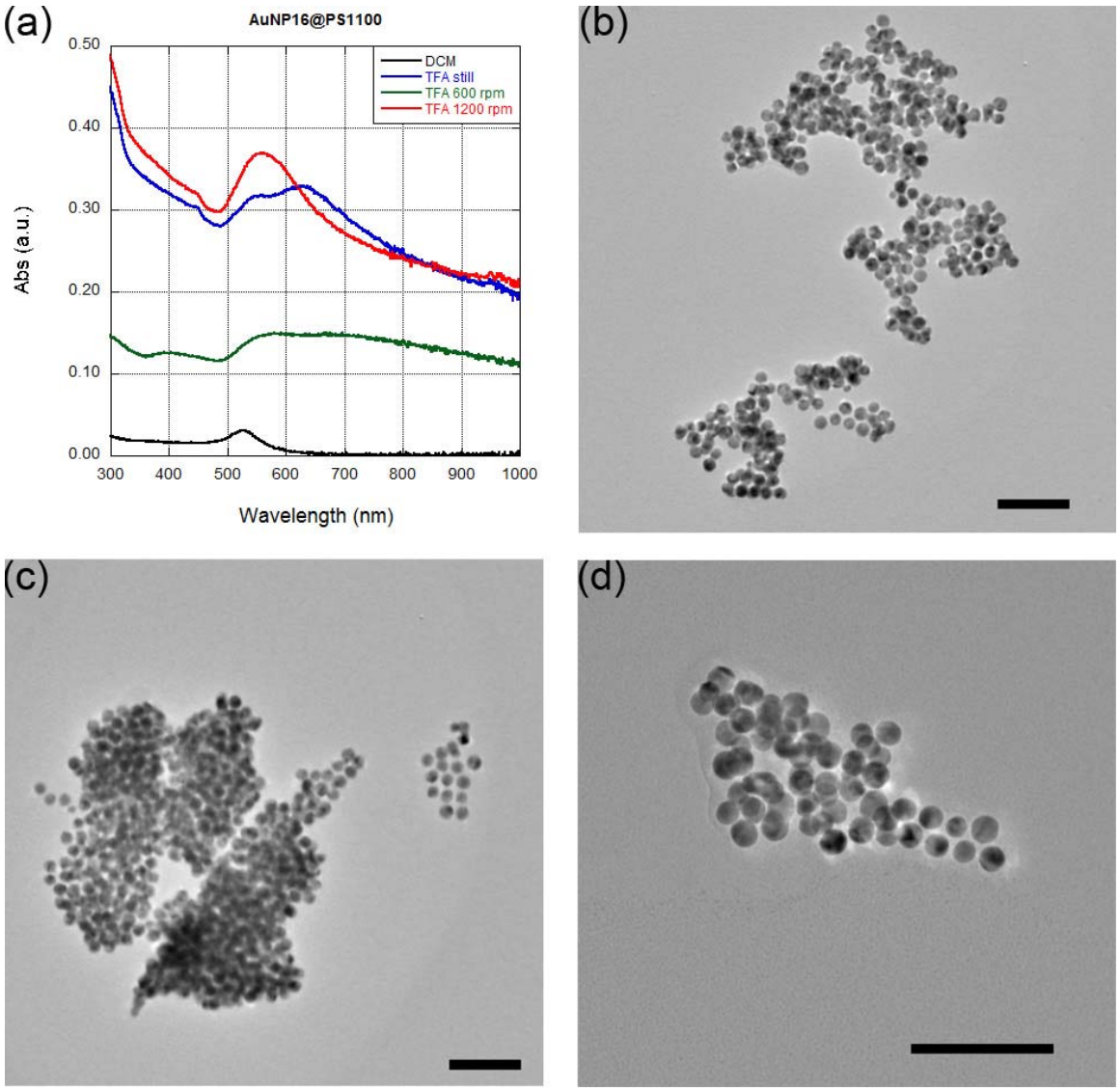

Figure 5.5 (a) UV-Vis spectra of Au NP_{16}@PS1100 in CH_2Cl_2 and in TFA after self-assembly by no stirring, 600 rpm stirring, and 1200 rpm stirring. Representative TEM images of the self-assembled beads of Au NP_{16}@PS1100 in TFA from (b) no stirring, (c) 600 rpm stirring, and (d) 1200 rpm stirring.

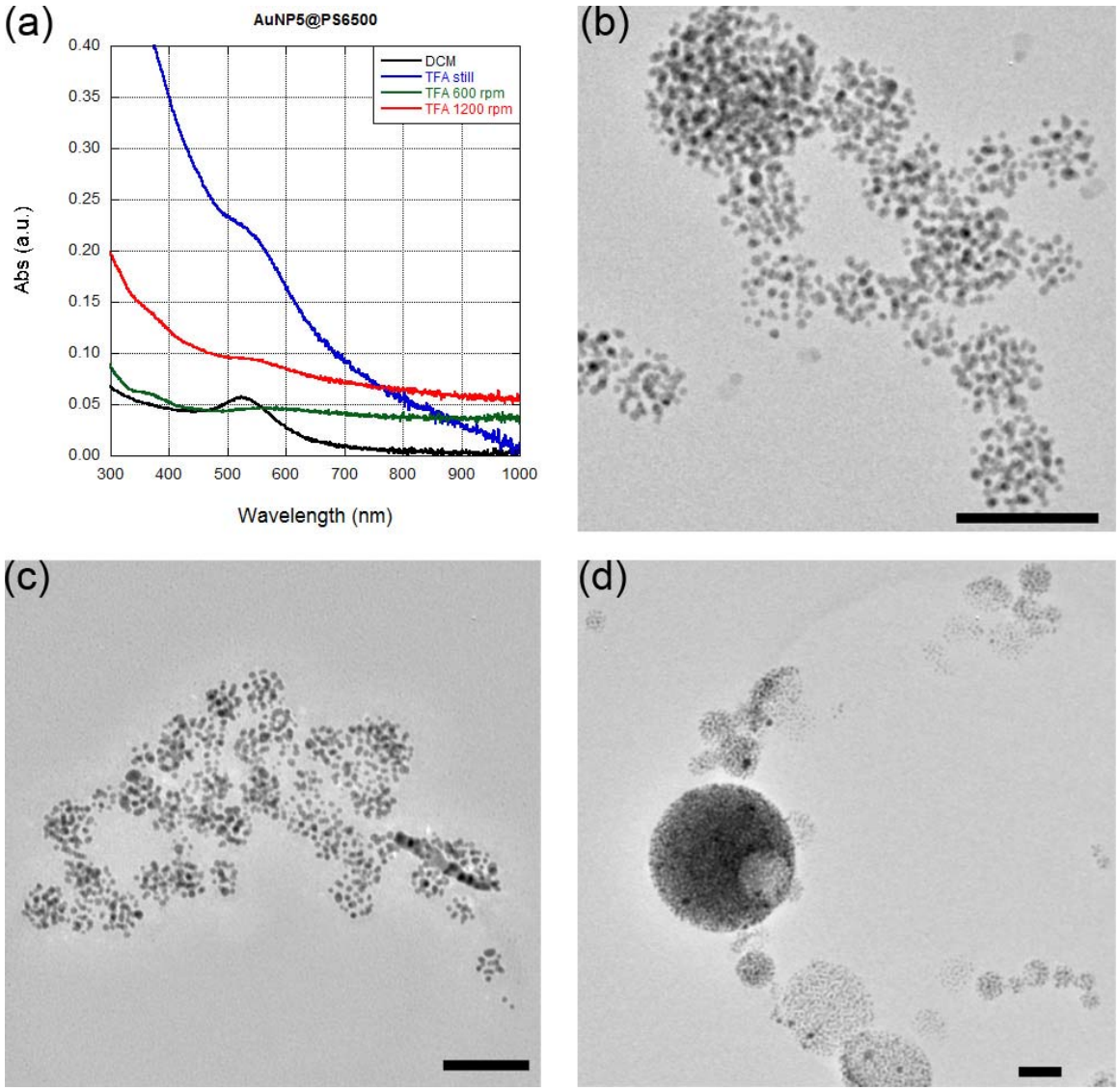

Figure 5.6 (a) UV-Vis spectra of Au NP_5@PS6500 in CH_2Cl_2 and in TFA after self-assembly by no stirring, 600 rpm stirring, and 1200 rpm stirring. Representative TEM images of the self-assembled beads of Au NP_5@PS6500 in TFA from (b) no stirring, (c) 600 rpm stirring, and (d) 1200 rpm stirring.

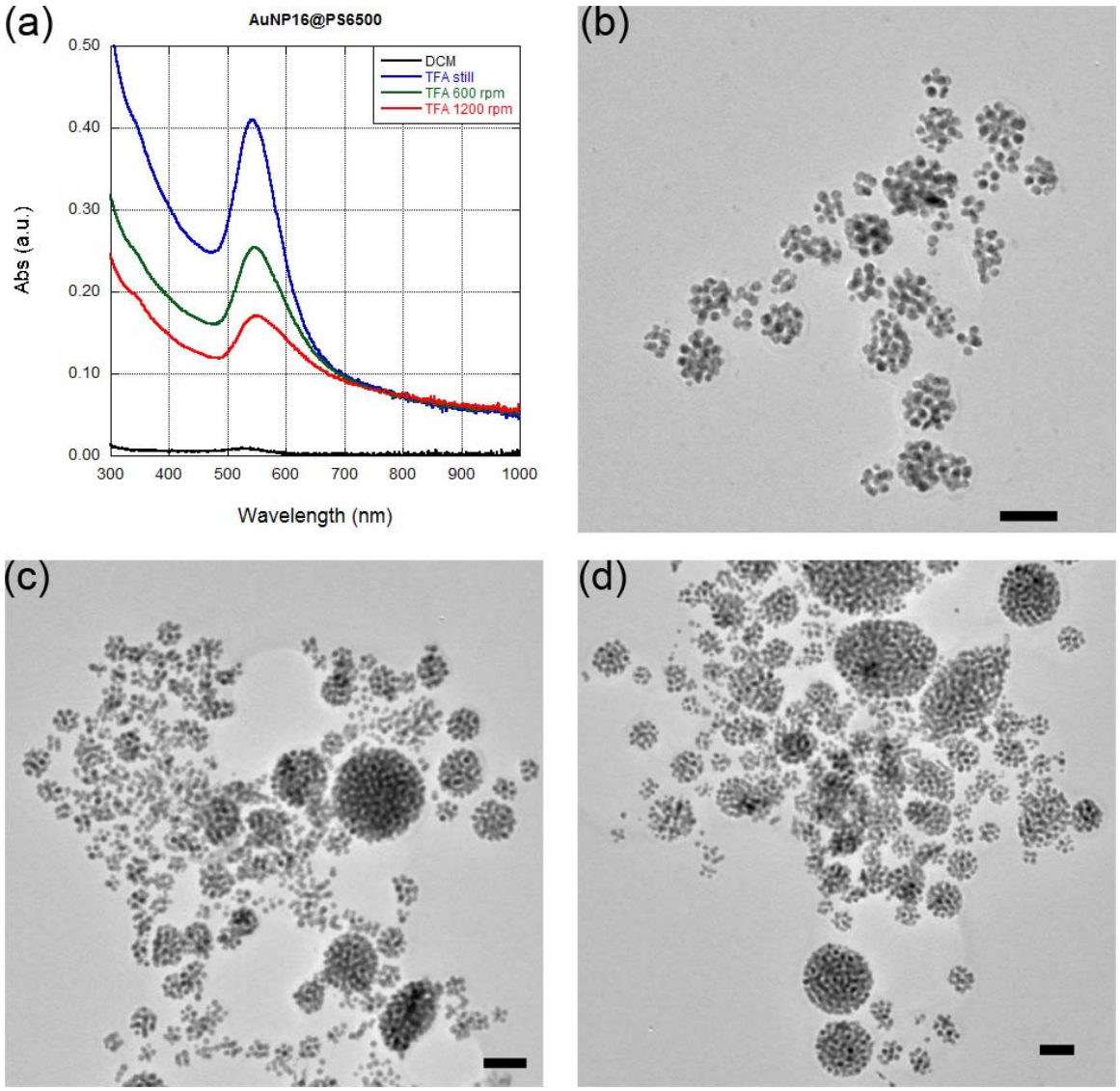

Figure 5.7 (a) UV-Vis spectra of Au NP_{16}@PS6500 in CH_2Cl_2 and in TFA after self-assembly by no stirring, 600 rpm stirring, and 1200 rpm stirring. Representative TEM images of the self-assembled beads of Au NP_{16}@PS6500 in TFA from (b) no stirring, (c) 600 rpm stirring, and (d) 1200 rpm stirring.

Table 5.1 Summary of the sizes of Au NP microbead assembly sizes from different sized Au NPs, molecular weight HS-PS, and evaporation methods. Italicized microbead sizes indicates a bimodal distribution of microbead sizes

Au NP size (nm)	**M_n HS-PS (g/mol)**	**Evaporation method**	**Microbead size (nm)**
2.5 ± 1.6	1,100	Still	70.4 ± 16.5
		600 rpm	73.9 ± 27.7
		1200 rpm	94.5 ± 19.5
5.4 ± 1.8	1,100	Still	91.0 ± 23.5
		600 rpm	82.5 ± 22.7
		1200 rpm	87.7 ± 24.0
16.0 ± 2.0	1,100	Still	N/A
		600 rpm	N/A
		1200 rpm	N/A
4.1 ± 1.5	6,500	Still	58.0 ± 15.5
		600 rpm	43.4 ± 18.7
		1200 rpm	*69.4 ± 62.4*
16.0 ± 2.0	6,500	Still	63.6 ± 22.2
		600 rpm	*61.6 ± 24.1*
		1200 rpm	*86.4 ± 41.0*

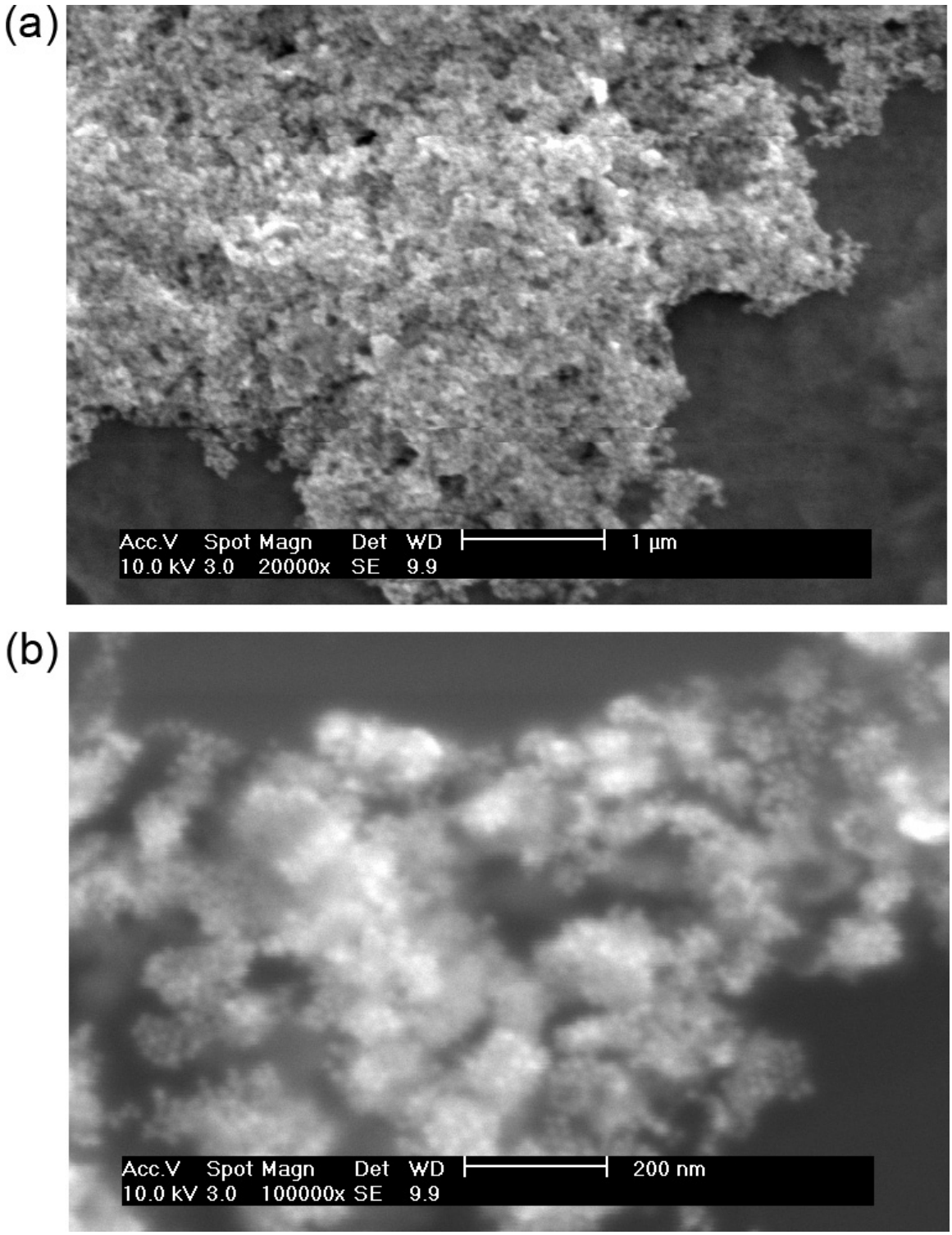

Figure 5.8 SEM images of assemblies of Au NP_{16}@PS1100 in TFA after evaporation with (a) no stirring and (b) 1200 rpm stirring.

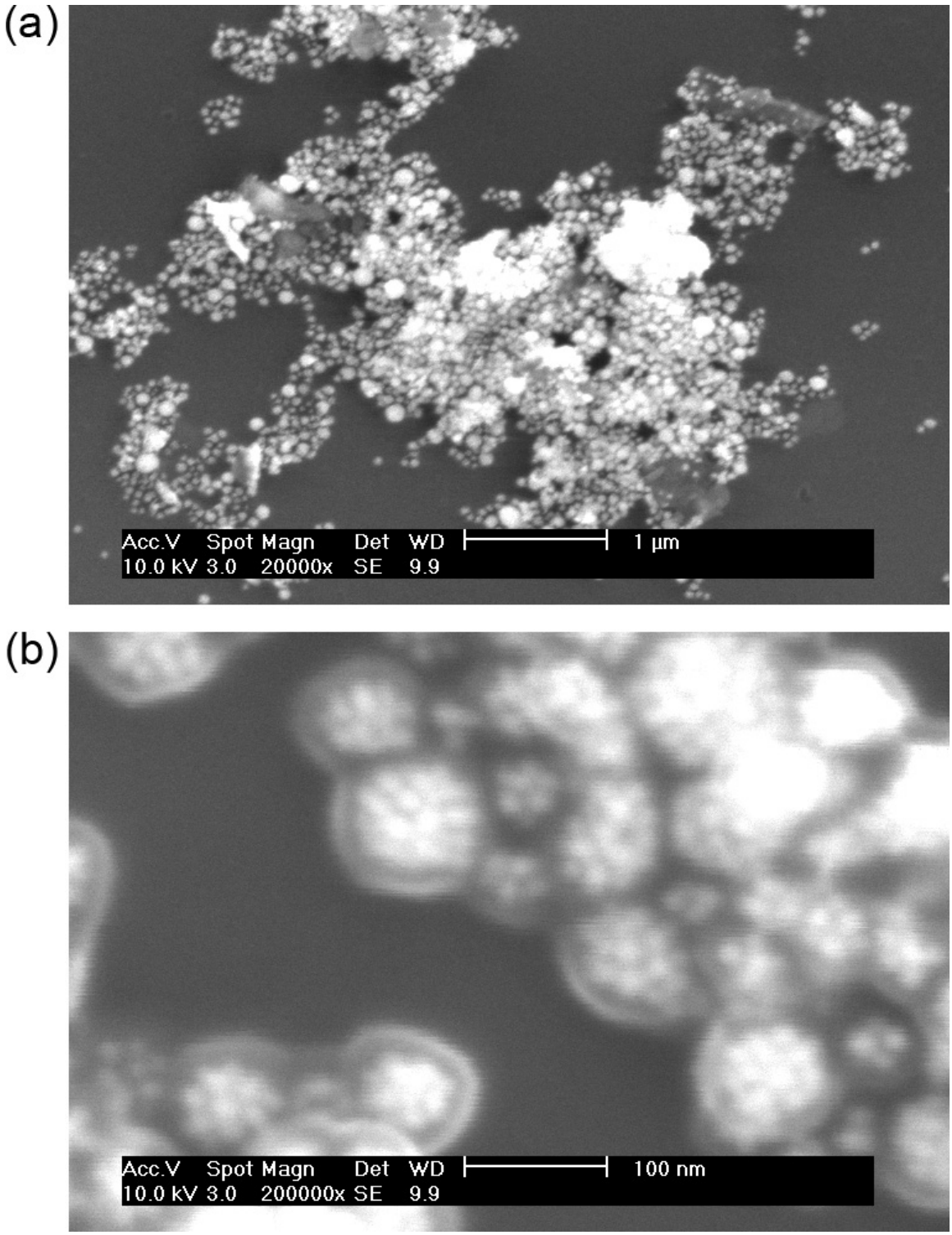

Figure 5.9 SEM images of assemblies of Au NP_{16}@PS1100 in TFA after evaporation with 600 rpm stirring. Magnifications of the images are (a) 80 kx and (b) 200kx.

5.3.3 Effects of Au NP Size on the Size of the Microbead Assembly

Different sizes of Au NPs were functionalized with the same molecular weight HS-PS in order to determine if the size of the Au NPs affects the size of the microbead assemblies. Figure 5.10 compares the sizes the microbead assemblies for different sizes of Au NPs with the same HS-PS ligand at different evaporation conditions. For the PS1100 Au NPs, the 5 nm Au NPs tend to produce larger microbeads except in the case of the 1200 rpm stirring evaporation. However, considering the substantial overlap in the size distribution for the assemblies created when stirring was used during the evaporation, this data does not show a clear trend.

Looking at the microbead sizes for the HS-PS6500 ligand, it would appear that the larger 16 nm Au NPs consistently generate slightly larger microbead assemblies. Yet, the broad size distributions show a lot of overlap for the different sized Au NPs. Thus, it would appear that the size of the Au NPs does not have a very great effect on the size of the microbead assembly.

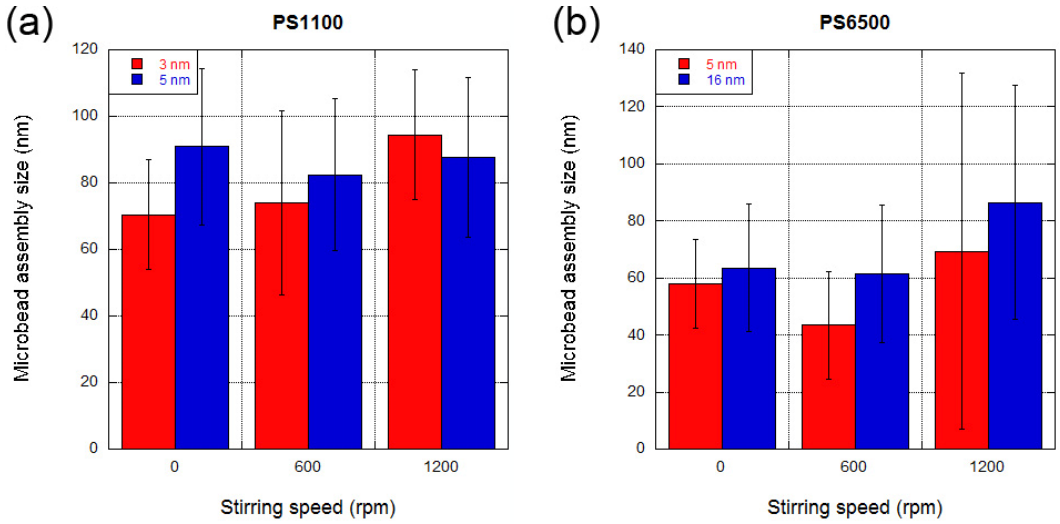

Figure 5.10 Graphical representation of the effects of the Au NP size on the size of the microbead assemblies at under different evaporation conditions and with (a) HS-PS1100 and (b) HS-PS6500 ligands.

5.3.4 How Stirring Effects the Size of the Microbead Assemblies

In order to demonstrate how the evaporation rate effects the size of the microbead assemblies, the CH_2Cl_2/TFA solution was either not stirred, or stirred with a stir bar at 600 or 1200 rpm. The 600 rpm stirring did not induce a vortex for the full 14 mL of solution, but as the volume of the solution decreased from the evaporation, a vortex was eventually generated. On the other hand, the 1200 rpm stirring generated a vortex for the 14 mL of solution. Total evaporation of the CH_2Cl_2 took ~20 hrs. when either no stirring or 600 rpm stirring was employed. The evaporation only took ~9 hrs. when 1200 rpm stirring was used.

It was believed that stirring would result in more uniform microbead assemblies due to better mixing of the solution. Figure 5.11 is a graphical representation of the various Au NP systems and the effect of the stirring speeds on the sizes of the microbead assemblies. In almost every case, the microbead assemblies generated with 1200 rpm stirring are larger than when 600 rpm stirring or no stirring was used. In the case of the Au NPs capped with a HS-PS6500 ligand, the size distribution was often bimodal, which means that there was a mix of large and small microbead assemblies. The bimodal distributions resulted in the large standard deviations for these data points. The reason that the 1200 rpm stirred samples produce such large microbead assemblies is because as the CH_2Cl_2 evaporates faster, there is a greater driving force for the Au NPs to aggregate. The agitation also increases the likelihood of two Au NPs finding each other to form an aggregate. This includes smaller Au NP aggregates fusing together to form a larger aggregate. The elliptical assemblies seen in the TEM images of the Au NP microbeads are most likely a result of two microbeads fusing into a larger microbead.

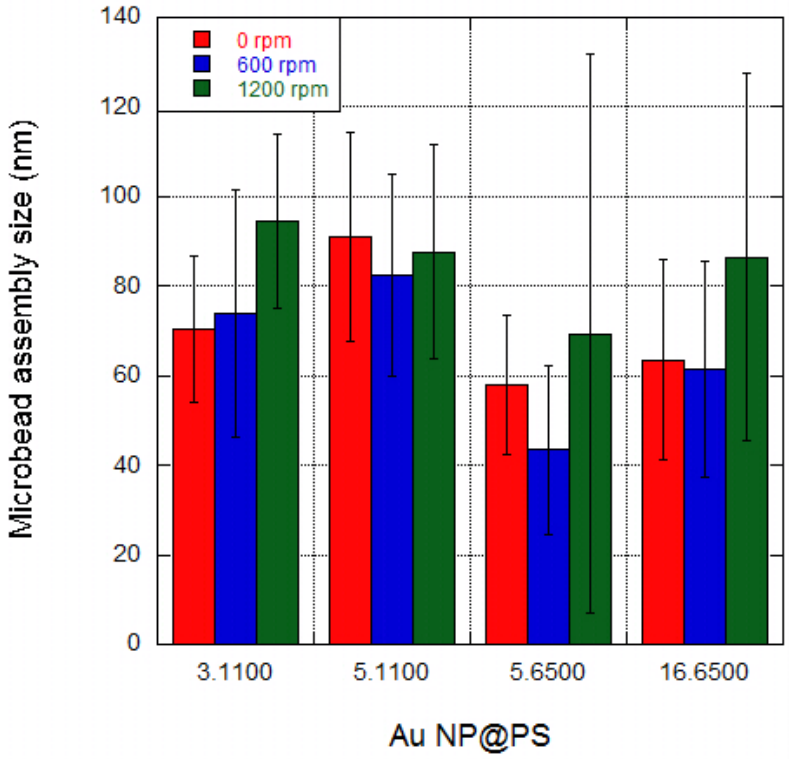

Figure 5.11 A graphical representation of the effect of the stirring speeds on the sizes of the microbead assemblies for the various Au NP systems.

A bimodal distribution of microbead assembly sizes was observed for the $AuNP_5$@PS6500 and Au NP_{16}@PS6500 samples evaporated with 1200 rpm and the Au NP_{16}@6500 sample evaporated at 600 rpm. While the increased evaporation rate for the 1200 rpm stirring partially explains the heterogeneity of the sizes, the stirring is probably most likely to blame. The stirring generates shear forces on the Au NPs and their assemblies. These forces, accompanied by the stir bar which is violently agitating the solution could cause the assemblies of the Au NPs to break apart. Thus, large assemblies may be obliterated into smaller assemblies.

The 600 rpm stirred samples and the not stirred samples resulted in fairly similar sized microbeads, except in the case of the bimodal Au NP_{16}@6500 system. The reason for the similar sizes could be that the 600 rpm stirring does not violently disrupt the

system enough in the early stages of the evaporation. In fact, the general trend is that the 600 rpm stirring resulted in slightly smaller average microbead assembly sizes, but slightly larger size variances. The reason for the slightly decreased size could be that as the evaporation proceeds, the volume of the solution decreases and the 600 rpm stirring becomes capable of more violently agitating the solution, which in turn leads to more rapid evaporation. Keeping in mind that all of the Au NP microbead assemblies precipitate out of solution, the accelerated evaporation may force the precipitation of the microbead assemblies sooner than if there was no stirring. Also, as the stirring becomes more violent, there is a greater likelihood that the Au NP assemblies may be blasted apart from the stir bar and the shear forces, which accounts for the larger standard deviations.

Lastly, the samples that were not stirred generally produced microbead assemblies with fairly narrow size distributions. Without any stirring, the evaporation is allowed to proceed at a fairly constant rate. Also, there are no shear forces or stir bar available to smash apart the Au NPs. Since evaporation without stirring is fairly calm, the microbeads are allowed to assemble slowly. Once they reach a critical size, they become insoluble and precipitate out of the solution. It would appear that evaporation without stirring is the best route to producing relatively uniform microbead assemblies. The uniformities seen for the microbeads generated without stirring are comparable with those generated using cross-linking molecules.[1-4]

5.4 Conclusions

The spherical self-assembly of large quantities of Au NPs was prepared by using the good-solvent evaporation process. Au NPs were synthesized by one-phase or two-

phase method with thiol-end functionalized polystyrene (PS-SH) as a passivation layer. The resulting PS-coated Au NPs were dissolved in CH_2Cl_2/TFA mixture solvent (1:1, v:v) and the spherical beads could be formed after the complete evaporation of volatile CH_2Cl_2 in the solution.

It was found that the microbead assemblies of Au NPs were generally smaller for larger molecular weight HS-PS. Also, larger Au NPs generally yielded larger microbead assemblies. Although it was thought that stirring would result in more uniform microbead assembly sizes, stirring actually resulted in less uniform sizes. Also, rapid stirring accelerated the evaporation of the solution, which led to greater microbead sizes and greater size variations. By allowing the evaporation to proceed without agitation, relatively uniform microbead assemblies were generated.

5.5 References

1. Hussain, I.; Wang, Z. X.; Cooper, A. I.; Brust, M., Formation of spherical nanostructures by the controlled aggregation of gold colloids. *Langmuir* **2006,** *22* (7), 2938-2941.
2. Maye, M. M.; Chun, S. C.; Han, L.; Rabinovich, D.; Zhong, C. J., Novel spherical assembly of gold nanoparticles mediated by a tetradentate thioether. *J. Am. Chem. Soc.* **2002,** *124* (18), 4958-4959.
3. Maye, M. M.; Lim, I. I. S.; Luo, J.; Rab, Z.; Rabinovich, D.; Liu, T. B.; Zhong, C. J., Mediator-template assembly of nanoparticles. *J. Am. Chem. Soc.* **2005,** *127* (5), 1519-1529.
4. Maye, M. M.; Luo, J.; Lim, I. I. S.; Han, L.; Kariuki, N. N.; Rabinovich, D.; Liu, T. B.; Zhong, C. J., Size-controlled assembly of gold nanoparticles induced by a tridentate thioether ligand. *J. Am. Chem. Soc.* **2003,** *125* (33), 9906-9907.
5. Hussain, I.; Wang, Z.; Cooper, A. I.; Brust, M., Formation of Spherical Nanostructures by the Controlled Aggregation of Gold Colloids. *Langmuir* **2006,** *22* (7), 2938-2941.
6. Higuchi, T.; Yabu, H.; Shimomura, M., Simple preparation of hemispherical polystyrene particles. *Colloid Surf. A-Physicochem. Eng. Asp.* **2006,** *284*, 250-253.
7. Yabu, H.; Higuchi, T.; Ijiro, K.; Shimomura, M., Spontaneous formation of polymer nanoparticles by good-solvent evaporation as a nonequilibrium process. *Chaos* **2005,** *15* (4).
8. Yabu, H.; Higuchi, T.; Shimomura, M., Unique phase-separation structures of block-copolymer nanoparticles. *Adv. Mater.* **2005,** *17* (17), 2062-+.
9. Fava, D.; Nie, Z.; Winnik, M. A.; Kumacheva, E., Evolution of Self-Assembled Structures of Polymer-Terminated Gold Nanorods in Selective Solvents. *Adv. Mater.* **2008,** *20* (22), 4318-4322.
10. Nie, Z. H.; Fava, D.; Kumacheva, E.; Zou, S.; Walker, G. C.; Rubinstein, M., Self-assembly of metal-polymer analogues of amphiphilic triblock copolymers. *Nat. Mater.* **2007,** *6* (8), 609-614.
11. Nie, Z. H.; Fava, D.; Rubinstein, M.; Kumacheva, E., "Supramolecular" assembly of gold nanorods end-terminated with polymer "Pom-Poms": Effect of pom-pom structure on the association modes. *J. Am. Chem. Soc.* **2008,** *130* (11), 3683-3689.
12. Yee, C. K.; Jordan, R.; Ulman, A.; White, H.; King, A.; Rafailovich, M.; Sokolov, J., Novel One-Phase Synthesis of Thiol-Functionalized Gold, Palladium, and Iridium Nanoparticles Using Superhydride. *Langmuir* **1999,** *15* (10), 3486-3491.
13. Corbierre, M. K.; Cameron, N. S.; Lennox, R. B., Polymer-stabilized gold nanoparticles with high grafting densities. *Langmuir* **2004,** *20* (7), 2867-2873.
14. Brust, M.; Walker, M.; Bethell, D.; Schiffrin, D. J.; Whyman, R., SYNTHESIS OF THIOL-DERIVATIZED GOLD NANOPARTICLES IN A 2-PHASE LIQUID-LIQUID SYSTEM. *J. Chem. Soc.-Chem. Commun.* **1994,** (7), 801-802.
15. Hiramatsu, H.; Osterloh, F. E., A simple large-scale synthesis of nearly monodisperse gold and silver nanoparticles with adjustable sizes and with exchangeable surfactants. *Chem. Mat.* **2004,** *16* (13), 2509-2511.

Chapter 6

Block Copolymer Templates for Self-Assembling Gold Nanoparticles

6.1 Introduction

Block copolymers are polymers that are composed of two different types of monomers which make up two separate blocks. Based on the fraction of each block, f_x, block copolymers can self-assemble into thermodynamically favorable configurations, as seen in Figure 6.1.[1]

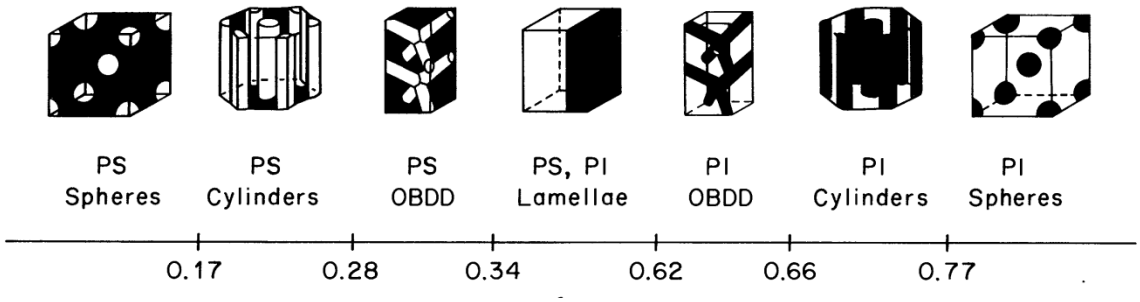

Figure 6.1 Bulk configurations of a poly(styrene)-b-poly(isoprene) block copolymer for different fractions of poly(styrene). Image recreated from Bates.[1]

Poly(styrene)-b-poly(4-vinyl pyridine) (PS-PVP) is a common block copolymer that has been heavily researched.[2-6] The poly(styrene) (PS) block is hydrophobic, while the poly(4-vinyl pyridine) (PVP) block is hydrophilic. The chemical structure of PS and PVP monomers are shown in Figure 6.2. Based on the solvent choice, it is possible to form micelles of the PS-PVP in solution with one block as the core and the other as a

pseudoligand.[5, 6] Furthermore, the solvent choice can affect the morphology of the block copolymer film.[6]

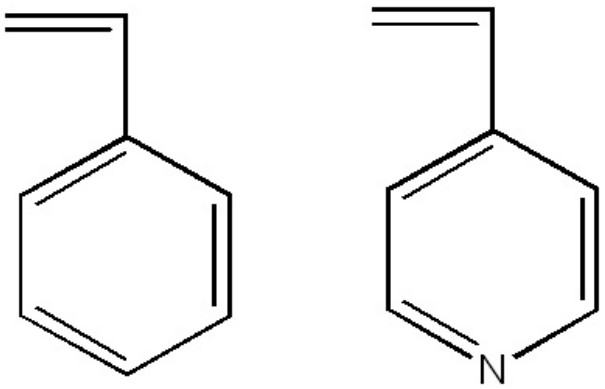

Figure 6.2 Chemical structures of the (left) PS monomer and the (right) PVP monomer.

Block copolymers are generally spin-cast on substrates. The morphology of the resulting configuration is dependent upon the substrate. Figure 6.3 illustrates the morphologies of PS-PVP (f_{PS} = 0.51) thin-films spin-cast on different substrates. The pattern observed for the mica substrate shows spheres of PS on top of PVP due to the strong attraction and repulsion to the mica of the PVP and PS, respectively. The interaction between the Si and the PVP is not as strong as for the mica, thus a more random pattern is observed. In the case of the graphite substrate, the PS wets the non-polar surface with random PVP blocks protruding on the surface. Furthermore, the morphology of the block copolymer film can be altered by using solvent annealing to selectively bring one block to the surface of the film.[3]

The bulk lamellar thickness, L, is the film thickness for which the bulk morphology repeats, as illustrated in Figure 6.4. For film thicknesses below L, the substrate effects dominate the morphology. At film thicknesses above L, the fractions of the blocks define the bulk morphology.[4]

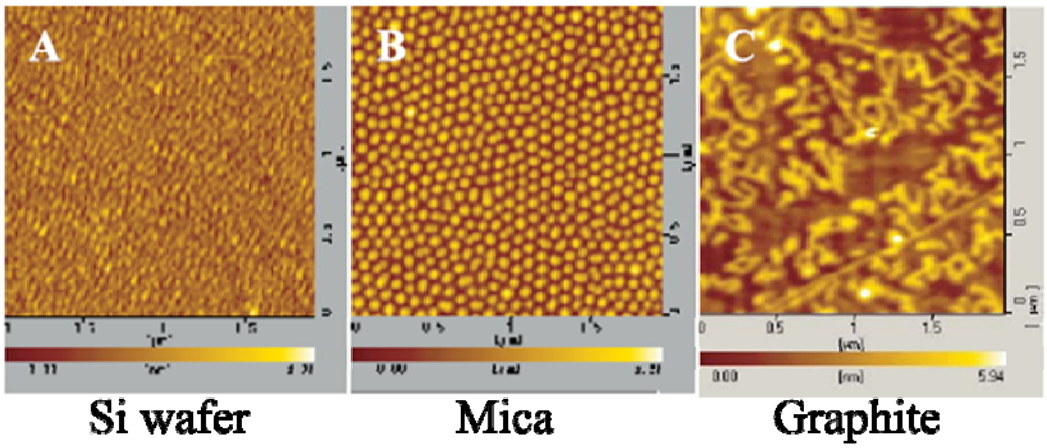

Figure 6.3 AFM images of the surface of thin films of PS-PVP spin cast on different substrates. Image recreated from Zhao.[4]

PVP has the ability to be quaternized. This means that the nitrogen in the pyridine ring bonds to an alkyl chain, and develops a permanent, positive charge. Bromoalkanes are commonly used to quaternize PVP and dibromoalkens can be used to both quaternize and cross-link PVP.[7-11] The bromide ion serves to counter the charge on the nitrogen. Interestingly, quaternized PVP can be used as an anti-microbial film.[12]

Figure 6.4 Illustration of the bulk lamellar length for a PS-PVP (f_{PS} = 0.51) film on mica. Image reproduced from Zhao.[4]

Since the size of the block copolymer domains are determined by the length of the block, it is possible to tune the sizes of the block copolymer features. Unlike lithographic methods which are generally limited by the size of the incident radiation, block copolymers can be used to generate features that are only a few nanometers in size. Thus, quaternized PS-PVP was used as a chemical template for the self-assembly of Au NPs via electrostatics with smaller feature sizes than were possible with EBL.

6.2 Experimental

Polystyrene-block-poly(4-vinylpyridine) (PS-PVP, $M_{n,\,PS}$ = 44,000 g/mol, $M_{n,\,PVP}$ = 4,400 g/mol, M_w/M_n = 1.09) was obtained from Polymer Source, Inc. All other chemical were from Sigma Aldrich and used as received.

6.2.1 Preparing PS-PVP Films

Solutions of PS-PVP in toluene at concentrations of 0.75, 1.10, 1.15, 1.20, 1.50 and 1.75 wt% were spin-cast onto clean 1 cm^2 pieces of Si wafer at 3,800 rpm for 30 s. Prior to use, Si wafers were cleaned by sonication in a 50/50 (v/v) solution of acetone and IPA, air dried, and hydroxylated by sonication in nitric acid for 10 min. All solutions were filtered through a 0.45 μm PTFE filter prior to spin-casting. At least three samples were prepared for each concentration of PS-PVP. After casting, samples were dried under vacuum overnight.

Annealing for 15 hours under toluene vapor, followed by immersion in MeOH for five hours was performed to allow the film to rearrange into the desired microstructure

and to expose the PVP regions, respectively. Samples were then dried overnight under vacuum.

6.2.2 Quaternization of PVP

Quaternization of the PVP domains with 1,4-dibromobutane was performed under an N_2 atmosphere at 110°C for 24 hours.[14] Following quaternization, samples were immersed in methanol to remove excess 1,4-dibromobutane. Samples were then dried overnight under vacuum.

6.2.3 Au NP synthesis

5 nm Au NPs were prepared by the reduction of gold salt using $NaBH_4$.[13] 20 mL of an aqueous solution of 0.25 mM $HAuCl_4$ and 25 mM trisoduim citrate was prepared. Next, 0.6 mL of ice-cold 0.1 M $NaBH_4$ was added to the solution under stirring. Almost immediately, the solution turned a pinkish color, indicating the formation of Au NPs.

6.2.4 Characterization

A J.A. Woollam Co., Inc multi-wavelength ellipsometer (control module EC110) equipped with a Xenon 75 W light source was used to measure the thickness of the PS-PVP film. The surface morphology of the thin films was characterized using a Nikon Optiphot optical microscope in reflective mode and a Nanoscope IIIa AFM (Veeco) in tapping mode.

The absorbance spectrum of the Au NPs was characterized via a Cary 50 Bio UV-Visible spectrophotometer (Varian) and the size was confirmed by TEM on a JEOL 3011 300 keV microscope.

6.3 Results and Discussion

6.3.1 PS-PVP thin film preparation

The PS-PVP thin films were prepared and the thickness was measured using ellipsometry. Four samples each of 0.75, 1.10, 1.20, 1.50 and 1.75 wt% PS-PVP were prepared, and three samples of 1.15 wt% PS-PVP were prepared. In order to make an accurate concentration, the polymer was weighed out in a vial and the corresponding volume of toluene was added to the vial with a micropipette. Table 6.1 lists the average thicknesses of the films after casting. The deviation of the film thickness was no more than 0.87 nm for any group of samples. The film thickness follows a linearly increasing trend with concentration, as seen in Figure 6.5.

Using the correlation curve, a sample with a predictable thickness was created. Two methods were used to determine the ideal thickness: ellipsometry measurement of the thickness of a donated sample with the correct microstructure and AFM image measurements of the periodicity of the surface features (domains) on a sample. The PS-PVP film sample provided by Dr. Ho-Cheol Kim from IBM ($M_{n,\,PS}$ = 35,500 g/mol, $M_{n,\,PVP}$ = 3,600 g/mol) had a thickness of 50.87 ± 1.67 nm, and the desired microstructure is present, as seen in Figure 6.6. The polymer weight fraction (f_{PVP}= 0.092) corresponds to a body centered cubic bulk film morphology with PVP spheres. The periodicity of the

surface domains, L, was measured to be about 24 nm, meaning that the total film thickness is about 2L. Since the thickness was very close to an integer multiple of the periodicity, the surface morphology matches the bulk morphology, and PVP domains are present.

Table 6.1 The thicknesses of spin-cast PS-PVP films before and after annealing with toluene vapor

Concentration (wt% PS-PVP)	Pre-annealed Thickness (nm)	Post-annealed Thickness (nm)	Change in Thickness (nm)
1.75	62.93 ± 0.24	-	-
1.50	53.04 ± 0.16	-	-
1.20	35.94 ± 0.09	-	-
1.15	38.34 ± 0.11	40.29 ± 0.12	1.95
1.10	35.53 ± 0.08	36.21 ± 0.09	0.68
0.75	27.92 ± 0.16	-	-
0.50	23.78 ± 0.30	21.87 ± 0.40	-1.91
0.25	17.29 ± 0.87	14.59 ± 1.32	-2.70
0.38	14.60 ± 0.55	15.38 ± 0.75	0.78

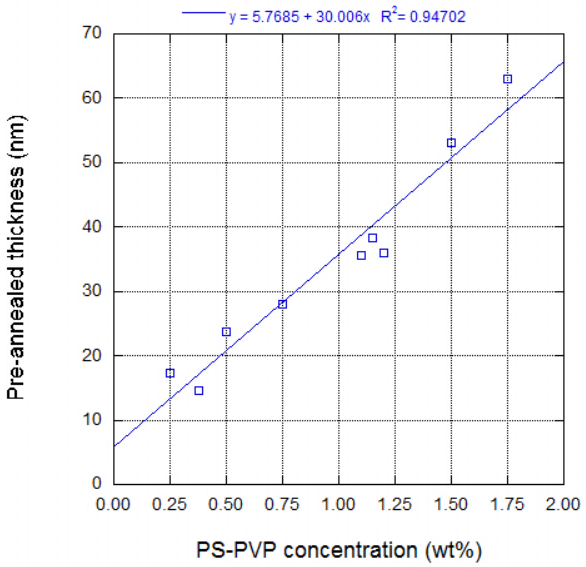

Figure 6.5 Correlation curve between the concentration of the polymer in toluene and the thickness of the polymer film.

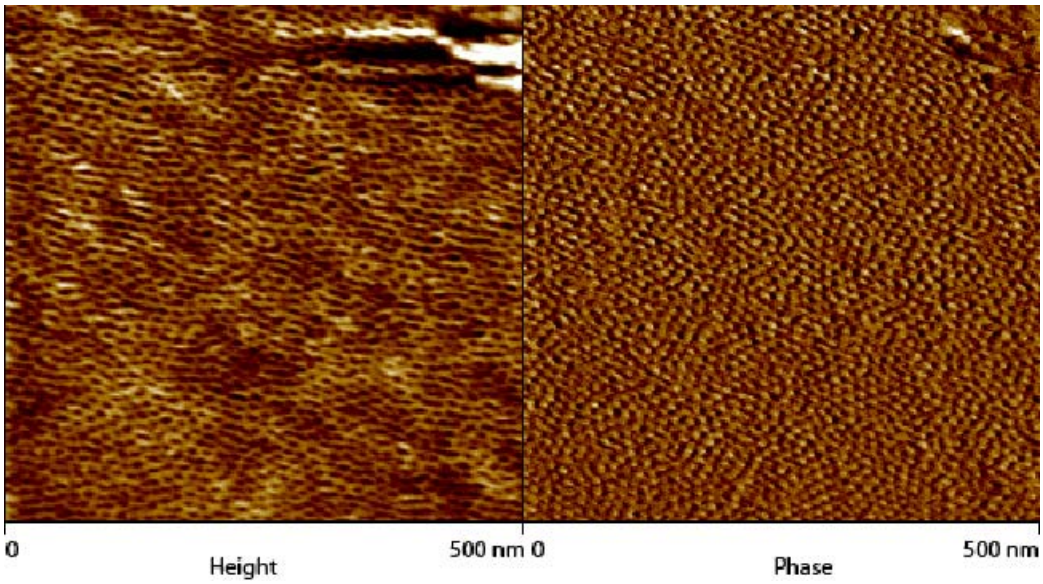

Figure 6.6 Height and phase AFM images of a PS-PVP film prepared by Dr. Ho-Cheol Kim showing a hexagonal array of PVP domains.

AFM image measurements of the PVP domain periodicities of the prepared samples yielded dissimilar numbers. Periodicities of 24 ± 3 nm and 35 ± 7 nm were measured for the 1.15 wt% and the 1.50 wt% samples, respectively. For the polymer used to create the thin films, $f_{PVP} = 0.124$, which corresponds to a bulk morphology of PVP spheres, like the sample provided by Dr. Kim. However, the domain periodicity should depend only on the lengths of the polymer blocks, and therefore should be the same for any thickness. The difference in the periodicity measurements for each thickness is difficult to explain. A more accurate measurement of the domain periodicity can be obtained by making more measurements on more AFM images of different samples. The most important thing to notice is that although the periodicity is not consistent across the samples, the surface morphology exhibits nano-scaled PVP domains. Ellipsometry indicated that the 1.50 wt% sample was 53 ± 0.2 nm thick and the 1.15 wt% sample was

38 ± 0.1 nm thick; both are relatively close to integer multiples of the values predicted by the two methods, and are considered in greater detail.

The preparation of a PS-PVP film for nanoparticle adsorption and assembly requires careful attention to the thickness of the film in order to achieve the correct microstructure. The microstructures of the samples were observed by AFM. The microstructure of the 1.15 wt% film is seen in Figure 6.7. The AFM images of the PS-PVP samples indicated the formation of the correct microstructure; there were small domains that may be used as a pattern for nanoparticle assembly. They both show PVP domains of about 20 nm in diameter. It is difficult to interpret the AFM phase image in order to tell whether the PS or the PVP is the raised or lowered domain. The PVP should appear raised on the phase image because it has a higher T_g than PS, and thus is stiffer.

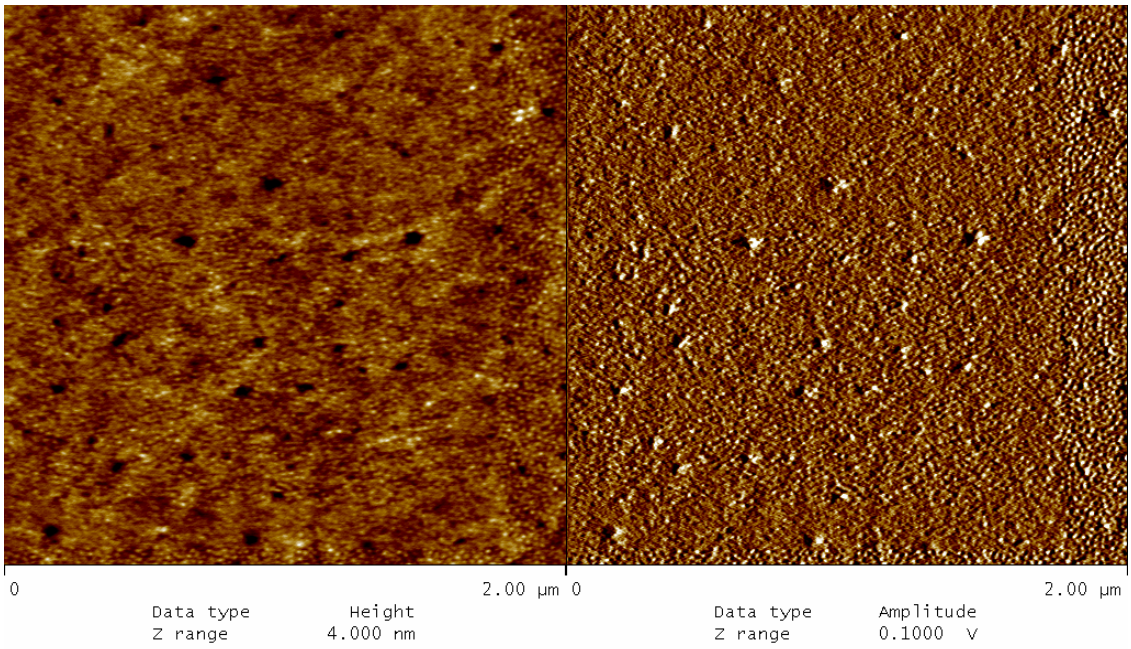

Figure 6.7 Height (left) and Phase (right) AFM images of 1.15 wt% PS-PVP in toluene solution as cast onto Si. The height image indicates the presence of small (~20 nm diameter) raised domains.

The film thickness measurements by ellipsometry are fairly accurate, but the AFM images are inconclusive. The desired microstructure has spherical PVP domains in a PS matrix. While the AFM images confirmed the presence of domains of the correct size, they did not provide detailed enough resolution to confirm that the domains are PVP. Identifying the species of the domain was almost a matter of perspective since no clear images at high enough magnifications could be obtained. The AFM images were limited by the fact that the tip radius is large, and the AFM scanner is meant for larger regions. This may all be ameliorated by using smaller tips and a scanner designed for smaller regions. Most of the samples showed that there are nano-domains at the surface, but it was hard to tell whether or not the domains were the correct species. Re-scanning these samples under more suitable conditions should reveal the true nature of the sample.

The 1.10, 1.15, 1.20, 1.50, and 1.75 wt% PS-PVP samples were annealed, and the thickness changed by less than 3 nm for any concentration, as seen in Table 6.1. The microstructure became more defined, as seen in Figure 6.8. The films were in a high energy state directly after casting, which was relieved through annealing. After annealing the features became more pronounced and the film was closer to an equilibrium state.

The macroscopic surface of the samples was uneven, but the microstructure still exhibited nano-scale domains. The unevenness in the surface is likely a result of the thickness of the film not being a perfect integer multiple of the domain periodicity. This causes the phases to separate and the surface reconstructs roughly into islands and hairline features in order to minimize its free energy.

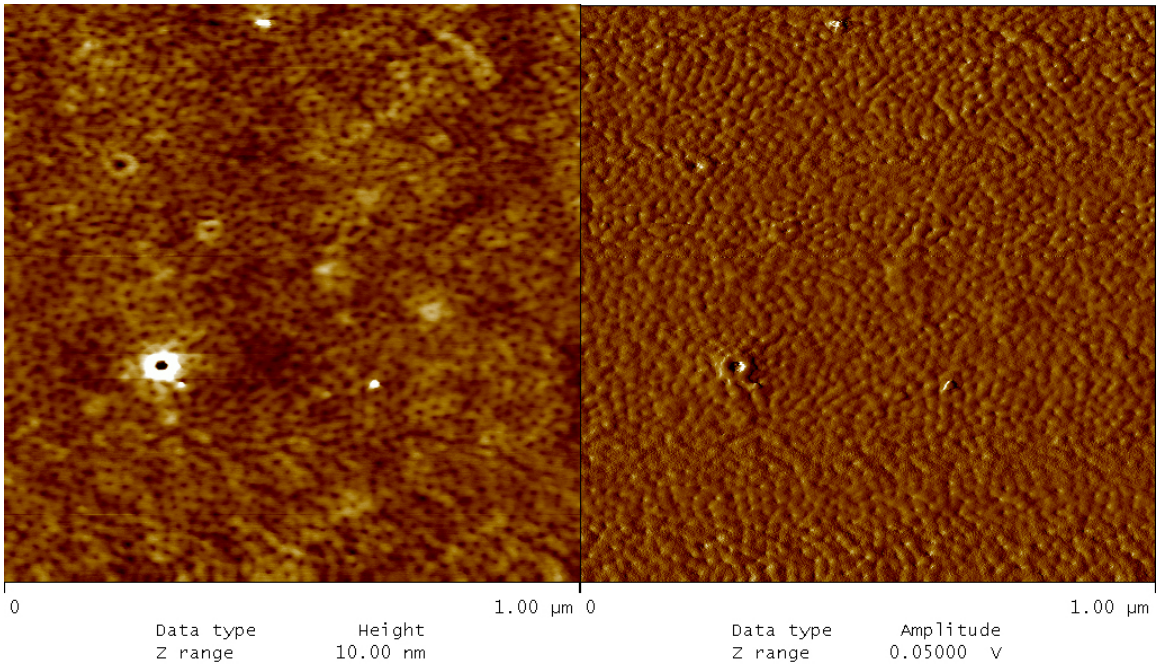

Figure 6.8 AFM (a) height and (b) phase images of the 1.15 wt% PS-PVP film after annealing with toluene.

6.3.2 Quaternization of the PVP domains

The next step in film preparation was the quaternization. 1,4-dibromobutane was used because in addition to giving the pyridine a positive charge it also cross-links the PVP groups, which should reduce swelling that may occur in aqueous solvents.[11] The 1.15 wt% sample was quaternized, and the surface was characterized using AFM, as seen in Figure 6.9. The surface appears to be disfigured and the desired nano-domains appear to no longer be present. However this may have been a result of a dirty AFM tip or the previously mentioned poor imaging conditions. More likely, though, the PVP domains have swelled after the quaternization due to the additional akyl chain disrupting the packing of the PVP domains.

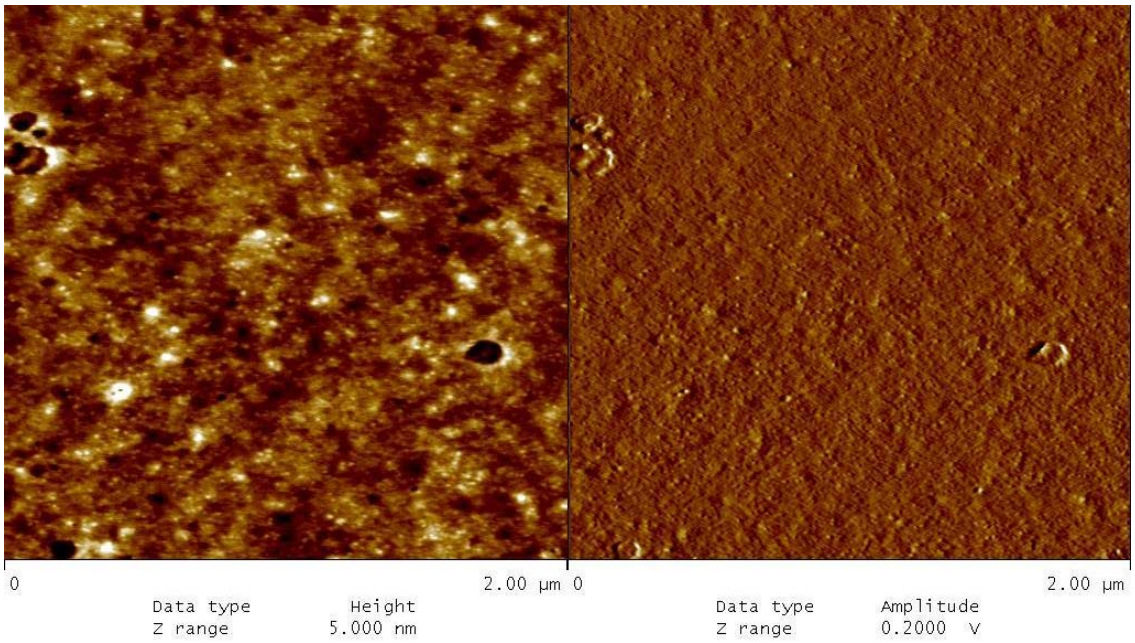

Figure 6.9 AFM (left) height and (right) phase images of the 1.15 wt% PS-PVP film after annealing and quaternization with 1,4-dibromobutane.

After the Au NPs were prepared, the quaternized 1.15 wt% sample was dipped into the aqueous, citrate-capped Au NP solution, but the surface morphology appears to have changed even more than before, as seen in Figure 6.10. A possibility is that the PVP in the film swelled in the presence of water, which would imply that the cross-linking did not succeed as was intended. Also, no Au NPs appeared to remain on the surface. However, it is possible that the Au NPs were too small to be perceived by the relatively large AFM tip. Carbon nanotube coated AFM tips or scanning transmission electron microscopy (STEM) may be more useful in imaging the small Au NPs.

The sample prepared by Ho-Choel Kim was quaternized using 1-bromobutane. After quaternization, the PVP domains appeared raised, relative to the PS matrix (Figure 6.11). This was most likely due to swelling of the PVP domains and increased volume of the PVP domains due to the interference in the packing because of the additional alkyl

chain. The hexagonal arrays are still present, which indicates that the PVP is still present at the surface.

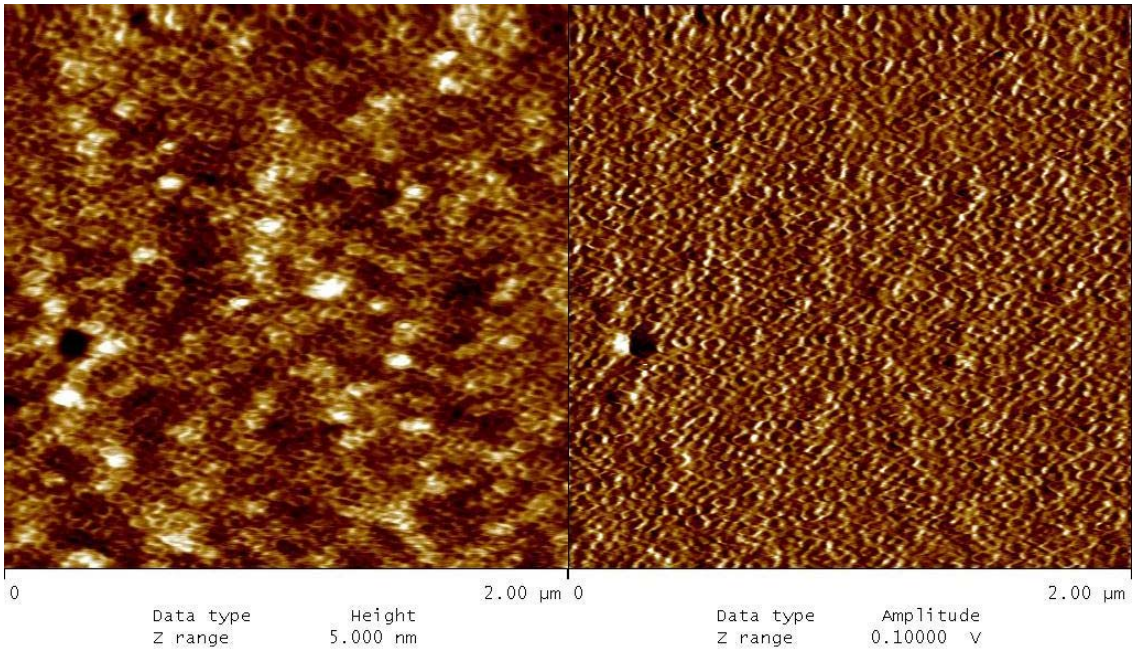

Figure 6.10 AFM height (left) and phase (right) images of the 1.15 wt% quaternized sample after immersion in a citrate-capped Au NP solution.

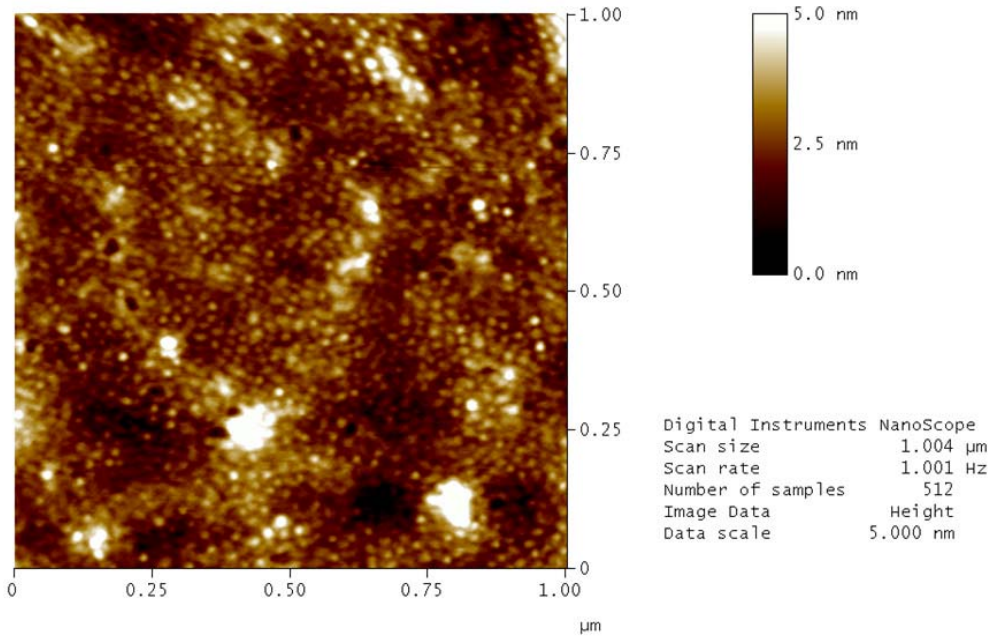

Figure 6.11 AFM height image of the PS-PVP film prepared by Dr. Ho-Cheol Kim after quaternization.

The quaternized sample was then immersed in the Au NP solution. The AFM images are seen in Figure 6.12. There appear to be many spherical areas that are much harder and more raised than the rest of the surface. These areas also appear to be hexagonal in conformation, which suggests that they are the PVP regions. It is believed that the additional hardness which is detected in the phase image corresponds to Au NPs on the PVP regions. However, closer analysis of these areas showed that the spheres were ~20 wide and ~ 7nm higher than the surface. Since the spherical dimensions were similar to those observed of the PVP domains of the film before the quaternization, it is safe to conclude that the spheres are the PVP domains. The increased height could either be due to swelling or the presence of Au NPs. After the quaternization, the swollen spheres had a height of ~1 nm, which means that the additional height may be from the presence of Au NPs. Since the Au NPs are so small, it is impossible to resolve them with the AFM. SEM was attempted to visualize the Au NPs, but the Au NPs were too small to be resolved with the SEM. Again, a carbon nanotube coated AFM tip or STEM could be used to better visualize the Au NPs.

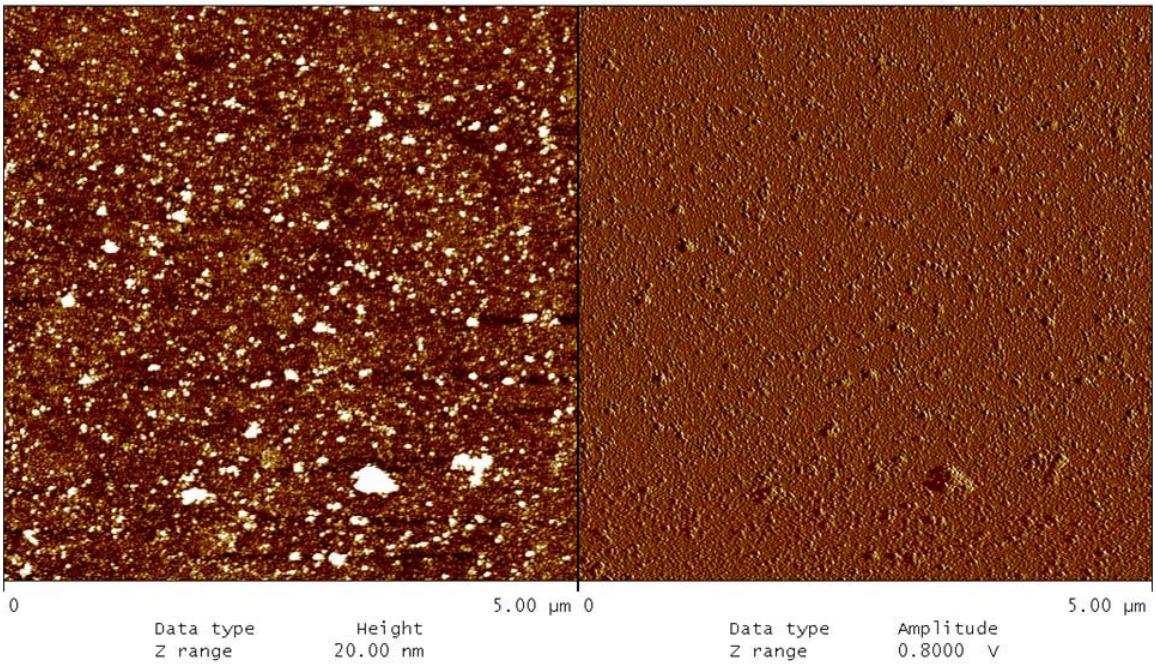

Figure 6.12 AFM (left) height and (right) phase images of the PS-PVP film prepared by Dr. Ho-Cheol Kim after quaternization and immersion in a citrate-capped Au NP solution.

6.4 Conclusions

PS-PVP block copolymer films were spin cast and annealed to generate a honeycomb pattern of PVP at the surface. Annealing in toluene relaxed the PS-PVP, and immersion in MeOH exposed the PVP spheres. Quaternizing with 1,4-dibromobutane cross-linked the PVP regions and gave them a positive charge. The quaternization caused the PVP regions to become swelled, probably due to the extra volume of the alkane chain.

After immersion into a citrate-capped Au NP solution, there were more raised areas on the PS-PVP film. The AFM phase image showed increased hardness of these raised areas, which may be from the deposited Au NPs. However, due to the small size of the Au NPs, it was impossible to resolve them with AFM or SEM.

Further study is needed to investigate the feasibility of using PS-PVP as chemical templates for the self-assembly of Au NPs. Improved AFM images would be needed to properly assess if Au NPs self-assemble on top of the quaternized PVP domains. It may also be possible to use a carbon nanotube coated AFM tip or STEM to investigate the self-assembly of the Au NPs.

6.5 References

1. BATES, F. S., Polymer-Polymer Phase Behavior. *Science* **1991,** *251* (4996), 898-905.
2. Zhao, J.; Jiang, S.; Ji, X.; An, L.; Jiang, B., Control of self-organized low-dimensional morphology in poly(styrene-b-4vinylpyridine)/polystyrene blend thin films. *Journal of Polymer Science Part B: Polymer Physics* **2004,** *42* (18), 3496-3504.
3. Zhao, J.; Jiang, S.; Ji, X.; An, L.; Jiang, B., Study of the time evolution of the surface morphology of thin asymmetric diblock copolymer films under solvent vapor. *Polymer* **2005,** *46* (17), 6513-6521.
4. Zhao, J.; Tian, S.; Wang, Q.; Liu, X.; Jiang, S.; Ji, X.; An, L.; Jiang, B., Nanoscopic surface patterns of diblock copolymer thin films. *The European Physical Journal E: Soft Matter and Biological Physics* **2005,** *16* (1), 49-56.
5. Meiners, J. C.; Ritzi, A.; Rafailovich, M. H.; Sokolov, J.; Mlynek, J.; Krausch, G., Two-dimensional micelle formation of polystyrene-poly(vinylpyridine) diblock copolymers on mice surfaces. *Applied Physics A: Materials Science & Processing* **1995,** *61* (5), 519-524.
6. Park, S.; Wang, J.-Y.; Kim, B.; Chen, W.; Russell, T. P., Solvent-Induced Transition from Micelles in Solution to Cylindrical Microdomains in Diblock Copolymer Thin Films. *Macromolecules* **2007,** *40* (25), 9059-9063.
7. Ishizu, K., Morphology of Core-Shell Type Polymer Microspheres on Carbon Substrates. *J. Colloid Interface Sci.* **1993,** *156* (2), 299-304.
8. Ishizu, K., Surface changes on block copolymers by crosslinking of spherical microdomains. *Polymer* **1989,** *30* (5), 793-798.
9. Ishizu, K.; Ikemoto, T.; Ichimura, A., Cross-linking reaction of poly(4-vinylpyridine) cylindrical microdomains of poly([alpha]-methylstyrene)-block-poly(4-vinylpyridine) films and characterization of soluble ribbon-like nanopolymers. *Polymer* **1999,** *40* (11), 3147-3151.
10. Lam, Y. M.; Song, L.; Moy, Y. C.; Xi, L.; Boothroyd, C., Controlled chemical stabilization of self-assembled PS-P4VP nanostructures. *J. Colloid Interface Sci.* **2008,** *317* (1), 255-263.
11. Kang, Y.; Walish, J. J.; Gorishnyy, T.; Thomas, E. L., Broad-wavelength-range chemically tunable block-copolymer photonic gels. *Nat Mater* **2007,** *6* (12), 957-960.
12. Tiller, J. C.; Liao, C.-J.; Lewis, K.; Klibanov, A. M., Designing surfaces that kill bacteria on contact. *Proceedings of the National Academy of Sciences* **2001,** *98* (11), 5981-5985.
13. Jana, N. R.; Gearheart, L.; Murphy, C. J., Seeding Growth for Size Control of 5−40 nm Diameter Gold Nanoparticles. *Langmuir* **2001,** *17* (22), 6782-6786.

Chapter 7

Janus Gold Nanorods

7.1 Introduction

While there was great effort to assemble Au NPs using chemical templates and in solution, Au NRs were only assembled using chemical templates. As with the Au NPs, the major drawback of using chemical templates is that the chemical templates do not self-assemble very many Au NRs at a time.

Previous work on assembling Au NRs on large scales in solution have used biological ligands to self-assemble Au NRs in both an end-to-end manner[1] and a side-by-side manner[2]. Solvent selectivity was also used to assemble Au NRs into various structures[3-5], as seen in Figure 1.6. Adipic acid was also used to assemble bundles of Au NRs in solution.[6] Yet, despite these efforts, there still has not been any successful technique to produce pairs of Au NRs in solution.

The idea here was to create Janus Au NRs, or Au NRs that were coated with inert ligands on all sides except one, which had a functional ligand. The functional ligand would be used to direct the self-assembly of the Au NRs by using either electrostatics or solvent selectivity.

Two separate efforts were conceived to produce Janus Au NRs. The first effort used EBL defined Au NRs which would be coated with a ligand, lifted off from the substrate, and then the newly exposed side would be coated with a second, functional

ligand. (Figure 7.1) The second effort worked in a similar vein, except CTAB coated Au NRs would be deposited on a substrate and the exposed surfaces would incur a ligand exchange. After lifting off the Au NR, the remaining surface that had been in contact with the substrate would undergo a ligand exchange for a functional ligand.

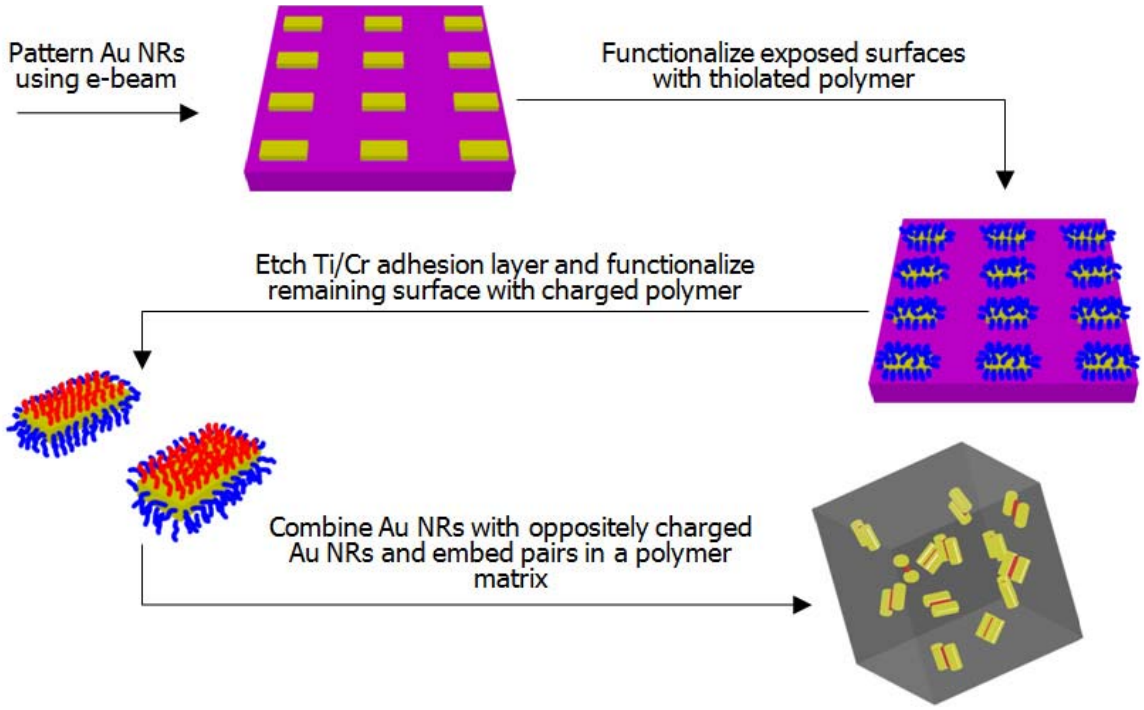

Figure 7.1 Illustrated protocol for generating Janus Au NRs with EBL and their electrostatic assembly.

7.2 Experimental

Thiol-functionalized poly(ethylene glycol) (HS-PEG, M_n = 2,000 g/mol) was purchased from Polymer Source. All other chemicals were purchased from Sigma Aldrich and used as received.

7.2.1 EBL Patterning of Au NRs

A 45 nm layer of thermal oxide was grown on the Si wafers. After a dehydration bake at 150°C for 5 min. on a hot plate, PMMA resist (PMMA 950k A2, MicroChem) was spin-coat onto the wafer at 4000 rpm for 60 sec. to obtain a resist thickness of ~ 65 nm. A pre-bake was then performed by heating the wafer at 170°C in an oven for 30 min.

Electron-beam lithography (EBL) was performed at 20 keV with at 30 um aperture using a Raith 150 (Raith) to write an array of 50,564 100 by 20 nm lines. After exposure, samples were developed by immersing samples in a 1:3 (v/v) mixture of MIBK and IPA for 20 sec., immersing samples in IPA for 30 sec., and drying the samples under a stream of N_2. O_2 plasma reactive ion etching (250 mT, 17% O2, 80 W, 15 s) was used to remove any trace organics from the wafer surface after development.

10 Å of Ti and 200 Å of Au were sequentially deposited using an SJ-20 electron-beam evaporator to form the Au NRs. Lift-off was done by immersing the sample in chloroform in a vial overnight and shaking the vial to remove the PMMA.

The sample was then immersed into an aqueous 1 mM HS-PEG solution overnight. Au NRs were liberated from the surface either by sonicating in MeOH for 2.5 hrs. or by immersion in HF.

7.2.2 Effects of Acids and Bases on the Gold-Thiol Bond

SPR-220 photoresist was spin-cast on a Si wafer using an ACS 200 cluster tool (Karl Suss) to generate a 3 μm thick film. The wafer was exposed using a custom made mask to generate 1 sq. in. features with an MA-6 mask aligner. Post-bake and development was performed using the ACS 200.

The patterned wafers were then treated with oxygen plasma and 100 Å of Ti and 2000 Å of Au were sequentially deposited using an SJ-20 electron-beam evaporator to form the Au squares. Lift-off was performed by sonicating the wafer in a large beaker of acetone. The wafer was scribed using a RA 120M Automatic Scriber (Karl Suss) to cleave the wafer into individual Au squares.

Oxygen and hydrogen plasma were sequentially used to clean the Au surface using a Plasmatherm 790. The Au coated Si wafers were then immersed into a 1 mM ethanolic dodecanethiol solution overnight to enable monolayer formation. The Au coated wafers were then washed with D.I. H_2O. The contact angle of a water droplet on the Au surface was measured in three locations.

Au coated Si wafers were then soaked in either acetic acid, hydrochloric acid, sulfuric acid, nitric acid, hydrofluoric acid, trifluoroacetic acid, hydrogen peroxide, or ammonium hydroxide for 5 min. The wafers were then transferred to 300 mL of D.I. H_2O for 10 min. and dried with Ar gas. The contact angle of a water droplet on the Au surface was measured in three locations again and XPS was used to examine the surface chemistry of the Au coated Si wafer.

7.2.3 Lifting-off Au NRs Deposited on a Surface

Au NRs were synthesized as reported elsewhere.[7] A CTAB-capped Au NP seed solution was prepared by adding 0.3 mL of an ice-cold 10 mM $NaBH_4$ aqueous solution to an aqueous solution containing 4.7 mL of 0.1 M CTAB and 25 μL of 50 mM $HAuCl_4$. A growth solution was prepared by first adding 30 mL of 0.1 M CTAB, followed by additions of 0.3 mL of 50 mM $HAuCl_4$, 0.57 mL of 1.0 M HCl, 360 μL of 10 mM

$AgNO_3$, and 240 μL of 0.1 M L-ascorbic acid. The addition of ascorbic acid turns the solution colorless. 72 μL of the 5 min. old CTAB-capped Au NP seed solution was added to the growth solution to initiate Au NR growth. The growth solution was kept at 30°C overnight for Au NR growth. Centrifugation at 10,000 *g* for 30 min. was performed twice to separate the Au NRs from excess CTAB and left-over starting materials. The supernatant was discarded each time and the Au NRs were redispersed in D.I. H_2O each time.

Pieces of Si wafers were coated with C12TMS via gas-phase silanization. The cleaned Si wafer was placed in a desiccator with 100 μL of silane overnight under vacuum. The wafer was then rinsed with MeOH and D.I. H_2O, and then placed on a hotplate at 140°C for 30 min.

A 10 μL droplet of the Au NR solution was placed on pieces of C12TMS coated wafers and allowed to dry in air. The wafers were then sonicated in D.I. H_2O for 30, 60, 120, or 180 min. to lift-off the Au NRs from the substrate. The lift-off solutions were analyzed with UV-Vis.

7.2.4 Characterization

Contact angle measurements were performed using a stereoscopic microscope and in-house software. UV-Vis absorption spectra were collected using a Cary UV-Vis Bio 50 (Varian) and scanning from 200 to 1000 nm. TEM and energy-dispersive X-ray spectroscopy (EDS) were performed using a Jeol 3011 HRTEM equipped with an EDS detector (EDAX) operating at 300 keV. SEM was performed using either an XL30 FEG

SEM (Phillips) operating at 10 keV or a Nova Nanolab FIB/SEM operating at 10 keV. XPS was performed using a Kratos Axis Ultra XPS.

7.3 Results and Discussion

7.3.1 EBL Patterning of Au NRs for Janus Au NRs

Au NRs were generated by EBL and the evaporation of Ti and Au. Figure 7.2 shows SEM images of typical Au NRs generated via this process with a 30 μm and a 10 μm aperture. The Au NRs produced with the 30 μm aperture were thicker than both those produced with the 10 μm aperture and what was programmed into the EBL pattern. The reason the Au NRs are thicker is because the beam is thicker for the 30 μm aperture than for the 10 μm aperture. Thus, the beam is unable to generate features as fine as 20 nm. However, the beam current is ~10× larger when using a 30 μm aperture, so more Au NRs may be produced in a shorter amount of time.

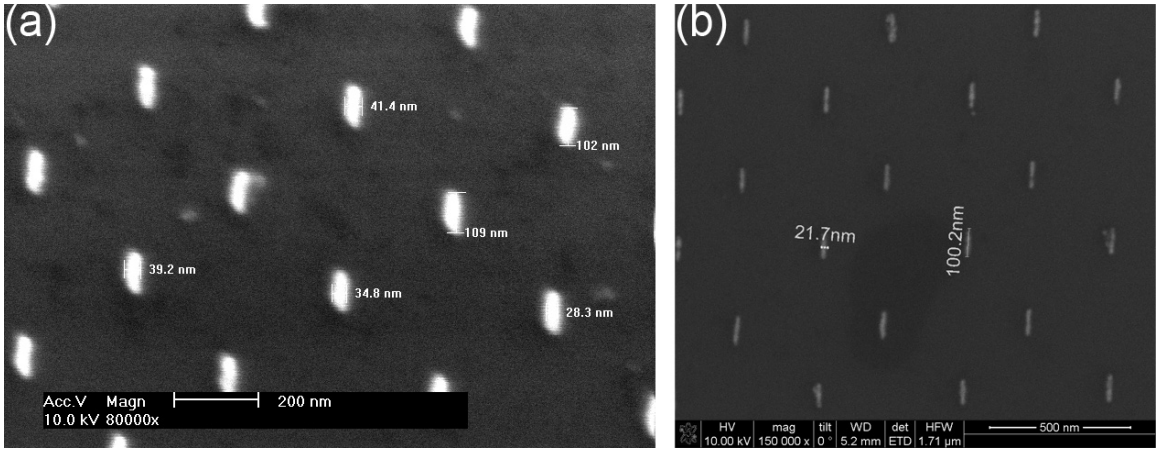

Figure 7.2 SEM image of Au NRs generated by EBL at 20 keV with a (a) 30 μm and (b) 10 μm aperture.

Au NRs were immersed in a HS-PEG solution to coat the exposed Au surfaces with HS-PEG. The HS-PEG is water soluble, so the Au NRs should be able to be suspended in solution after they are lifted off. Sonication in MeOH for 2.5 hrs. liberated the Au NRs from the Si surface. The MeOH lift-off solution was concentrated with centrifugation and UV-Vis was used to observe if any Au NRs were in the solution. Figure 7.3a is of the UV-Vis spectra of the concentrated lift-off solution. While there is no peak around 520 nm, only 50,564 Au NRs are patterned on the surface. As previously discussed in Chapter 3, this number of Au NRs is incredibly too small to be detected by the UV-Vis.

TEM was used to visualize the contents of the lift-off solution, as seen in Figure 7.3b. Clearly, metallic nanoparticles are present in the lift-off solution. However, the majority of these particles are smaller than 20 nm, which means that the Au NRs are destroyed during the sonication for lift-off. EDS was used on the TEM sample to determine the nature of the metallic nanoparticles. The EDS spectrum is seen in Figure 7.3c. The peaks for Cu, Co, and Fe are from the TEM column and the TEM grid. A peak for Ti is present at ~4.25 keV, but there are no peaks for Au. Thus, it appears that the metallic nanoparticles are actually Ti nanoparticles. The Ti nanoparticles most likely formed during the sonication for lift-off, since Ti was used as an adhesion layer between the Au NR and the Si substrate. Oddly enough, there is no Au present anywhere. The most likely explanation is that that the Au NRs are destroyed during the lift-off process and the absorption peaks in Figure 7.3a below 300 nm are from the HS-PEG. Still, the fate of the Au NRs is unknown.

HF was also used to lift-off the Au NRs, since wet etching would not damage the Au NRs like the sonication. Despite the selectively etching both the SiO_2 and the Ti adhesion layer, no Au NRs could be observed after lift-off with HF. This is most likely due to the small number of Au NRs that are generated with this technique.

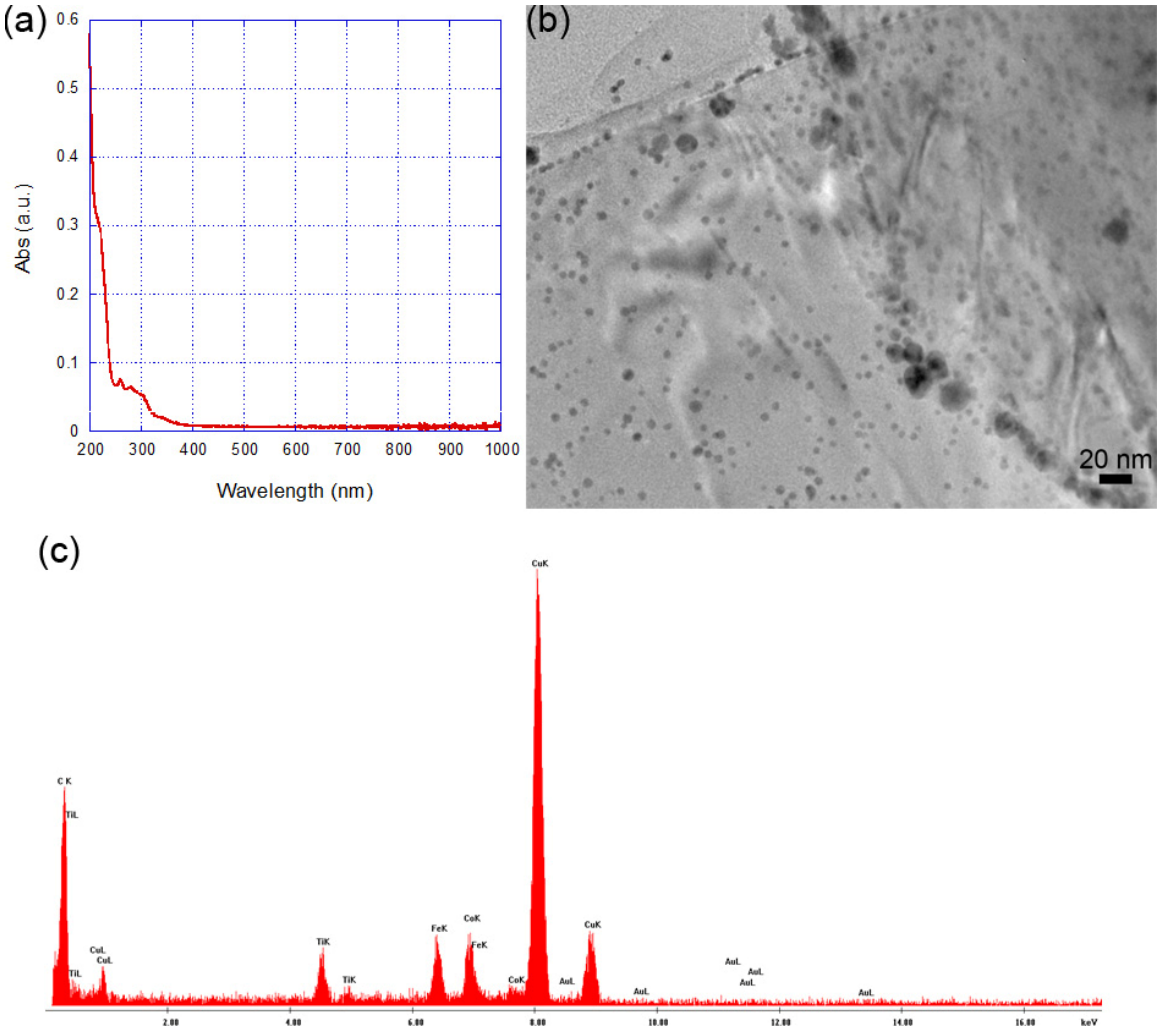

Figure 7.3 The (a) UV-Vis spectrum, (b) TEM image, and (c) EDS spectrum of the MeOH lift-off solution after lifting-off the Au NRs.

7.3.2 The Effects of Acids and Bases on Dodecanethiol Coated Au Films

Since HF was to be used to etch the Ti and SiO_2 that anchored the EBL defined Au NRs to the substrate, it was necessary to see how HF would affect a thiol-functional

ligand. Dodecanethiol was chosen because of its ability to form a hydrophobic, self-assembled monolayer on Au films and its simple chemistry.[8]

The acids and bases that were selected for this study were chosen because they are commonly used to wet etch metals and other materials. TFA was chosen because it is both an acid and it is an organic solvent. Thus, the TFA should wet the dodecanethiol surface.

Figure 7.4 graphically displays the contact angles of a dodecanethiol coated Au film before and after being exposed to an acid or a base. The average contact angle for all of the samples as prepared is ~102°, which indicates a hydrophobic surface. The only sample which showed an average contact angle below 100° was the HCl sample. But, the large standard deviation indicates that one data point skewed the average lower than it should have been. This must be the case, because the contact angle is larger after the acid exposure and the standard deviation is smaller.

Both the nitric acid and hydrogen peroxide samples showed decreased contact angles after exposure to the acid and base, respectively. Both nitric acid and ammonium hydroxide are known to be capable of oxidizing organics. Thus, the decreased contact angles may be due to oxidation of the dodecanethiol.

XPS was used to determine if the acids or bases disrupted the chemistry of the dodecanethiol ligand bound to the Au surface. The XPS data for the dodecanethiol coated Au films is summarized in Table 7.1. The plain sample is a dodecanethiol coated Au film that was used as prepared. Comparing the atomic percentages for the S 2p content, it would appear that only the nitric acid treated sample shows a large decrease in S 2p. Both the nitric acid and the hydrogen peroxide samples show substantial increases in the O 1s

content, which supports the theory that these chemicals oxidize the dodecanethiol. Also, the nitric acid shows a decrease in C 1s content, which indicates that the nitric acid may have etched the dodecanethiol.

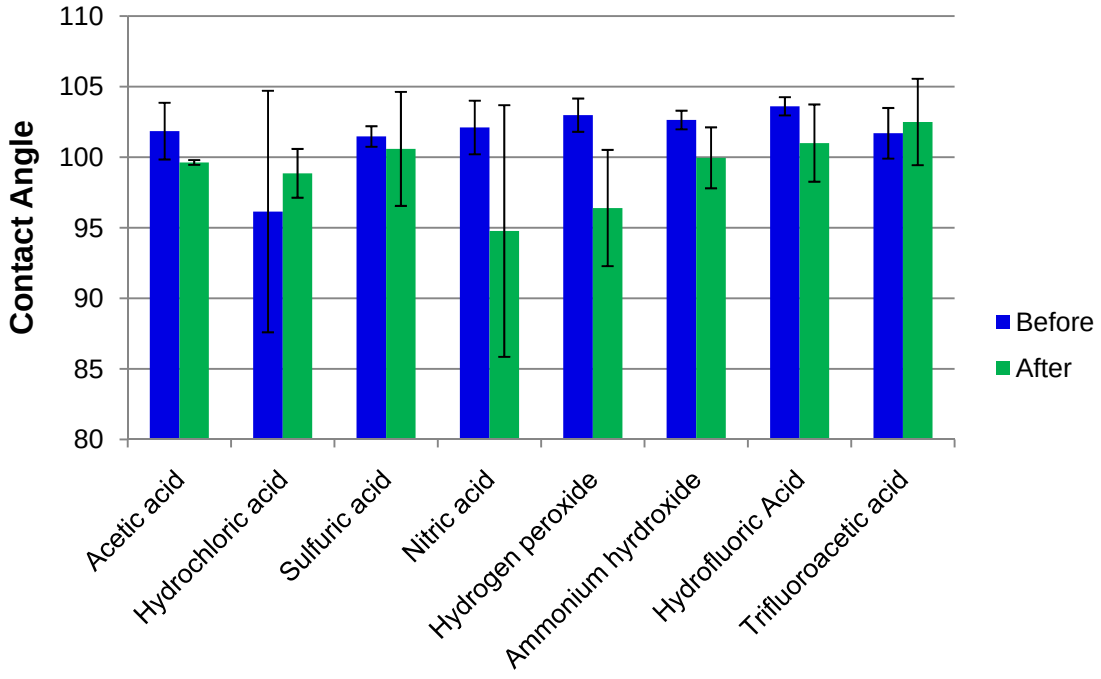

Figure 7.4 Contact angles of water on the dodecanethiol-coated Au surface before and after soaking in an acid or a base.

Table 7.1 XPS data for the relative atomic percentages of the surfaces of dodecanethiol coated Au films on Si wafers before and after being soaked in an acid or a base

	Plain	**Acetic acid**	**HCl**	**H_2SO_4**	**HNO_3**	**H_2O_2**	**NH_4OH**	**HF**	**TFA**
Au 4f	58.20	57.95	56.88	56.48	62.78	56.78	54.85	55.31	51.77
S 2p	2.10	2.24	2.28	3.24	1.37	2.00	1.86	3.08	2.74
C 1s	38.35	38.34	40.24	39.38	33.29	38.10	42.23	40.58	44.01
O 1s	1.36	1.48	0.60	0.89	2.56	3.12	1.07	1.03	1.48

Thus, it appears that the nitric acid is most capable of damaging the dodecanethiol, including cleaving the Au-S bond. The hydrogen peroxide may only oxidize the dodecanethiol, but does not appear to damage the Au-S bond. Based on the

contact angle measurements and the XPS data, the rest of the acids and bases appear to have little to no effect on the dodecanethiol. However, longer exposure times may reveal more adverse effects.

7.3.3 Lifting-off Au NRs Deposited on a Surface

Au NRs were drop cast on a C12TMS coated substrate. It took ~2 hrs. for the 10 μL droplet to evaporate. Samples were placed in a 20 mL vial with D.I. H_2O so that the sample was floating on the D.I. H_2O surface, with the C12TMS side in the D.I. H_2O. Attempts to sonicate with the Si wafer submerged in the D.I. H_2O resulted in the Si wafer floating to the top of the D.I. H_2O due to the hydrophobicity of the C12TMS monolayer and the general buoyancy of the Si wafer piece.

The CTAB-capped Au NRs are hydrophilic and are only confined to the C12TMS surface because the D.I. H_2O evaporated. Thus, by sonicating the sample in D.I. H_2O, it is expected that CTAB-capped Au NRs will come off of the Si wafer into solution. The UV-Vis spectra for the lift-off solutions are seen in Figure 7.5. The UV-Vis spectra for the Au NRs, CTAB, and D.I. H_2O are also included for reference.

All of the UV-Vis spectra for the lift-off solutions show absorption peaks around 250 nm, which is most likely due to CTAB. None of the lift-off solutions show an absorption peak around 525 nm except for the 30 min. solution. This solution also shows absorption around 850 nm. Both of these absorption peaks match up well with those of the Au NRs' transverse and longitudinal plasmon absorptions. All of the lift-off solutions show some absorption around 950 nm. This could correspond to aggregates of Au NRs that lift-off into the D.I. H_2O. The Au NRs may have formed these aggregates as the D.I.

H_2O evaporated in order to minimize their free energy in the presence of the hydrophobic C12TMS coated surface. However, since the lift-off solutions did not display absorption peaks similar to those of the Au NRs, it appears that this technique is not successful for confining and lifting-off Au NRs. Etching the SiO_2 substrate with HF could enable the Au NRs to lift-off successfully.

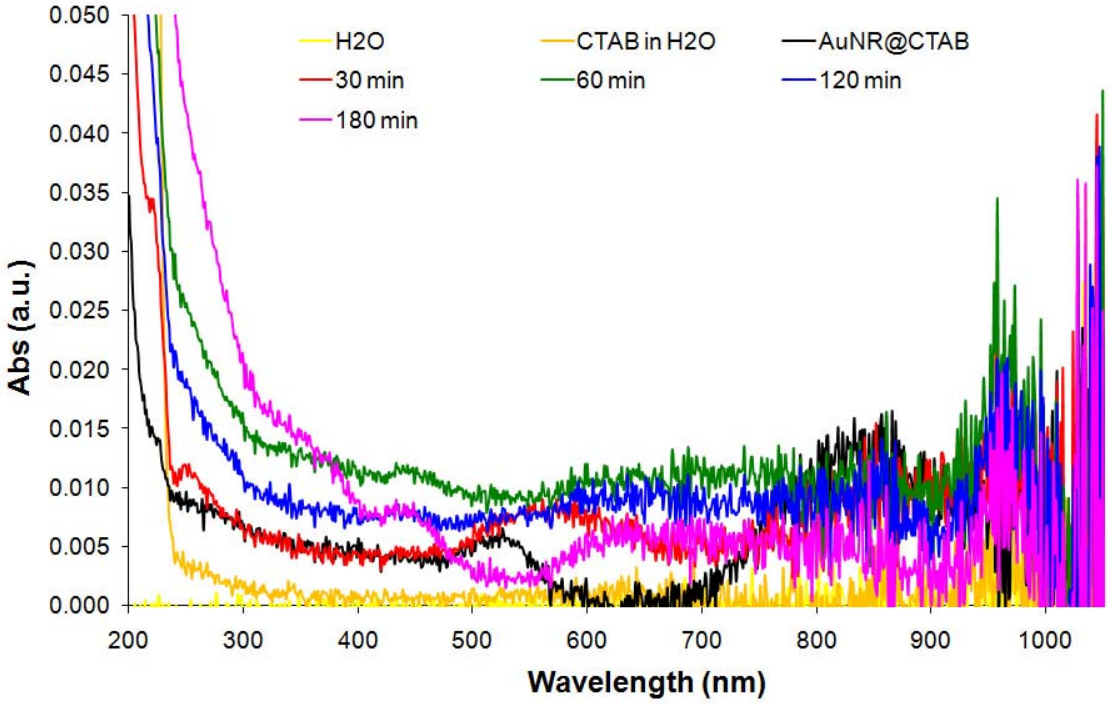

Figure 7.5 UV-Vis spectra of the D.I. H_2O lift-off solutions for CTAB-capped Au NRs sequestered on a C12TMS coated Si wafer. Spectra for CTAB and CTAB-capped Au NRs are included as references.

7.4 Conclusions

Two separate techniques were presented for preparing Janus Au NRs. The first technique used EBL to generate Au NRs. However, this technique suffers from poor throughput, as it takes ~15 min. to generate 50,596 Au NRs. In order to produce 10^8 Au NRs, at least eight hours of EBL would be necessary.

Also, using sonication to lift-off the Au NRs appears to destroy the Au NRs. Since there were so few Au NRs available, they were impossible to detect via UV-Vis even when HF was used for the lift-off.

The effects of common acids and bases on the Au-S bond was also investigated. It appears that dodecanethiol-coated Au films are not affected by exposure to acids or bases except for powerful oxidizers like nitric acid and hydrogen peroxide. Still, if the dodecanethiol-coated Au films were immersed in the acids and bases for longer times, adverse effects may be observed.

CTAB-capped Au NRs that were deposited on a C12TMS coated Si substrate attempted to be lifted-off by sonicating the Si substrate in D.I. H_2O. UV-Vis was used to characterize the lift-off solutions and revealed that the individual Au NRs did not lift-off of the substrate, but aggregates of Au NRs may have lifted-off in solution. Thus, this technique was inadequate for Janus Au NR production. Etching the SiO_2 substrate with HF, however, may enable lift-off.

7.5 References

1. Caswell, K. K.; Wilson, J. N.; Bunz, U. H. F.; Murphy, C. J., Preferential End-to-End Assembly of Gold Nanorods by Biotin−Streptavidin Connectors. *J. Am. Chem. Soc.* **2003,** *125* (46), 13914-13915.
2. Gole, A.; Murphy, C. J., Biotin−Streptavidin-Induced Aggregation of Gold Nanorods: Tuning Rod−Rod Orientation. *Langmuir* **2005,** *21* (23), 10756-10762.
3. Fava, D.; Nie, Z.; Winnik, M. A.; Kumacheva, E., Evolution of Self-Assembled Structures of Polymer-Terminated Gold Nanorods in Selective Solvents. *Adv. Mater.* **2008,** *20* (22), 4318-4322.
4. Nie, Z. H.; Fava, D.; Kumacheva, E.; Zou, S.; Walker, G. C.; Rubinstein, M., Self-assembly of metal-polymer analogues of amphiphilic triblock copolymers. *Nat. Mater.* **2007,** *6* (8), 609-614.
5. Nie, Z. H.; Fava, D.; Rubinstein, M.; Kumacheva, E., "Supramolecular" assembly of gold nanorods end-terminated with polymer "Pom-Poms": Effect of pom-pom structure on the association modes. *J. Am. Chem. Soc.* **2008,** *130* (11), 3683-3689.
6. Orendorff, C. J.; Hankins, P. L.; Murphy, C. J., pH-Triggered Assembly of Gold Nanorods. *Langmuir* **2005,** *21* (5), 2022-2026.
7. Carbó-Argibay, E.; Rodríguez-González, B.; Pacifico, J.; Pastoriza-Santos, I.; Pérez-Juste, J.; Liz-Marzán, L. M., Chemical Sharpening of Gold Nanorods: The Rod-to-Octahedron Transition. *Angewandte Chemie International Edition* **2007,** *46* (47), 8983-8987.
8. Bain, C. D.; Troughton, E. B.; Tao, Y. T.; Evall, J.; Whitesides, G. M.; Nuzzo, R. G., Formation of monolayer films by the spontaneous assembly of organic thiols from solution onto gold. *J. Am. Chem. Soc.* **1989,** *111* (1), 321-335.

Chapter 8

Conclusions and Remarks

8.1 Conclusions

The purpose of this thesis is to explore novel techniques for self-assembling nanogold to be used as building blocks for optical metamaterials. In the following sections, the conclusions of the electrostatic self-assembly using chemical templates, cross-linking Au NPs, the self-assembly of Au NPs using good-solvent evaporation, and Janus Au NRs are summarized.

8.1.1 Electrostatic Self-Assembly of Nanogold Using Chemical Templates

The initial plan was to use a chemical template as a factory for self-assembling nanogold. By controlling the size of the chemical template, different numbers of nanogold elements would self-assemble on the chemical template. Electrostatics were used to direct the self-assembly because they are long-range forces and it is easy to tailor the surface charge of both nanogold and substrates.

A chemical template was generated using EBL and an aminosilane. The feature sizes of the chemical templates were limited by the size of the electron beam used in the EBL. The aminosilane self-assembled on exposed SiO_2 to give the patterned area a positive charge. The choice of aminosilane proved to be critical. APDMES was chosen

because APTMS and other aminosilanes with multiple ethoxy or methoxy groups can form gels, which resulted in "halos" of aminosilane on the wafer surface.[1]

Various sizes of dots were used in the chemical templates, which enabled different numbers of Au NPs to self-assemble on the dots. The ratio between the diameter of the aminosilane dot and the diameter of the Au NP determined how many Au NPs would self-assemble on the dot. It was found that the electrostatic self-assembly of the Au NPs was very fast, reaching an equilibrium after ~10 minutes.

By adding NaCl to the Au NP solution, it was possible to increase the number of Au NPs that self-assemble on the same size aminosilane dot. This was due to the charge screening of the NaCl. However, care should be taken as to when the NaCl is added to the Au NP solution. If the NaCl concentration of the Au NP solution becomes too large, the Au NPs will irreversibly aggregate and there will be non-specific deposition on the chemical pattern substrate.

The electrostatic self-assembly of Au NRs was more challenging, most likely due to the fact that the Au NRs are anisotropic and are synthesized with CTAB, a positively charged, cationic surfactant. Thus, either the surface charge of the Au NRs must be altered to be compatible with the aminosilane chemical template or a negatively charged chemical template must be used.

PSS was used to coat the CTAB-capped Au NRs in order to give the Au NRs a negative surface charge, but this did not work very well for the self-assembly of the Au NRs. It is believed that there was a mismatch between the size of the Au NRs and the molecular weight of the PSS that prevented this method from being successful.[2, 3]

A negatively charged chemical template was created by using EBL to cross-link PSS. This way, the CTAB-coated Au NRs could self-assemble on the negatively charged PSS pattern. However, the Au NRs appeared to prefer to self-assemble on the edges of the PSS pattern, not on top of the PSS pattern. This may have been caused by surface roughness on the PSS surface or the edges of the PSS were the most energetically preferred configuration for the Au NRs.

The CTAB capping agent was replaced with MUA via a ligand exchange reaction on the Au NRs.[4] The MUA enabled the Au NRs to be used with the aminosilane chemical template due to the negatively charged carboxylic acid. Care should be taken when returning the Au NRs to a neutral pH from the basic conditions necessary for the ligand exchange. If the Au NRs are centrifuged in a pH neutral solution, irreversible aggregation of the Au NRs occurred. This may be due to poor repulsion between Au NRs at neutral pHs and the centrifuging forcing the Au NRs to aggregate. The MUA-capped Au NRs were successful in self-assembling on the APDMES chemical template, but the kinetics were slower than for the Au NPs. The slower kinetics are most likely due to the anisotropy of the Au NRs.

8.1.2 Cross-Linking Au NPs Using PDDA

Since the chemical templates were to serve as factories for creating assemblies of nanogold, the assembled nanogold must be cross-linked and lifted-off from the chemical templates. PDDA was used to cross-link self-assembled Au NPs. The PDDA has a permanent charge, so the electrostatic attraction to the Au NPs is pH independent.

Additional Au NPs were shown to self-assemble on top of the PDDA cross-linked Au NPs, indicating that the PDDA is successful at binding to the Au NPs.

NaOH solutions were used to lift-off the cross-linked Au NPs by immersing the chemical templates holding the self-assembled Au NPs into NaOH solutions. While the basic conditions should release the Au NPs from the APDMES substrate due to the deprotonation of the APDMES amine in basic solutions, no lift-off was observed without sonicating the lift-off solution. Since the self-assembly of the Au NPs was found to be unsuccessful at a pH = 11 due to the deprotonated aminosilane, it appears that the Au NPs are not simply electrostatically bound to the chemical template. It is possible that the aminosilane ionically binds to the Au NP, which leads to a more stable bond than the electrostatic attraction between the Au NP and the aminosilane. This ionic bond and van der Waals forces between the Au NP and the substrate may be why sonication is required to lift-off the Au NPs.

8.1.3 Self-Assembly of Au NPs Via Good-Solvent Evaporation

The spherical self-assembly of large quantities of Au NPs was successfully prepared by using the good-solvent evaporation process with HS-PS coated Au NPs. It was found that the microbead assemblies of Au NPs were generally smaller for larger molecular weight HS-PS. Also, larger Au NPs generally yielded larger microbead assemblies. Although it was thought that stirring would result in more uniform microbead assembly sizes, stirring actually resulted in less uniform sizes. This was most likely due to the shear effects of the stirring that could break apart assemblies of Au NPs. Also, rapid stirring accelerated the evaporation of the solution, which led to larger microbead

sizes and greater size variations. By allowing the evaporation to proceed without agitation, relatively uniform microbead assemblies were formed.

8.1.4 Janus Au NR Fabrication

The concept for Au NRs with two different ligands, or Janus Au NRs, would allow for self-assembly of the Au NRs based on solvent selectivity for one ligand, electrostatics between functional ligands, or biological interactions. Two methods for creating Janus Au NRs were conceived. The first method involved drop-casting wet chemistry synthesized Au NRs on a substrate, exchanging the ligands on the exposed surfaces, and lifting-off the Au NRs from the substrate. However, after drop-casting the Au NRs, it was not possible to liberate the individual Au NRs from the substrate despite unfavorable interactions between the Au NRs and the substrate.

EBL was also used to fabricate Au NRs. The exposed surfaces could be capped with a thiol-functional ligand and the final surface could be capped with a second thiol-functional ligand. However, attempts to lift-off the Au NRs were not successful. Using sonication appeared to destroy the Au NRs and lift-off with HF was inconclusive, since no Au NRs could be detected.

8.2 Future Considerations

The work presented here is not just a chronicle of success, but a chronicle of failure as well. Based on these failures, it is possible to direct which directions to pursue in the future.

In the case of the electrostatic self-assembly of nanogold using chemical templates, this process was fairly successful for Au NPs and somewhat successful for Au NRs. Assembling CTAB-capped Au NRs on PSS templates could be perfected by annealing the PSS film to reduce surface roughness and using oxygen plasma to thin the PSS in order to prevent the Au NRs from self-assembling on the sides of the PSS patterns.

Cross-linking and lifting-off the Au NPs showed limited success with PDDA. Since sonication was necessary to liberate the Au NPs from the surface, it would appear that more than electrostatics are keeping the Au NPs at the surface. If the attraction were purely electrostatic, then the Au NPs would move around if the substrate was reimmersed into D.I. H_2O and subsequent imaging of the same region would reveal a different configuration of Au NPs. A study into the nature of the bonding holding the Au NPs on the chemical template is necessary to choose a better cross-linking molecule and lift-off conditions. If the bonding is purely electrostatic, then a short, dithiol ligand could be used to cross-link the Au NPs since the Au NPs would "dance around" on the aminosilane dot while in water until the dithiol molecule binds the Au NPs together. Additional thiols could be used to cap the rest of the Au NP surface, which could disable the electrostatic interaction holding the Au NPs on the chemical template.

The PS-PVP thin films could also be used to direct the self-assembly of Au NPs that are too small (~5 nm) to be used to generate monomers, dimmers, and trimers of Au NPs with the relatively large patterns (~40 nm) generated via EBL. However, in aqueous solutions the PVP domains are prone to swelling, which could greatly affect the self-assembly of the Au NPs. The success of this method is very questionable. A better

technique for producing fine chemical templates for the self-assembly of Au NPs may be block copolymer nanolithography.[5-10] This would involve selectively etching the minority block of a block copolymer to pattern aminosilane on the exposed Si surface.

In order to get the Janus Au NRs to work, a proof of concept at the micron-scale may be used. This would use photolithography to produce the Au microrods, which would greatly improve the throughput of the process. Also, this would give insight into if the HF could be used to gently release the Au NRs without destroying them. The major challenge with the Janus Au NRs is throughput. It is very difficult to produce billions of Au NRs via lithography, although it is very easy via chemical synthesis. One way to improve the throughput would be to use nanoimprint lithography. However, the main bottleneck would be fabricating the imprint mask.

Another approach to forming elements for optical metamaterials would be the self-assembly of metamaterial unit cells. Previously, micron-sized, hexagonal discs were self-assembled into large, highly ordered, three-dimensional arrays.[11] Based on the hydrophobicity and hydrophilicity of the surfaces of these discs, which were generated using self-assembled monolayers, the discs self-assembled. If such discs were patterned with SRRs, it could be possible to self-assemble three-dimensional NIMs from these discs. The investigation into the stability of the Au-S bond was done partially to assess if the ligand could withstand the exposure to common acids and bases used to etch materials that may be used in the fabrication of these discs.

Lastly, the most important future work that should be embarked is the optical characterization of the self-assembled nanogold. While the idea was to create elements for optical metamaterials, no optical measurements were performed to determine the

permeability or permittivity of the self-assembled nanogold. Once the optical properties of the self-assembled nanogold structures are assessed, it would be possible to go back and refine the self-assembly to produce structures with more meaningful properties, if necessary. The microbead assemblies of Au NPs should be the first things to characterize, since they are available in large quantities.

8.3 References

1. Pallandre, A.; Glinel, K.; Jonas, A. M.; Nysten, B., Binary nanopatterned surfaces prepared from silane monolayers. *Nano Letters* **2004,** *4* (2), 365-371.
2. Gole, A.; Murphy, C. J., Polyelectrolyte-Coated Gold Nanorods: Synthesis, Characterization and Immobilization. *Chem. Mat.* **2005,** *17* (6), 1325-1330.
3. Gittins, D. I.; Caruso, F., Tailoring the Polyelectrolyte Coating of Metal Nanoparticles. *The Journal of Physical Chemistry B* **2001,** *105* (29), 6846-6852.
4. Walker, D. A.; Wilmer, C. E.; Kowalczyk, B.; Bishop, K. J. M.; Grzybowski, B. A., Precision Assembly of Oppositely and Like-Charged Nanoobjects Mediated by Charge-Induced Dipole Interactions. *Nano Letters* **2010,** *10* (6), 2275-2280.
5. Jung, Y. S.; Lee, J. H.; Lee, J. Y.; Ross, C. A., Fabrication of Diverse Metallic Nanowire Arrays Based on Block Copolymer Self-Assembly. *Nano Letters* **2010,** *10* (9), 3722-3726.
6. Cheng, J. Y.; Ross, C. A.; Chan, V. Z. H.; Thomas, E. L.; Lammertink, R. G. H.; Vancso, G. J., Formation of a Cobalt Magnetic Dot Array via Block Copolymer Lithography. *Adv. Mater.* **2001,** *13* (15), 1174-1178.
7. Jung, Y. S.; Chang, J. B.; Verploegen, E.; Berggren, K. K.; Ross, C. A., A Path to Ultranarrow Patterns Using Self-Assembled Lithography. *Nano Letters* **2010,** *10* (3), 1000-1005.
8. Jung, Y. S.; Jung, W.; Ross, C. A., Nanofabricated Concentric Ring Structures by Templated Self-Assembly of a Diblock Copolymer. *Nano Letters* **2008,** *8* (9), 2975-2981.
9. Jung, Y. S.; Jung, W.; Tuller, H. L.; Ross, C. A., Nanowire Conductive Polymer Gas Sensor Patterned Using Self-Assembled Block Copolymer Lithography. *Nano Letters* **2008,** *8* (11), 3776-3780.
10. Jung, Y. S.; Ross, C. A., Solvent-Vapor-Induced Tunability of Self-Assembled Block Copolymer Patterns. *Adv. Mater.* **2009,** *21* (24), 2540-2545.
11. Clark, T. D.; Tien, J.; Duffy, D. C.; Paul, K. E.; Whitesides, G. M., Self-Assembly of 10-μm-Sized Objects into Ordered Three-Dimensional Arrays. *J. Am. Chem. Soc.* **2001,** *123* (31), 7677-7682.